ngVLA 6m Antenna Concept Design Document

Document Number ngVLA6-0000-002-CDD-002
Revision: ..... A
Author ..... G. Lacy
Date 2021-03-25
Status ..... Final
Classification ..... Unrestricted

Prepared By	Name	G. Lacy	Signature	Lacy, Gordon Digitally signed by Lacy, Gordon DN: cn=Lacy, Gordon, c=CA, o=GC, ou=NRC-CNRC, email=gordon.lacy@cnrc-nrc.gc.ca Date: 2021.09.23 11:57:12 -07'00'
	Organisation	NRC		
Reviewed By	Name	Gordon Lacy	Signature	Lacy, Gordon Digitally signed by Lacy, Gordon DN: cn=Lacy, Gordon, c=CA, o=GC, ou=NRC-CNRC, email=gordon.lacy@cnrc-nrc.gc.ca Date: 2021.09.23 11:57:03 -07'00'
	Organisation	NRC		
	Name	Nathan Loewen	Signature	2021-09-24
	Organisation	Sightline Engineering		
	Name	Gordon Lacy	Signature	Lacy, Gordon Digitally signed by Lacy, Gordon DN: cn=Lacy, Gordon, c=CA, o=GC, ou=NRC-CNRC, email=gordon.lacy@cnrc-nrc.gc.ca Date: 2021.09.23 11:56:23 -07'00'
	Organisation	NRC		
Approved By	Name	Scott Roberts	Signature	Roberts, Scott Roberts, Scott cn=Roberts, Scott, c=CA, o=GC, ou=NRC-CNRC, email=scott.roberts@cnrc-nrc.gc.ca 2021.09.23 19:08:40 -07'00'
	Organisation	NRC		
Issued By	Name	Gordon Lacy	Signature	Lacy, Gordon Digitally signed by Lacy, Gordon DN: cn=Lacy, Gordon, c=CA, o=GC, ou=NRC-CNRC, email=gordon.lacy@cnrc-nrc.gc.ca Date: 2021.09.23 11:55:48 -07'00'
	Organisation	NRC		

[This document describes concept design for the ngVLA 6m Antenna Design project.]

DOCUMENT HISTORY

Revision	Date	Change Request	Change Description
A	25Mar2021		Initial draft for comment – copied from P2 CDD
B	27Mar2021		Final version

DOCUMENT SOFTWARE

Application		Version	Filename
Wordprocessing	MSWord		ngVLA6-0000-001-CDD-002_CoDesignDoc_P3_A_2021-04-26.docx

ORGANISATION DETAILS

Designation	Name	Organisation
Primary Author and Responsible Organisation	G. Lacy	NRC
Contributors	G. Lacy	NRC
	M. Islam	NRC
	N. Loewen	Sightline Engineering
	E. van Vuuren	Sightline Engineering

TABLE OF CONTENT

LIST OF TABLES

LIST OF FIGURES

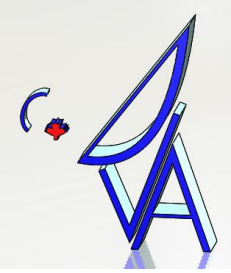

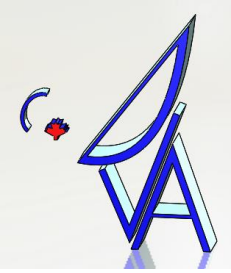

LIST OF ACRONYMS AND ABBREVIATIONS

BUS	BackUp Structure
CTE	Coefficient of Thermal Expansion
DVA	Dish Verification Antenna
ERA	Elevation Rotating Assembly
FE	Finite Element
FEA	Finite Element Analysis
BUS	Inner Backup Structure
ngVLA	next generation Very Large Array
NRAO	National Radio Astronomy Observatory (USA)
NRC	National Research Council (Canada)
OBUS	Outer Backup Structure
PE	Pointing Error
QISO	Quasi-Isotropic
RF	???
RMS	Root Mean Square
SPEM	Systematic Pointing Error correction Model
SBA	Short Baseline Array
SRC	Single-piece Rim-supported Composite
VLA	Very Large Array
XEL	Cross-elevation

1 INTRODUCTION

1.1 Purpose of Document

The purpose of this document is to describe the design concept of the National Research Council of Canada (NRC) Next Generation Very Large Array (ngVLA) 6m Antenna as called out in Statement of Work NRC ngVLA 6m Antenna Study, [AD02].

1.2 Scope of Document

This document describes the current status of the design concept for the 6m antenna. It is an interim report intended to show the design concept that will be taken forward to a Conceptual Design Review at a TBD date.

This document describes the operational context of the design and the operating conditions as defined in the ngVLA Short Baseline Array SBA Antenna: Preliminary Technical Specifications, [AD01] and ngVLA: System Environmental Specifications [AD04].

- The project assumptions and risks are presented with their status and mitigation plans.
- Methods of accounting for system budgets are described, error budgets and initial analysis results for key performance requirements are presented.
- Production logistics concepts are described for manufacturing and assembly.
- Finally a summary of the key future tasks is provided.

1.3 Intended Audience

This document is expected to be used by the NRC ngVLA Antenna Design Team, National Radio Astronomy Observatory (NRAO) ngVLA Antenna Integrated Product Team and the ngVLA System Engineering and Management Team.

1.4 Design Context

NRC has conducted three design studies for the ngVLA; an initial community study based on DVA1/2 15m optics, [RD02], in 2017 and then two conceptual designs in 2018; a 6m, [RD03] and an 18m, [RD04], in parallel. Due to the relative cost impacts for the project, 214 x 18m antenna could constitute ~50% of the overall project cost vs <5% for the 19x 6m antennas, a much greater emphasis was put on the 18m design. The 6m antenna design presented in [RD03] was based on the extensive 18m development and an existing mount designed for 10m satcom antennas. The ngVLA 6m and 18m antennas, essentially, must meet the same requirements (other than optical surface sizes); however, designing the 18m antenna to meet these requirements is much more difficult than the 6m. Given

limited resources the bulk of design and analysis effort had therefore been put into the 18m design with the understanding that there will very low risk in meeting the requirements with the 6m design by the application of the same design concepts. Therefore the design study contained a minimal amount of analysis of the performance of the 6m. Its ability to meet the requirements is inferred by analogy to the 18m design. The exception is the close packing requirement of 11m centre to centre for the 6m antenna. This unfortunately was overlooked in that design study and so the 6m design presented did not meet the requirement.

Post the PDR held in October 2018 NRAO requested NRC to progress the 6m design addressing the close packing issue. This document outlines the work performed thus far and presents the current state of the design.

2 APPLICABLE AND REFERENCE DOCUMENTS

2.1 Applicable Documents

The following documents at their indicated revision form part of this document to the extent specified herein.

Table 2-1 Applicable Documents

Ref No	Document/Drawing Number	Document Title	Revision
AD01	020.47.05.00.00-0001-SPE	ngVLA Short Baseline Array SBA Antenna: Preliminary Technical Specifications	2
AD02	020.25.00.00.00-0004-SOW	Statement of Work NRC ngVLA 18m Antenna Study - Phase 2	
AD03	101-0000-001-REG-001	ngVLA 6m Antenna Risk Register	A
AD04	020.10.15.10.00-0001-SPE	ngVLA: System Environmental Specifications	

2.2 Reference Documents

The following documents provide useful reference information associated with this document. These documents are to be used for information only. Changes to the date and/or revision number do not make this document out of date.

Table 2-2 Reference Documents

Ref No	Document/Drawing Number	Document Title	Revision
RD01	101-0000-004-PLN	ngVLA 18m Antenna Preliminary Production Plan	A
RD02		ngVLA Memo 26 15m Design Study	
RD03	101-0000-001-CDD	ngVLA 18m Antenna Concept Design Document	B
RD04	102-0000-001-CDD	ngVLA 6m Antenna Concept Design Document	A
RD05		20210611-NRC_DRAO_FE_Model_Report-01.pdf	

3 OPERATIONAL CONTEXT

The ngVLA array will consist of 214 x 18m antennas and 19 x 6m antennas. The 6m antennas will be deployed on the Plains of San Agustin in New Mexico at the core of the array with baselines from 11 to 60m, [AD01]. All antennas will be fixed position, the array will not be reconfigurable.

The project has defined four functional regimes;

1. Precision Operating: low wind speed, at night, low temperature rate of change and no precipitation.
2. Normal Operating: moderate wind speed, day/night, moderate temperature rate of change and no precipitation.
3. Limit to Operations: higher wind speed, low and high temperature limits and precipitation resulting in ice build-up.
4. Survival Conditions: high winds, extreme temperatures, snow and/or ice accumulation and hail.

Additionally, requirements are identified for seismic and lightning strike events.

3.1 Operational Environment

The defined operating conditions for the antennas are shown in Table 3-1,

Table 3-2 and

Table 3-3.

Table 3-1 Precision Operating Conditions [AD04]

Parameter	Req. #	Value	Traceability
Solar Thermal Load	SBA1411	Night time only; no solar thermal load within last 2 hours.	SYS2411
Wind Speed	SBA1412	0 ≤ W ≤ 5 m/s average over 10 min time. 7 m/s peak gusts.	SYS2412
Temperature	SBA1413	-15 C ≤ T ≤ 25 C	SYS2413
Temperature Rate of Change	SBA1414	1.8°C/Hr.	SYS2414
Precipitation	SBA1415	No precipitation.	SYS2415

Table 3-2 Normal Operating Conditions [AD04]

Parameter	Req. #	Value	Traceability
Solar Thermal Load	SBA1421	Exposed to full sun.	SYS2421
Wind Speed	SBA1422	W ≤ 7 m/s average over 10 min time. 10 m/s peak gusts.	SYS2422
Temperature	SBA1423	-15 C ≤ T ≤ 35 C	SYS2423
Temperature Rate of Change	SBA1424	3.6°C/Hr.	SYS2424
Precipitation	SBA1425	No precipitation.	SYS2425

Table 3-3 Limit to Operating Conditions [AD04]

Parameter	Req. #	Value	Traceability
Wind	SBA1431	W ≤ 15 m/s average over 10 min. W ≤ 20 m/s gust.	SYS2432
Temperature	SBA1432	-20 C ≤ T ≤ 45 C	SYS2433
Precipitation	SBA1433	Any precipitation rate that does not result in accumulation of ice on the antenna structure.	SYS2434

Table 3-4 Survival Conditions [AD04]

Parameter	Req. #	Value	Traceability
Wind	SBA1441	0 m/s ≤ W ≤ 50 m/s average.	SYS2441
Temperature	SBA1442	-30 C ≤ T ≤ 50 C	SYS2442
Radial Ice	SBA1443	2.5 cm	SYS2443
Rain Rate	ENV0344	16 cm/hr over 10 min	
Snow Load	SBA1444	25 cm	SYS2444
Hail Stones	SBA1445	2.0 cm	SYS2445
Antenna Orientation	SBA1446	Stow-survival, as defined by designer	

4 DESIGN OVERVIEW

The design produced in the previous study, [RD04], was based around an existing mount designed for a 10m satellite communications antenna and a scaled down version of the 18m elevation assembly. This configuration required the elevation axis to be significantly offset from the azimuth axis in order to allow the bottom of the primary reflector to clear the pedestal at low elevation angles. This offset meant that the shortest baseline that could be achieved was 14.8m, Figure 4-1, the requirement of 11m could not be met by the design.

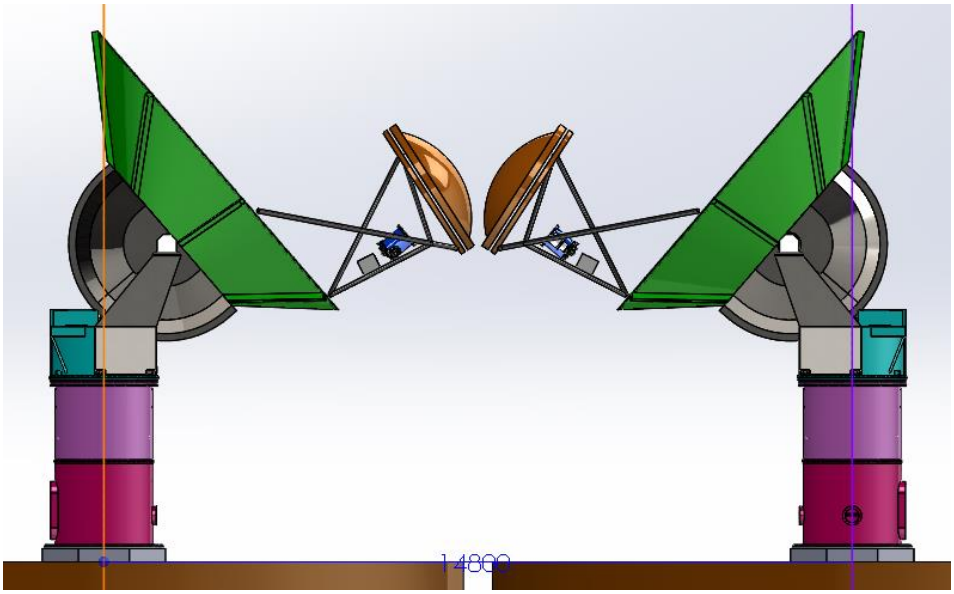

Figure 4-1 Previous 6m Design showing minimum baseline of 14.8 m

The Phase 2 design presented in this document began by determining the geometry required to meet the minimum baseline of 11m and then developing a structure based on that geometry. The defined optical geometry sets the envelope of the elevation assembly; primary and secondary reflector sizes, shapes and relative locations. In order to meet the requirement the distance from the extreme points of the elevation assembly to the elevation axis plus any offset of the elevation axis from the azimuth axis must be <11m/2. To determine the location of the axes on the elevation assembly Ø11m circles centred on the extreme ends of the primary and secondary reflectors were sketched on the model, Figure 4-2, the area outlined in red delineates the zone the two axes must pass through.

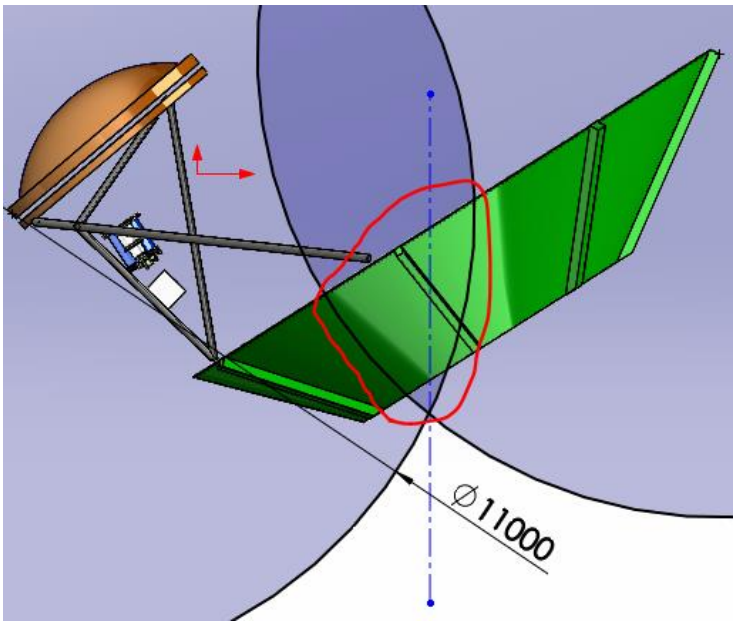

Figure 4-2 Location of Elevation Axis to meet 11m minimum spacing.

This geometry could obviously not be accommodated with the reference design, Figure 4-3.

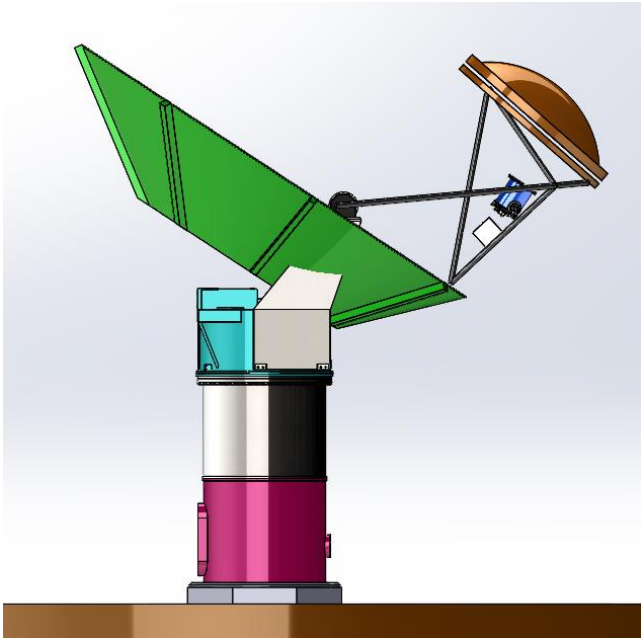

Figure 4-3 Geometry required to meet 11m baseline.

It was recognized that the required geometry looked very much like that of the 15m design study that was produced by NRC in ngVLA Memo #26, Figure 4-4. In that design the elevation axis was placed very close to the rim of the primary reflector with a wraparound azimuth structure supported on a wheel and track.

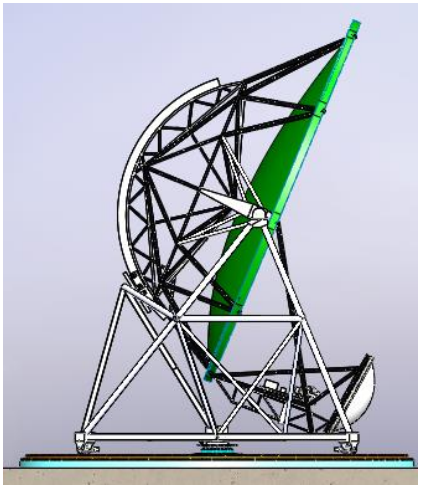

Figure 4-4 NRC 15m Design Study

The proposed design presented in this document utilizes a yoke-style mount supported on a slewing ring and pedestal with a single piece rim supported primary reflector supported on a monocoque BUS with steel sub-frames. Figure 4-5 to Figure 4-9 show the latest iteration of the proposed ngVLA-6m design. A close packing distance of 10.6m has been achieved, Figure 4-6 shows the sweep radius for the elevation structure.

Note that rack and pinion drives are shown for both the azimuth and elevation axis, however the drive type has not been selected and further discussion on drives is provided in 6.

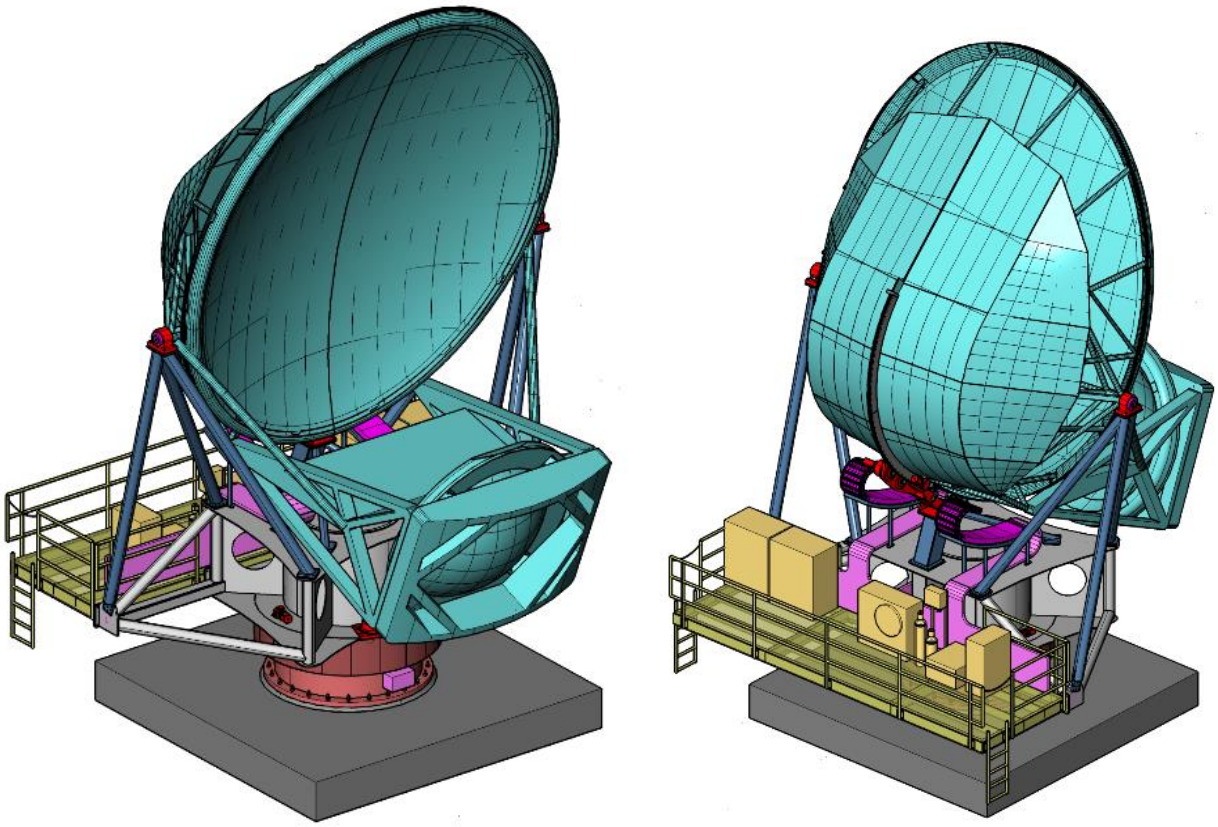

Figure 4-5: 6m Antenna Design Concept

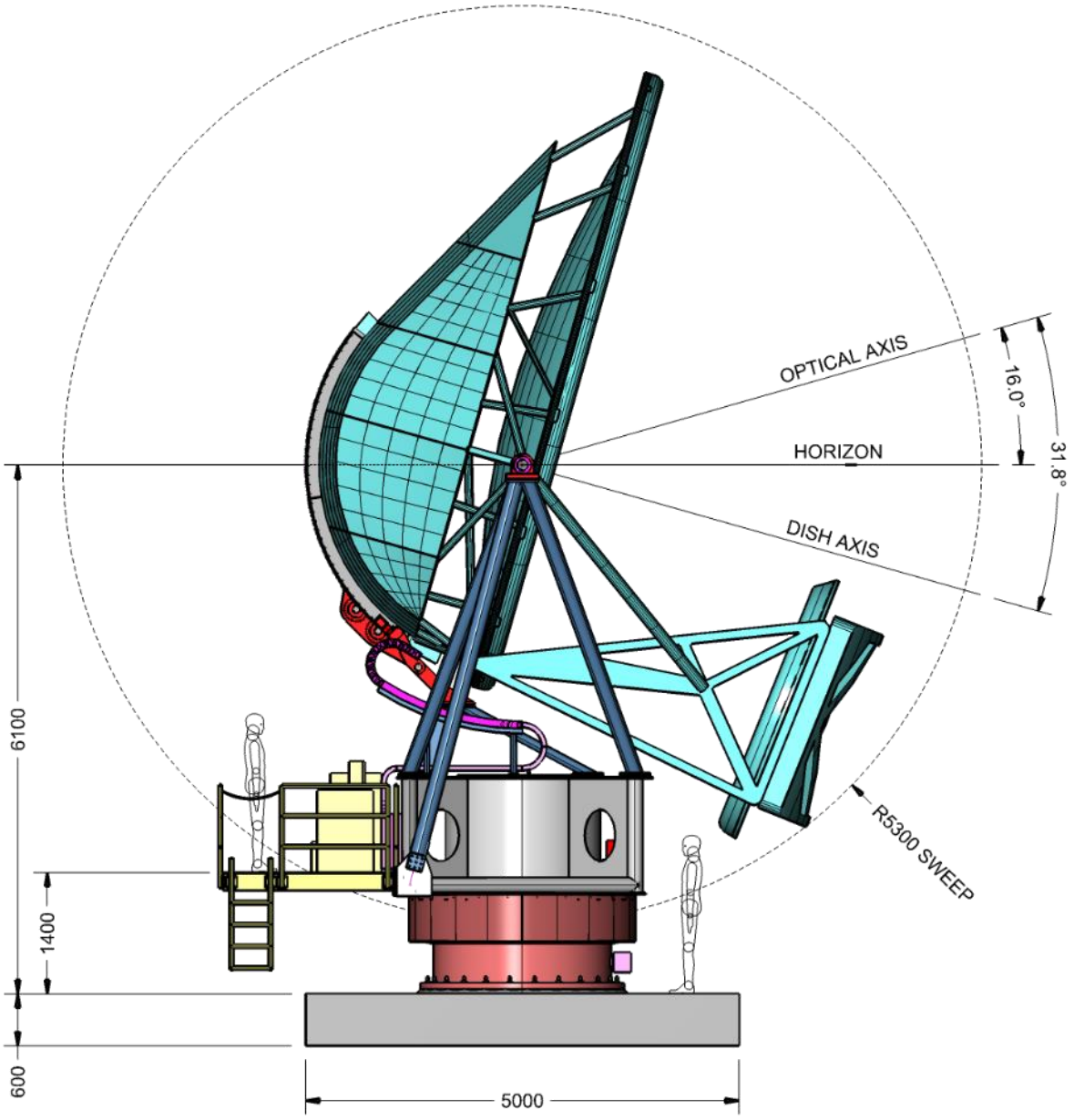

Figure 4-6: Antenna side view at 16deg elevation

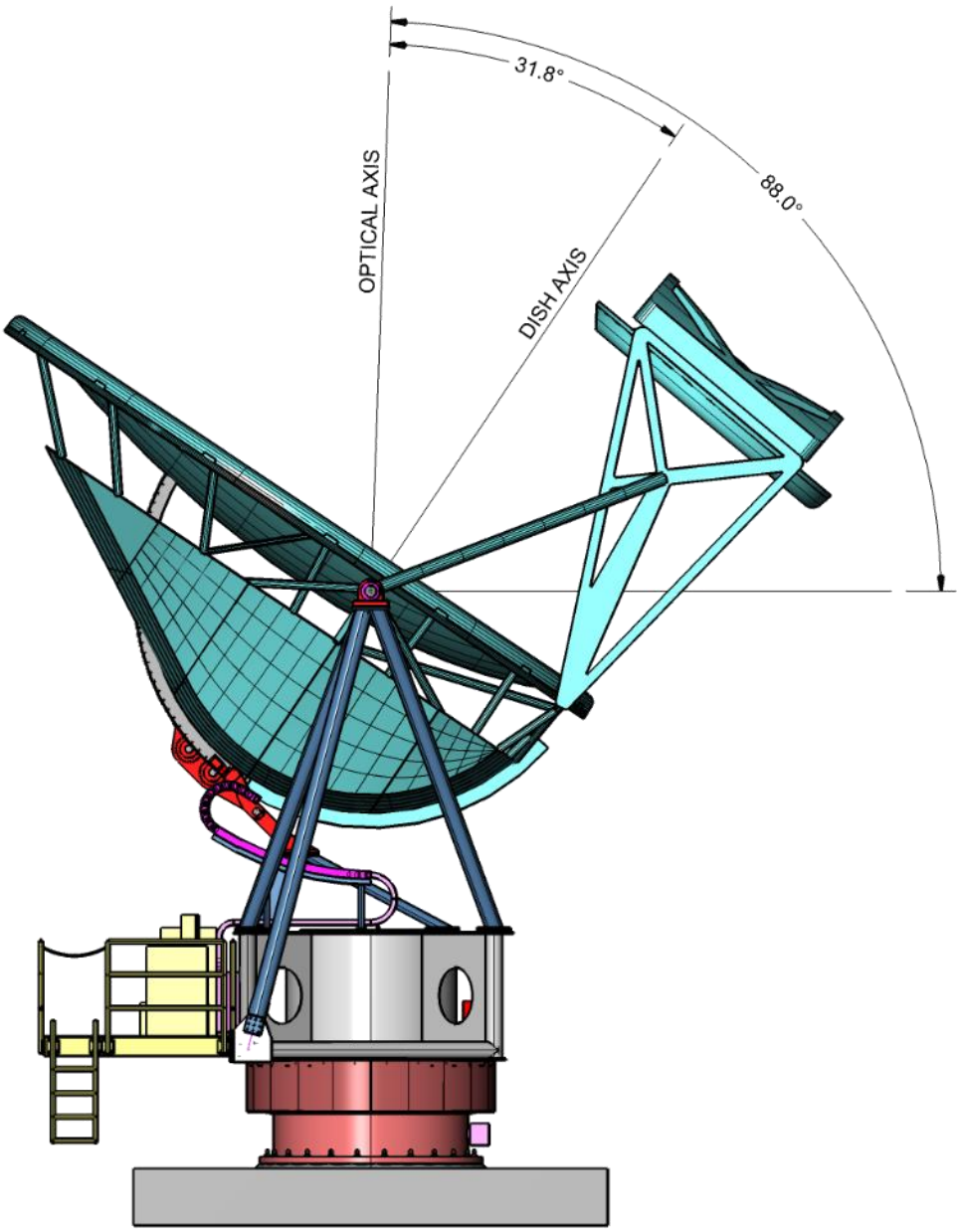

Figure 4-7: Antenna side view at 88deg elevation

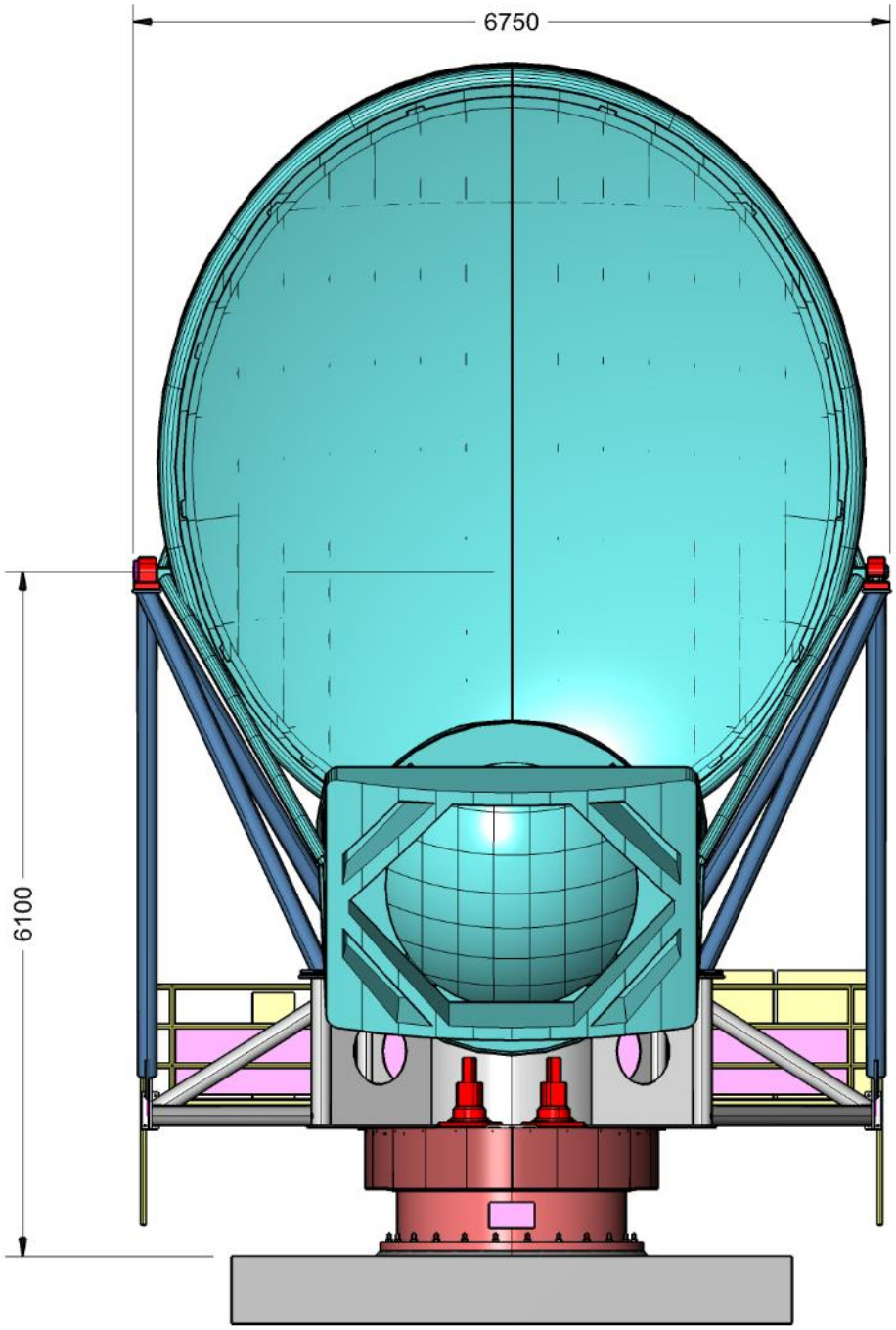

Figure 4-8: Antenna front view

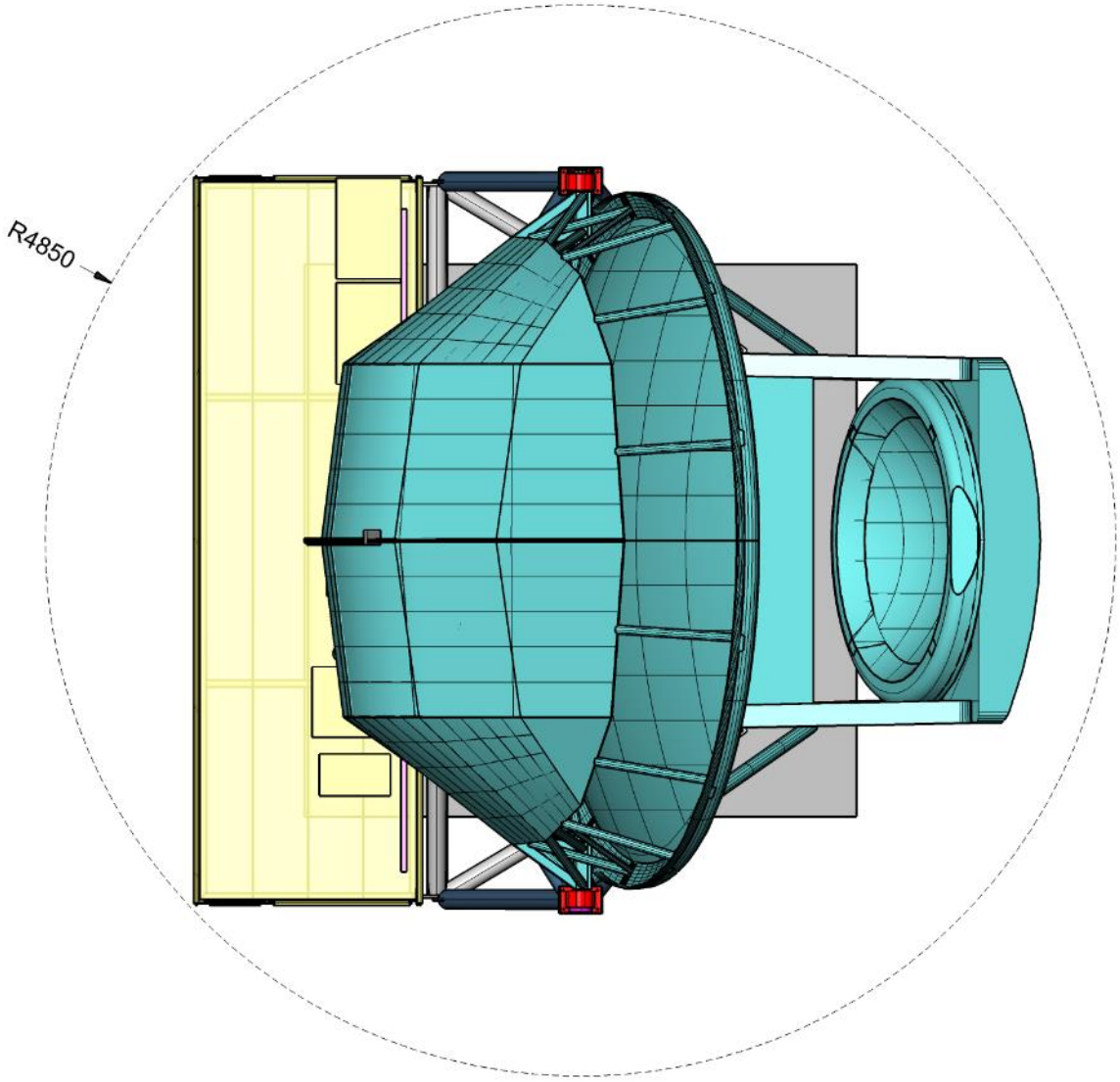

Figure 4-9: Antenna plan view

The following sections detail the development work and current status of this design.

4.1 Elevation Rotating Assembly

4.1.1 Primary Reflector Surface

The path from the DVA style primary to the 6m ngVLA primary starts with the need to reduce surface distortions. The DVA style primary reflector surface has a sheer connection at its centre. While this connection is great at its job of reducing the mass and complexity of the BUS on the DVA style reflector, it does also introduce some stresses into the reflector surface. Operating at frequencies up to 116GHz, it is critical to reduce stresses (and thus distortions) in the reflecting surface as much as possible. In fact this was already recognized on the 15m design study done earlier (see Figure 4). On the 15m design the primary surface experiences self-weight induced stresses only, the inner backup structure (BUS) is a self-contained steel tube structure which supports the drive arc and the elevation bearings, and the outer backup structure (OBUS) consists of carbon tubes that radiate from the upper edge of the BUS to the outer edge of the primary reflector rim. There is also a sheer connection located above each of the primary elevation bearings.

The 6m ngVLA design is derived from the 15m ngVLA design study. This was not initially the case, but once the design constraint of the close packing distance of 11m maximum was fully considered, it became evident that the elevation axis needed to be located near the primary rim, which then drove the design towards the solution found earlier with the 15m.

4.1.1.1 Rim Design

The ngVLA 6m primary is supported by a series of discrete points, similar to the DVA style, but with some improvements. Considering the principles behind homology the ngVLA 6m rim design better distributes the point load from the support legs and thus reduces the magnitude of the hard spots created by the discrete support points (the outer back structure or OBUS). Figure 4-10 is a cross section through the rim and support tube. The green surface is the primary surface with integral rim. The Composite Backing Piece (CBP) brown in Figure 4-10, serves to stiffen the rim and to provide a mounting point for the OBUS. The OBUS legs attach to the primary in a similar manner to the DVA reflector through a ball joint which provides a “pinned” support, eliminating the transfer of moments into the reflector surface.

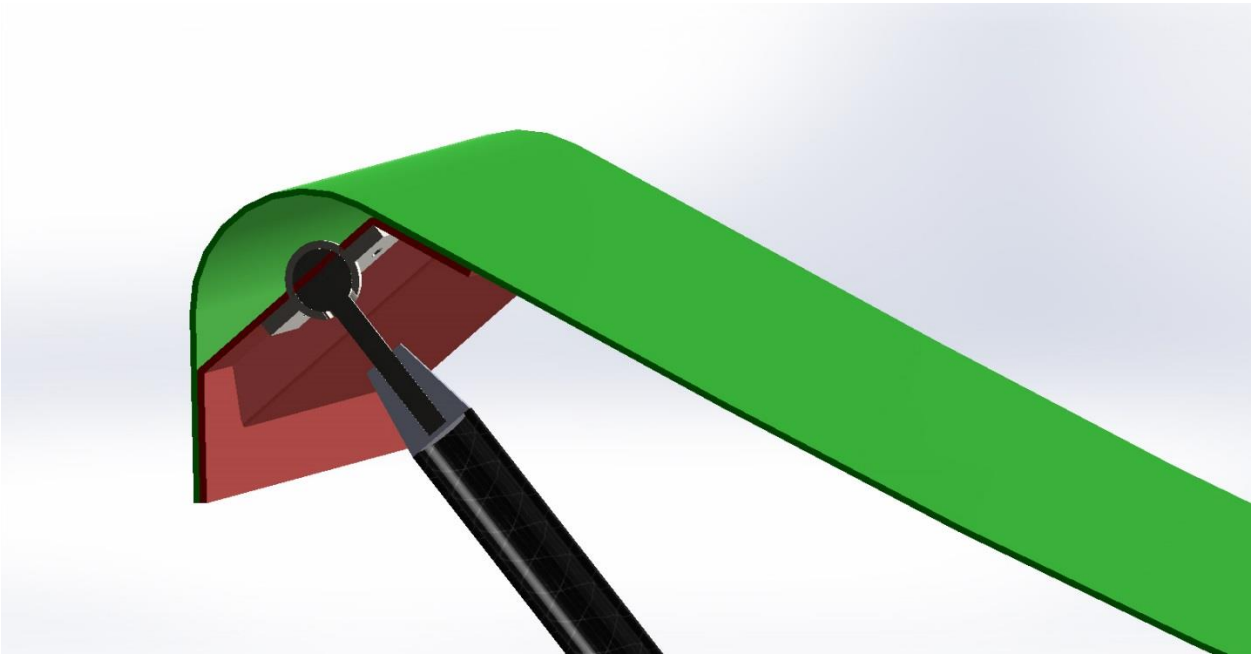

Figure 4-10: Cut through the primary rim at a support leg

The main intent of this support structure is very similar to the DVA structure, but there are some important differences:

1. The rim shape is now rounded instead of squared off. The “best” shape of the primary rim is one which provides maximum stiffness in out of plane bending between support points while at the same time providing tangential support for the rim-supported surface. It is not obvious what this shape should be, since the ‘beam’ defined by this edge structure is not straight, but curved, and such a beam does not have a simple solution. Through FEA analysis, the current curved structure has proven to be just as stiff as the earlier rectangular sections (of the DVA), but with the added advantage of not requiring core due to its tightly curved shape. Removing the core helps reduce part complexity, fabrication costs, and (most importantly) reducing the coefficient of thermal expansion (CTE) of the dish rim by about 50%. This is a particularly important gain.
2. The OBUS legs are individual instead of in pairs, individual legs are far easier to adjust than paired legs and they represent a better solution from a thermal (CTE) point of view. This is discussed in detail in 4.1.2.
3. The ball-joint connects to the composite backing piece at a point isolated from the primary surface. On the DVA reflectors the OBUS legs connected to the Dish Rim Connectors (DRC’s) which besides being large, complicated, and expensive, were connected directly to the reflector surface. This had some advantages, but most critically the considerable disadvantage of creating a ‘hard spot’ on the surface. On the new design the CBP incorporates a recess at the centre of which the ball joint is located. The moulded recess provides the ability to provide both local stiffness (the end flats of the recess act as transverse

beams), and a ‘tuneable’ membrane surface to which the ball joint is bolted. Tuneable meaning the stiffness of this surface can be adjusted in the direction parallel to the line of action of the struts. All of this is important because the prime objective is to preserve the shape of the primary reflector, not to prevent all solid body translation and rotation (homology principle). In other words it is just as important to try and spread-out or reduce the amplitude of the high points (support points) as it is to try and reduce the amplitude of the low points (the infinite stiffness approach).

4. The ball-joint connectors are all the same. With total reflector numbers of 19 antennas in the SBA, the part count will be high enough to consider various fabrication scenarios from cast-metal-post-machined parts to compression moulded carbon parts.
5. Sheer connection (*early concept*), (X direction constraint) between the primary surface and the BUS is located on both sides of the reflector on top of the elevation bearing support structure. The left hand image in Figure 4-11 shows the elevation structure in its vertical position. In this position, without diagonalization of the OBUS (red tubes) if the sheer connection was not present the reflector surface would not be properly supported (the OBUS tubes are not diagonalized because of thermal expansion over-constraint issues). At the same time transverse (Y) constraint (into the page for left hand and middle images) is not desired, so the sheer connection is shown as a double-hinged planer structure allowing differential movement in Y to take care of any CTE differential between the dish surface and the BUS, and to decouple any transverse (Y direction) stresses induced into the BUS from the dish surface. This system is the similar to that proposed in the 15m design shown in Figure 4-4. An additional need has been identified to soften the hard spot created by the very stiff structure around the elevation axis structure (to understand this, picture the dish in the ‘bird bath’ position with the dish rim horizontal). Because the rest of the primary reflector is supported on the longer and softer OBUS tubes it is desirable to make the connector on top of the elevation bearing less stiff in the Z direction without compromising its stiffness in X. The current design consists of two sheer connection double hinged blades, instead of the one used on the 15m design, mounted on compliant cantilever bars reducing the load concentration and softening the hard spot. In addition the size of the attachment surface to the CBP was increased similar to the OBUS legs connection, Figure 4-10, which allows tuning of the stiffness of this surface as well. The down-side with these methods is that the stiffness in X and Z are not entirely decoupled and reducing the stiffness of the cantilever bars as well as the CBP surface both also effect the stiffness in X and thus the dish deformations in X.

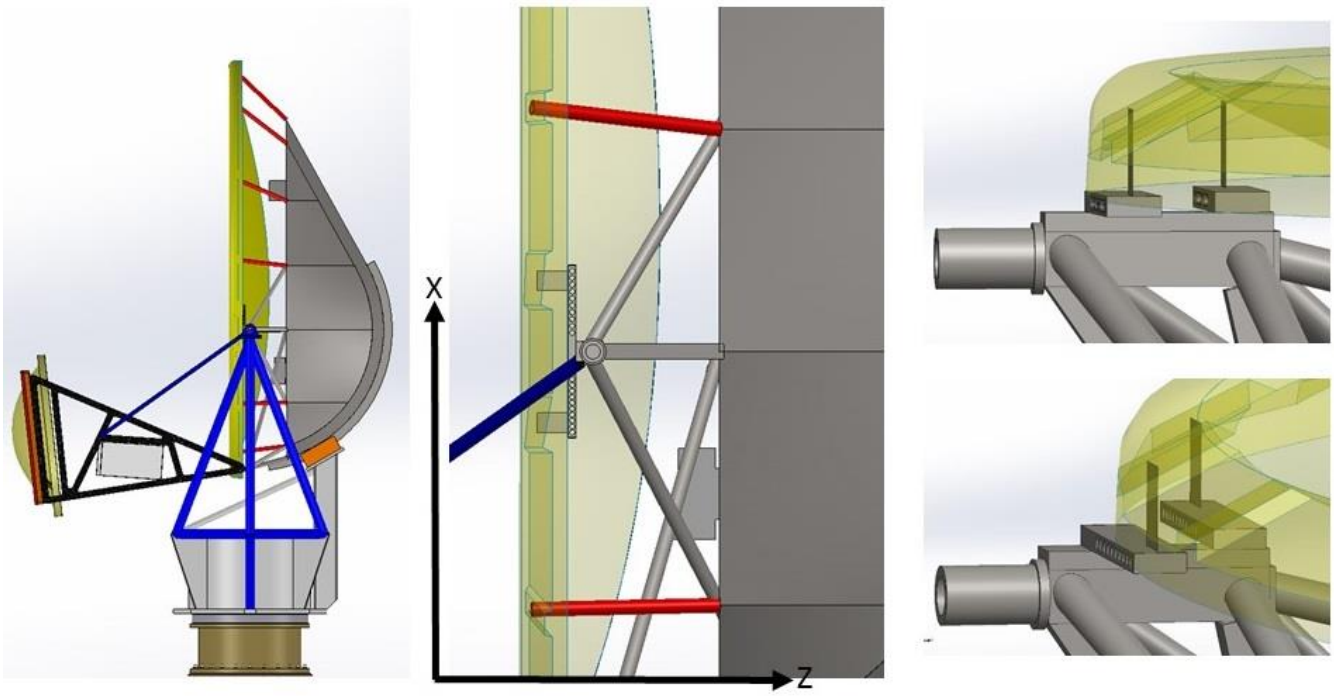

Figure 4-11: Sheer connection on the ngVLA-6m primary surface

6. Sheer connection concept (*new concept, 2021*). Due to primary surface distortion issues caused by the relative stiffness in the Z direction of the sheer connection detailed in (5) above, a new idea was developed. This concept is simple, to add a diagonal member, but was not initially tried because of concerns with differential thermal expansion that could occur. Some additional FEA modelling showed that this was not going to be a big problem, so the solution was adopted. In addition to adding a diagonal member to replace the older 'blade' concept, all the OBUS legs were moved around the rim by half a spacing. This was done to allow the placement of the OBUS legs near the elevation axis while still maintaining a nearly uniform leg spacing, and also to improve the primary surface shape through two additional homology-like changes. With the OBUS legs moved by one-half of a leg spacing the legs no longer land on internal bulkheads in the BUS structure which further softens this support point (and therefore helps reduce the 'hard spots' that these support point causes in the primary reflector). Furthermore, the elimination of the OBUS strut on the centreline of the BUS structure where the BUS is very stiff eliminates two even harder spots in the primary reflector that previously occurred at these two locations. Figure 4-4-12 illustrates these structural changes. The left hand image gives an overall view of the telescope. The middle image shows a profile view around the elevation axis. The shifted OBUS legs are clearly seen (now on either side of the elevation axis) along with the one diagonalized 'bay' between the two OBUS legs above the elevation axis in this view (actually two of course, one on either side of the X-Z centre plane). The right-hand image in Figure 4-4-12 shows the OBUS and BUS in the transverse Y-Z plane (tipped on its side). This view shows the OBUS legs spaced now either side of the centreline

of the BUS structure and also shows an additional diagonal strut that was added to increase the stiffness between the primary reflector surface and the BUS structure in the transverse Y direction. This diagonal was added after normal-mode calculations showed a lower than desired natural frequency due to excess softness in this Y direction.

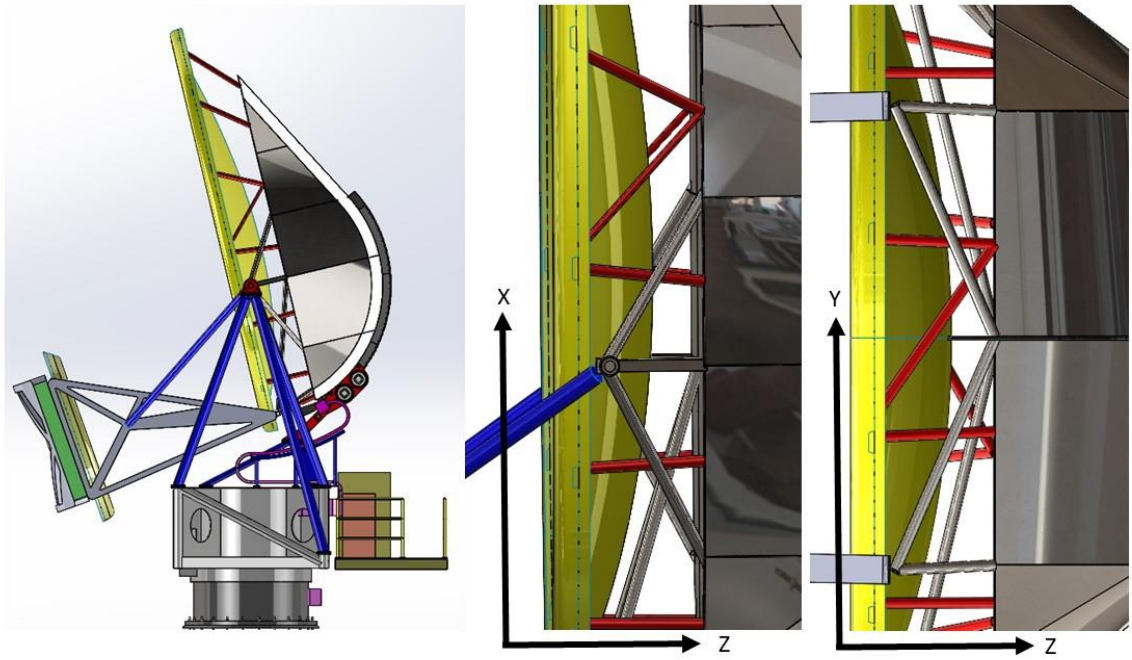

Figure 4-4-12: Revised (May 2021) ngVLA-6m BUS to main reflector support structure.

4.1.2 Backup Structure

4.1.2.1 Inner Backup Structure (BUS)

The Inner Backup Structure (BUS) is the stiff foundation of the elevation structure, it consists of the flat topped cored carbon fibre monocoque structure, Figure 4-13, the elevation drive quadrant (either a drive plate or a quadrant gear depending on the type of drive used), two tripod-type steel structures that support the elevation bearings and two structures supporting the secondary legs.

While the BUS monocoque doesn't actually rotate to a completely horizontal, birdbath, position even at 90^{o} elevation angle, it is still instructive to imagine it in this orientation when considering the beam-in-bending mode. In this orientation, Figure 4-13, the BUS must act as a beam which is suspended from the two elevation bearings. Besides self-weight, loads are fed into this structure at the two secondary support points and at each of the outside corners around the tops surface from the primary

(OBUS) legs. Additionally the BUS monocoque must resist loads from the drive arc which can be considered as a support point but only in the tangential direction.

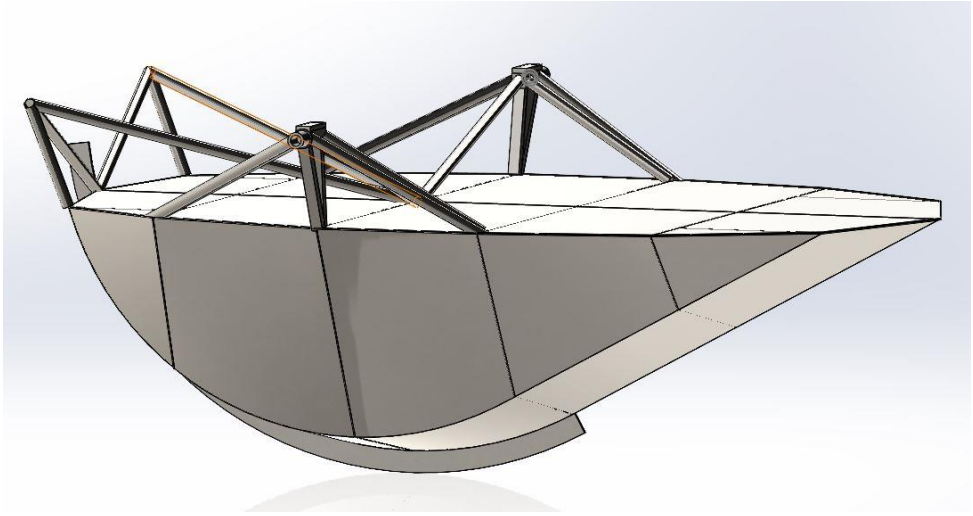

Figure 4-13: BUS structure

The carbon monocoque is constructed with multiple transverse and longitudinal bulkheads to better handle localized loads fed into it by the OBUS and at the tripod attachment points along with the drive arc. This structure could be fabricated from steel, but because the elevation axis is positioned so close to the primary surface (and because the primary and secondary structures are all carbon fibre), it would be impossible to counterbalance this weight without adding counterweights above the primary surface. With a carbon monocoque, the Cg of the current design is very close to the elevation axis.

The CTE of the carbon monocoque, which would be mostly cored with foam core to increase panel stiffness, will be very close to steel (10 versus 12ppm per ^{o}C). This provides a fairly good CTE match between it and the steel mount which minimizes stresses and distortions through temperature changes.

4.1.2.2 Outer Back Structure (OBUS)

Figure 4-14 shows the OBUS, consisting of the red legs connecting the primary surface to the BUS. On the DVA dishes and the 15m design study these legs are individual, with some occurring as triangulated pairs to insure rotational stability about the Z axis. For the ngVLA-6m the OBUS to uses (primarily) single legs that are orientated approximately radially and relies on just two pairs of diagonalized legs to constrain X and Y translation and Z rotation, Figure 4-14, and Figure 4-15.

If the dish was radially symmetric the OBUS could also be radially symmetric and all the OBUS legs could be identical and radially oriented. This means they could all be triangulated pairs and would not

overly constrain the surface during thermal expansion. With a non-radially symmetric structure care must be taken to avoid over-constraining the reflector surface during thermal expansion with the OBUS legs, so consequently only a couple of pairs of legs are diagonalized.

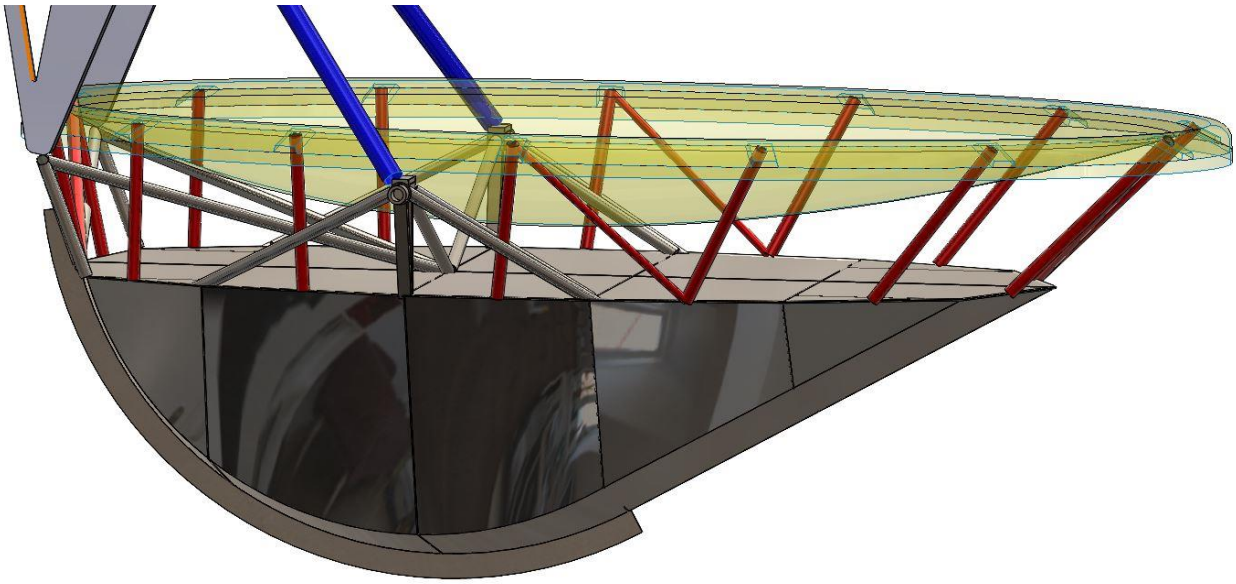

Figure 4-14: Outer back structure, (red legs)

Additionally, to further control primary surface distortion under thermal expansion the OBUS legs are not all made of material with the same CTE. For this conceptual design the OBUS material has been confined to steel for all the legs except the six (plus the diagonal) on the right side of Figure 4-15. Because these legs are somewhat longer than the rest of the OBUS legs, they expand more, if made of the same material. Using carbon the surface distortion under thermal bath temperature change is much less, see **Figure 9-15**. Further refinement such as using blended fibres for some of the composite legs to adjust the CTE will be explored as the design matures.

The elevation axis is not centred on the primary in the X direction, Figure 4-15, and the OBUS legs do not all have the same orientation in terms of 'lay-out' angle but are more vertical on the secondary end. This provides better support on this end where reflector shape is more critical. The BUS is elongated in the X direction away from the secondary to better support the primary reflector on top end. Although support on this end is not as critical as on the end nearest the secondary (due to RF beam weighting), it is still important.

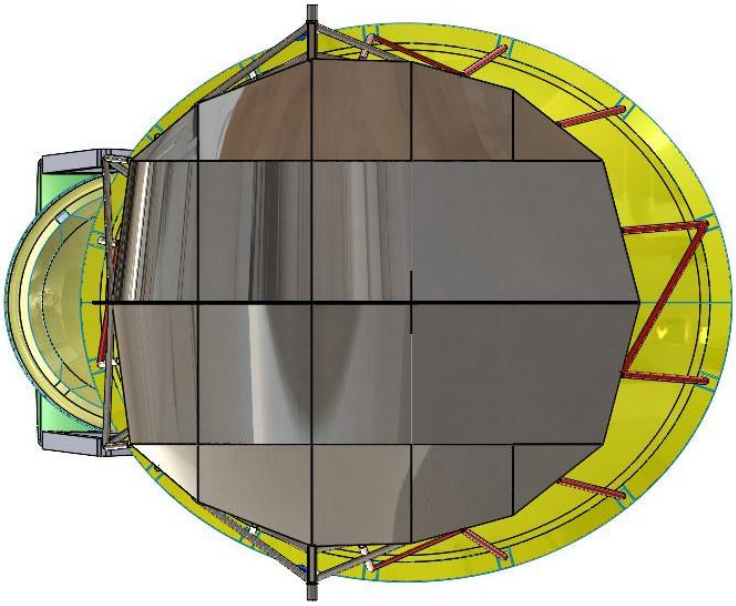

Figure 4-15: Bottom view of the elevation structure

4.1.3 Secondary Support

Secondary support is quite different to the DVA reflector due to the ngVLA-6m being a feed-down design and the size and mass of the feed package relative to the 6m primary reflector (it is the same as used on the 18m antenna). However the length of the feed support structure is much less than on the larger antenna designs and because the primary is so much smaller, it is possible to position a straight feed leg from the secondary support structure to the elevation bearing structure without intersecting the optical path. This same feed support leg on the DVA design had to be positioned a large distance off the central plane of symmetry (the X-Z plane) which complicated the structure.

Figure 4-16 shows the secondary support structure in profile. The principle elements are the carbon fibre truss (gray) which stands on the two support points on the BUS, the forward feed legs (blue) which connect the truss to the elevation bearing structure, the secondary mounting structure (gray and green), the secondary reflector (yellow), and the feed package (not shown).

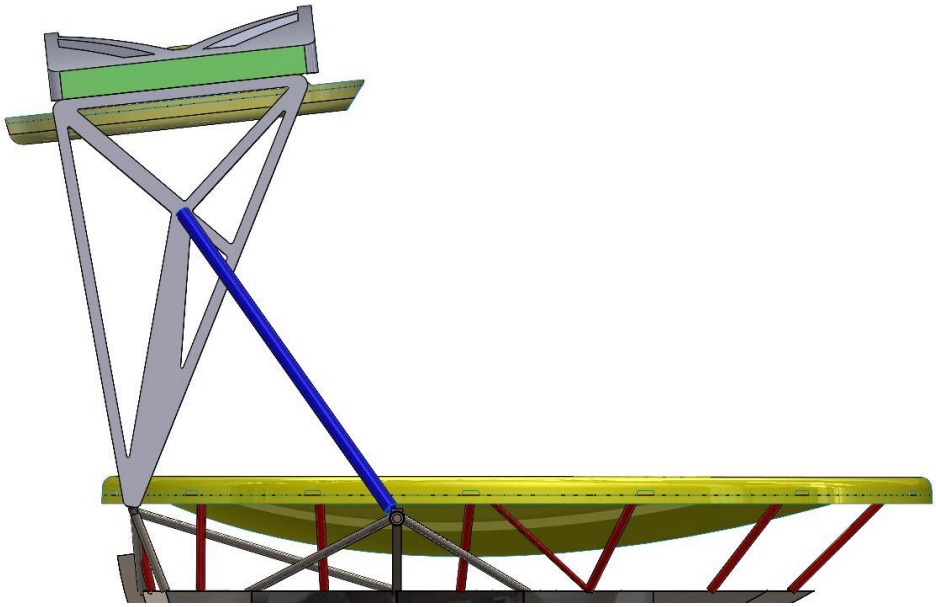

Figure 4-16: Secondary support structure in profile

4.1.3.1 Base support of secondary structure

Figure 4-17 shows the four point support of the secondary structure. In concept it is similar to the DVA except that for the ngVLA-6m the support points are connected directly to the BUS and not connected through the rim of the primary as on the DVA dishes. This helps to further reduce distortions in the primary surface. However, the secondary load cannot be fully isolated from the primary because everything is connected together through the BUS, but the improvement in strain reduction in the primary surface is quite significant.

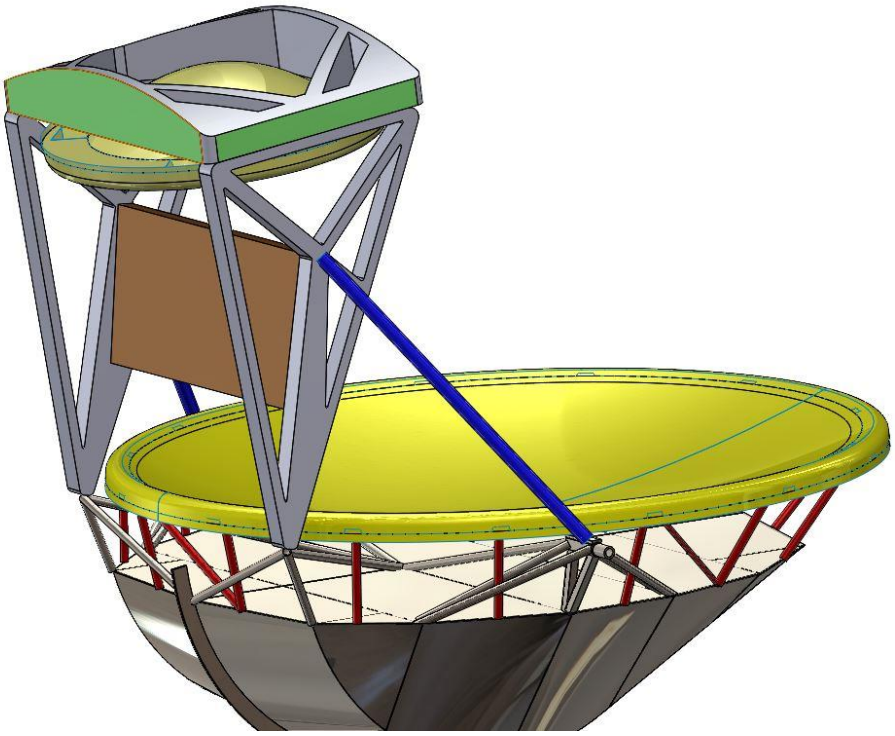

Figure 4-17: Isometric of the secondary structure

4.1.3.2 Side Trusses

On the DVA design the feed and secondary support structure consisted mostly of carbon tubes with separate end connectors. In principle this is fairly easy to implement except that the end connectors can get complicated especially where multiple tubes connect. In an effort to reduce this complexity the 6m design incorporates more planer truss structures such as the side truss. Figure 4-18 shows the side truss structure (latest iteration, optimized using topology optimization techniques). This is relatively easy to mould from carbon fibre and would consist of two parts, the base part and the lid with a shoe-box joint. Where other structures are to be connected to this truss additional reinforcement such as more local laminate layers, bulkheads, or metallic plates would be added to take care of local high stresses and strains (these details are TBD).

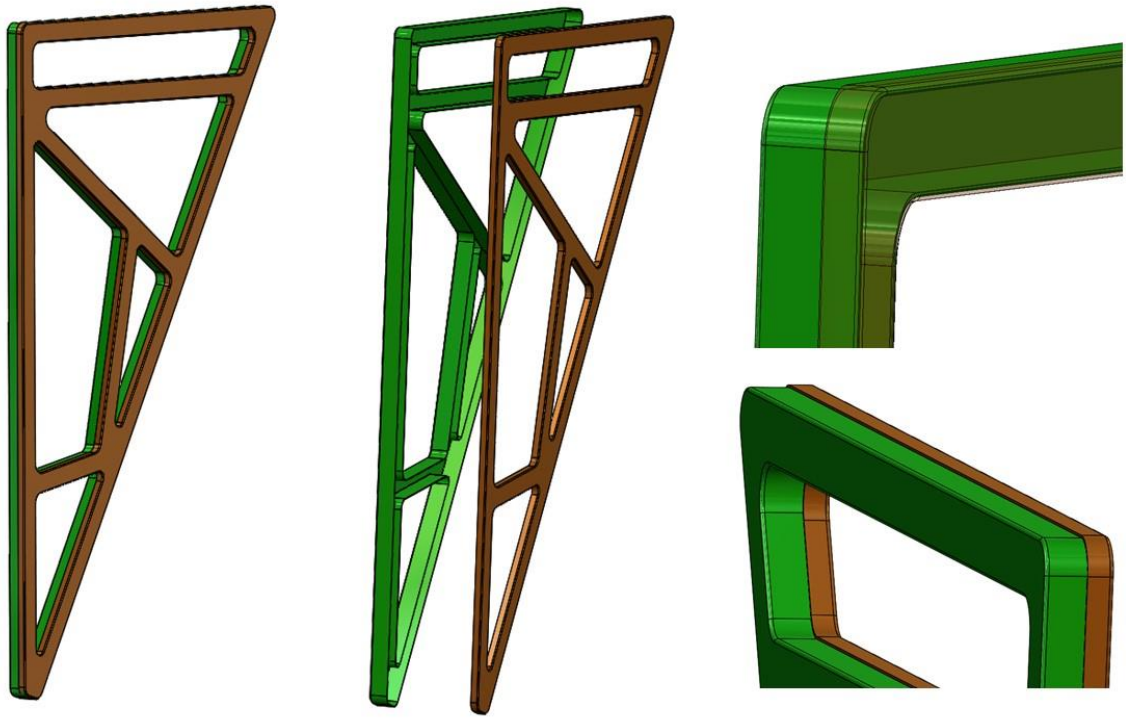

Figure 4-18: Secondary side truss (earlier version shown, but concept is the same)

4.1.3.3 Secondary reflector support structure

This structure (top grey and green structure in Figure 4-17) completes the secondary support structure and ties the two trusses together. As with the side trusses this structure was optimized using topology optimization. It is to be made using the same style of structure shown in Figure 4-18 for the side trusses, and similarly consists of a top and bottom piece, moulded separately, then bonded together. The support of the secondary itself is through a 4 point quasi-kinematic support ('quasi' because there are 4 support points instead of 3). Based on experience with the DVA telescopes, the need to completely isolate structural loads from the reflector surfaces is fully appreciated, especially at the frequency ranges desired for the ngVLA instrument. Figure 4-19 shows the secondary (older version) with its supports. All supports have ball connectors at the secondary reflector end so that no moments are transferred to the reflector. Support number one is fixed in all axis at the top (bottom right support). Proceeding clockwise around the reflector support number two provides transverse (Y direction) freedom but constrains X and Z translations as well as X and Z axis rotations. Supports three and four have ball connections on both ends, their role is to provide Y axis rotational constraint as well as defining the reflector plane. The only possible load transfer from the support frame would be a twisting about the plane of the reflector rim, but this is unlikely to occur with a structure symmetric about the X-Z plane. The secondary reflector should now only experience self-gravity induced deflections. See also section 9.1.2.1 for the updated secondary reflector rim design details.

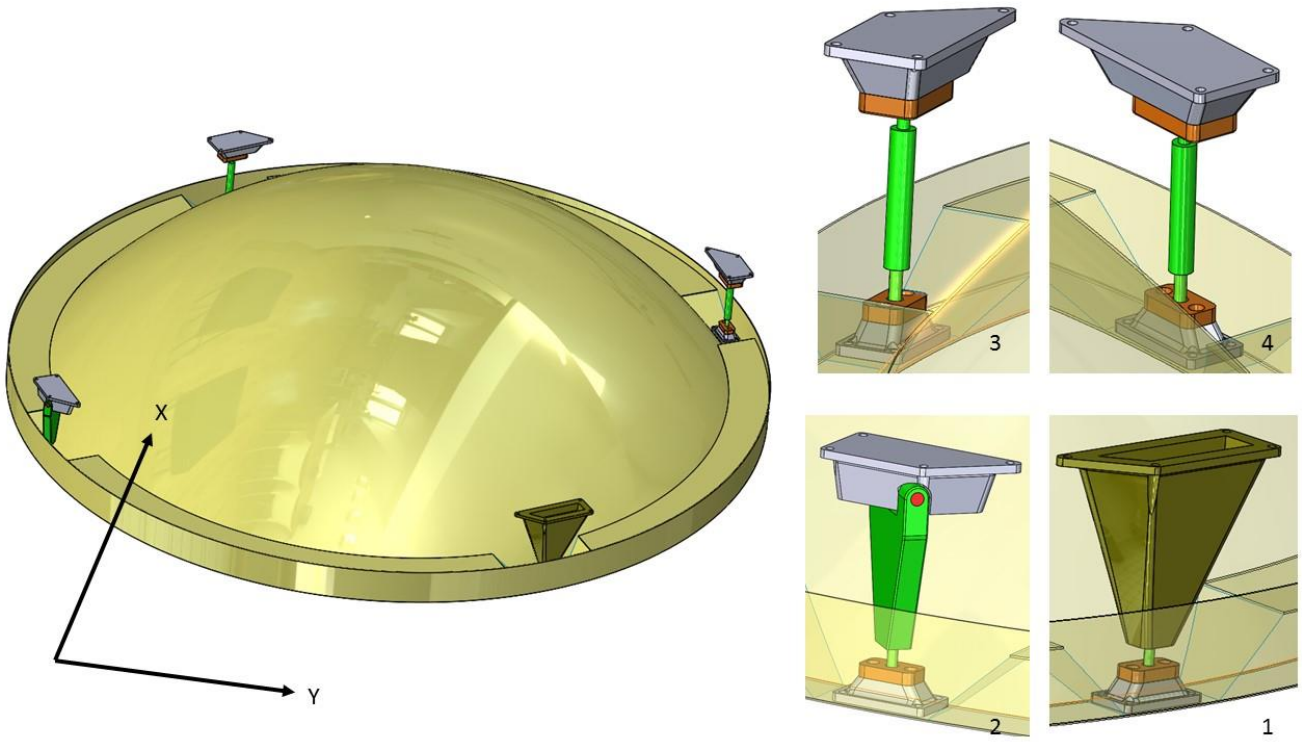

Figure 4-19: Secondary kinematic support

4.1.3.4 Feed package and indexer support

(*Initial Concept*): The feed package and indexer support would be through a corrugated composite platform designed to be adequately stiff where the indexer rails attached to the platform. This structure would also act as a diagonal brace between the two feed and secondary support trusses. Figure 4-20 shows the proposed structure. Connections at the platform ends would be through-bolts into embedded backing plates inside the side trusses (details TBD). Similarly connections to the indexer would be through-bolts. This is another reason to adopt a corrugated versus a cored structure; the ability to easily accommodate through-bolts and to reinforce for local loads.

(Current Concept): A new concept by Sightline Engineering incorporates transverse steel truss structures for the support of the linear indexer mechanism.

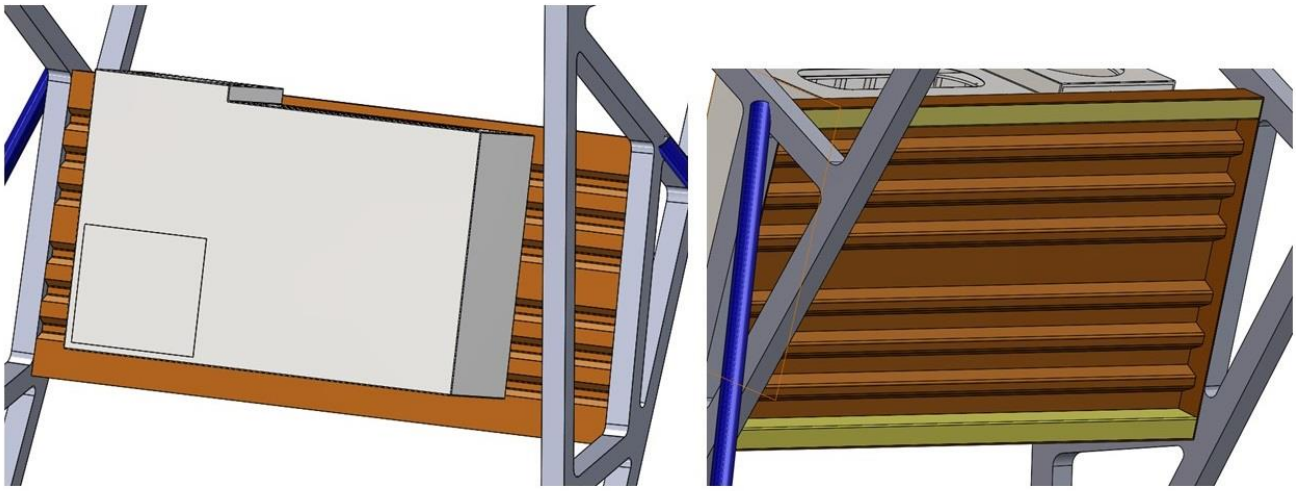

Figure 4-20: Feed and indexer support

4.1.3.5 Weight and Centre of Gravity

The preliminary weight and C of g of the elevation structure is as illustrated in Figure 4-21.

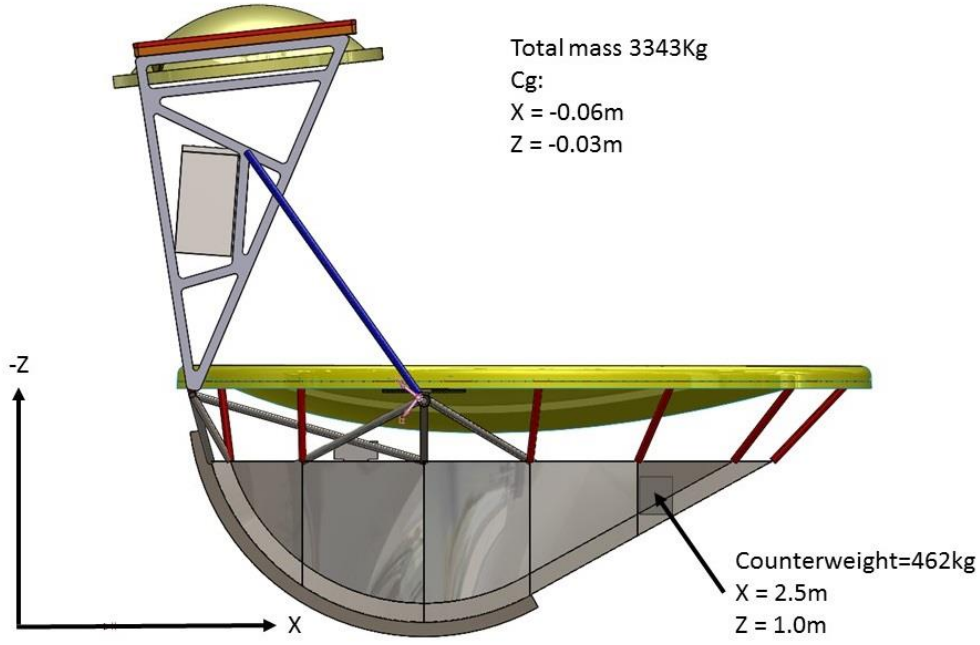

Figure 4-21: 6m elevation structure weight and C of g.

The origin in Figure 4-21 is the elevation axis. The total mass of the elevation structure including feeds and counterweight is 3343kg. Currently there is a 462kg counterweight shown, but this will change depending on where the auxiliary equipment (such as the vacuum pump, etc.) is located. Figure 4-21 shows a vacuum pump located to the left of the elevation axis on top of the BUS, but at the moment it has zero mass in the model. If it and some of the other auxiliary equipment can be located to the right of the elevation axis, then the mass of the counterweight can be reduced.

4.2 Mount

4.2.1 Overview

The proposed mount design utilizes a yoke-style mount supported on a slewing ring and pedestal, Figure 4-22. A key restriction on the ngVLA 6m design is the close-packing specifications, which necessitate that the elevation axis is located very close to the rim of the dish in order to limit the sweep envelope of the ERA and secondary support. Having the elevation axis at this location requires that the mount has very widely spread yoke arms to support the elevation axis, and thus the yoke is much larger relative to the dish compared to most radio telescopes.

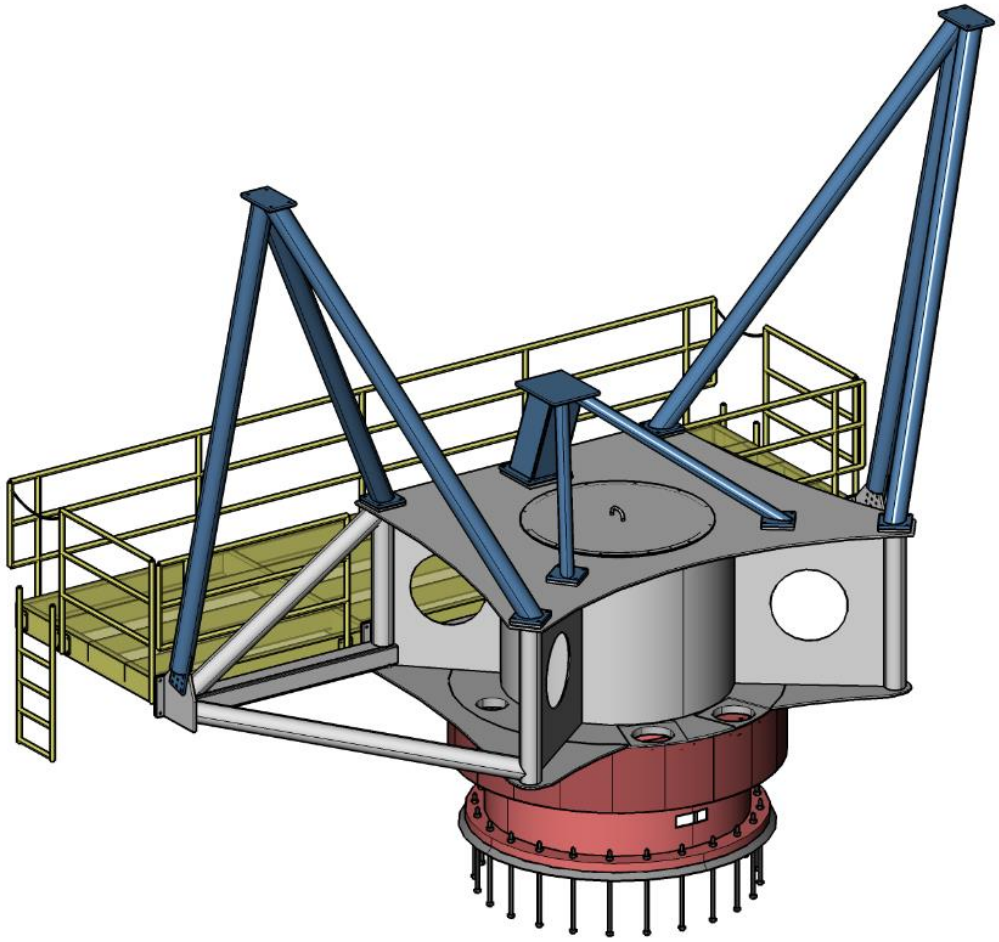

Figure 4-22: Mount concept

4.2.2 Design Evolution

One of the key initial design trades was whether to use a slewing ring or wheel and track arrangement for azimuth rotation. Early concepts for each option are shown in Figure 4-23 below. The slewing ring design has the advantages of being more compact, and arguably simpler to construct and maintain since the azimuth bearings and drives are well contained and sealed. The foundation interface is also simpler. The wheel and track design provides a stiffer structure for a given weight due to the large base diameter.

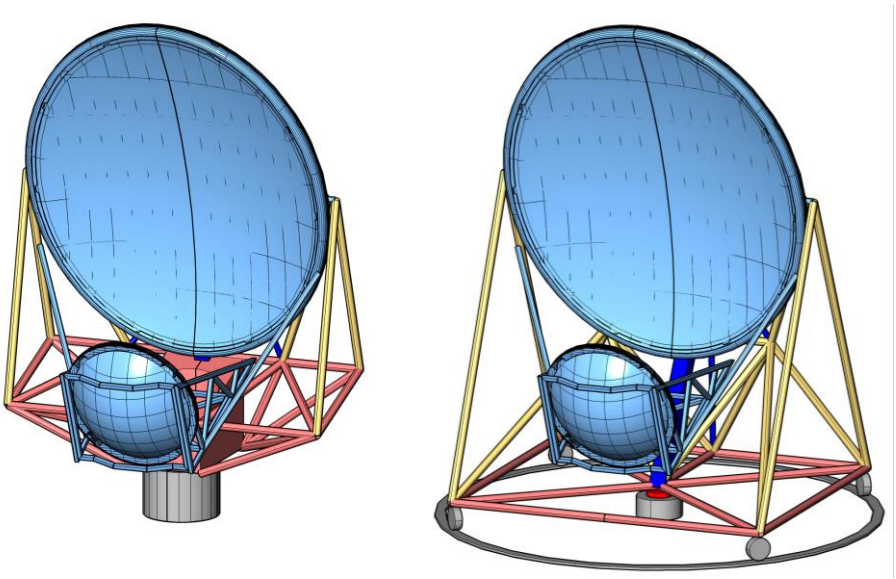

Figure 4-23: Early concepts for slewing ring (left) and wheel and track (right) mounts

Preliminary FEA was carried out for simplified models of both options. It was found that for equivalent weight the wheel and track option had natural frequencies approximately 50% higher than the slewing ring option. However, the performance of the slewing ring option was sufficient to meet the project requirements and thus was selected for further development due to the mechanical benefits.

Figure 4-24 illustrates the topology evolution of the mount, described as follows:

- Top left: Initial concepts were based primarily on a frame structure, with significant structure situated near the rear of the mount (behind the elevation drive) in an effort to increase the fore/aft stiffness of the mount due to frontal wind loading of the ERA.
- Top right: It was found that the structure at the rear of the mount was not particularly effective, so it was removed and the lower portion of the yoke frame was stiffened.
- Bottom left: As the lower portion of the yoke became increasingly complex the frame structure was replaced with a monocoque structure in order to simplify fabrication and increase stiffness.

- Bottom right: The monocoque structure was updated to have a flat deck to accommodate on-board equipment and simplify fabrication, and it was found this did not significantly reduce the stiffness. The elevation axis was moved lower on the dish in order to facilitate ERA balancing, which resulted in the additional benefit that the mount height was reduced.

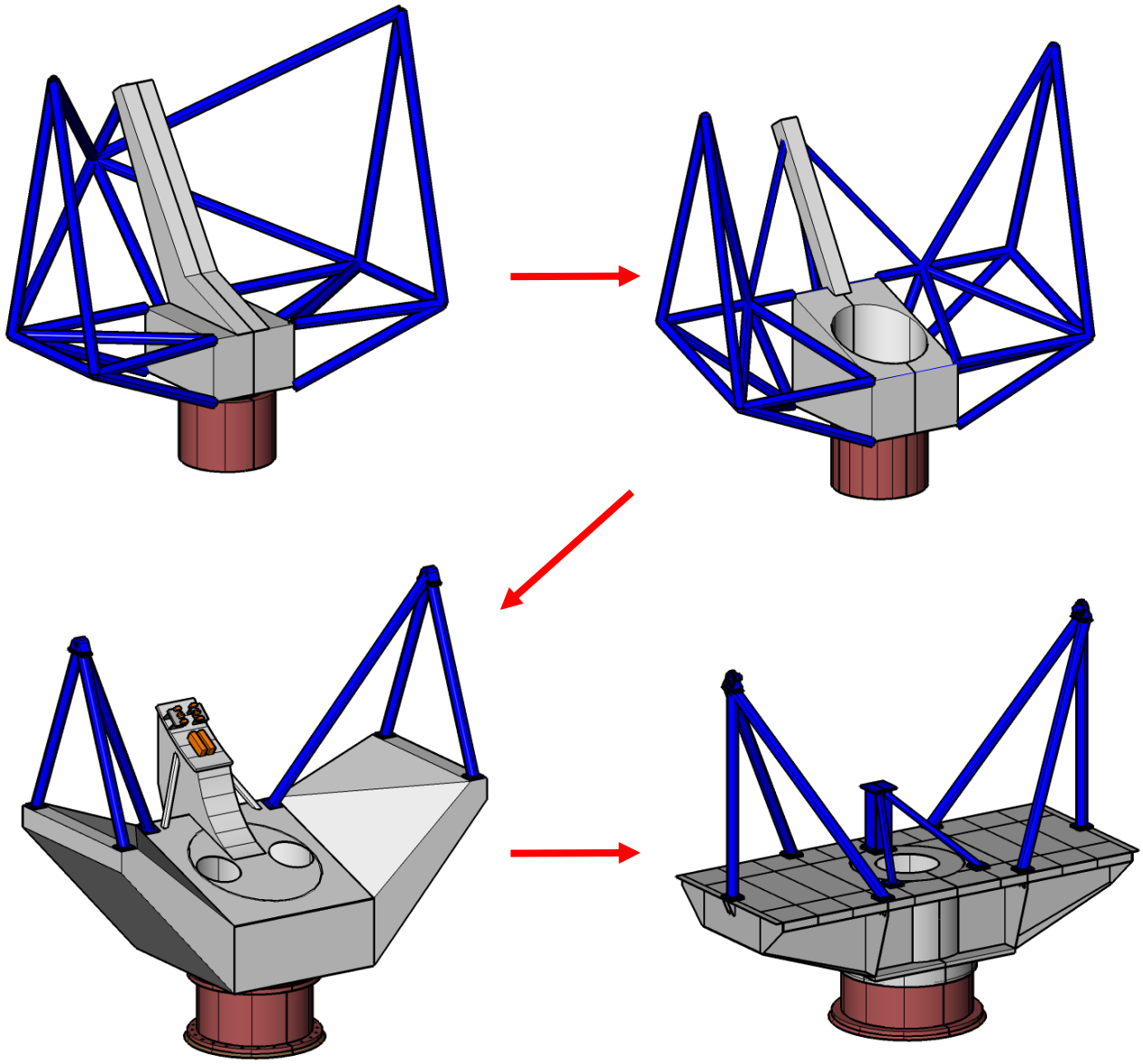

Figure 4-24: Topology evolution

4.2.3 Structure

Error! Reference source not found. shows the breakdown of the main structural elements. The lements shown all have bolted interfaces to one another. The main yoke element and pedestal structures will have machined mounting interfaces at the azimuth bearing and drive interfaces. Additional machining operations may be required to achieve locally flat bolted interfaces.

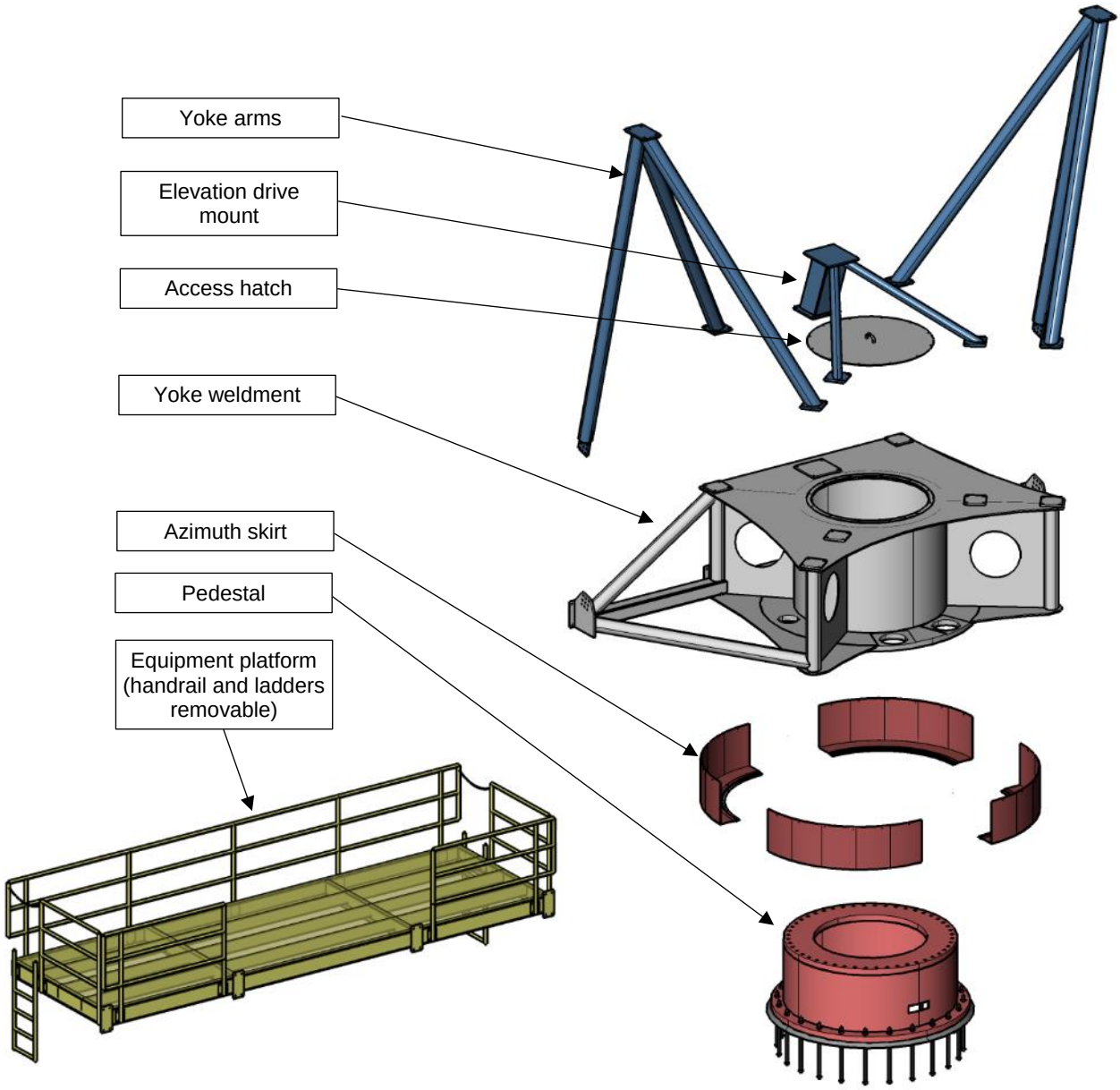

Figure 4-25: Structural elements, exploded

4.3 Bearings

4.3.1 Azimuth Bearing

The azimuth bearing utilizes a slewing ring that is nominally 2.0m in diameter. General requirements for the slewing ring are zero tilting backlash which is achieved by preloading the balls or rollers, and high tilting stiffness. Common rolling element arrangements for slewing rings are shown in Figure 4-26 and include 1) single-row ball bearings 2) cross roller bearings and 3) three-row roller bearings. Slewing rings generally increase in stiffness and cost in this order.

Figure 4-26: Slewing ring types - single row four-point contact (left), cross roller (middle), three-row roller (right)

The bearing size and type are governed by stiffness requirements. A preliminary stiffness specification of 6.0e+9 N-m/rad was used in order to limit the influence of bearing stiffness on point error (this is described further in the analysis section below). SKF and Rotek were both consulted for bearing selection based on this specification. SKF proposed a cross-roller bearing which achieved this stiffness via high preload. Rotek proposed a three-row roller bearing which could achieve this stiffness with zero preload. Rotek also indicated that the single-row and cross-roller options were both reasonably close to meeting the stiffness specification, and could be considered an option in the future.

Figure 4-27 shows a general arrangement of the azimuth bearing relative to the pedestal and yoke structures. The bearing shown is a cross-roller type bearing with an external gear (not shown) for the azimuth drive. The gear and bearing are protected from the exterior environment via a removable skirt and brush seal.

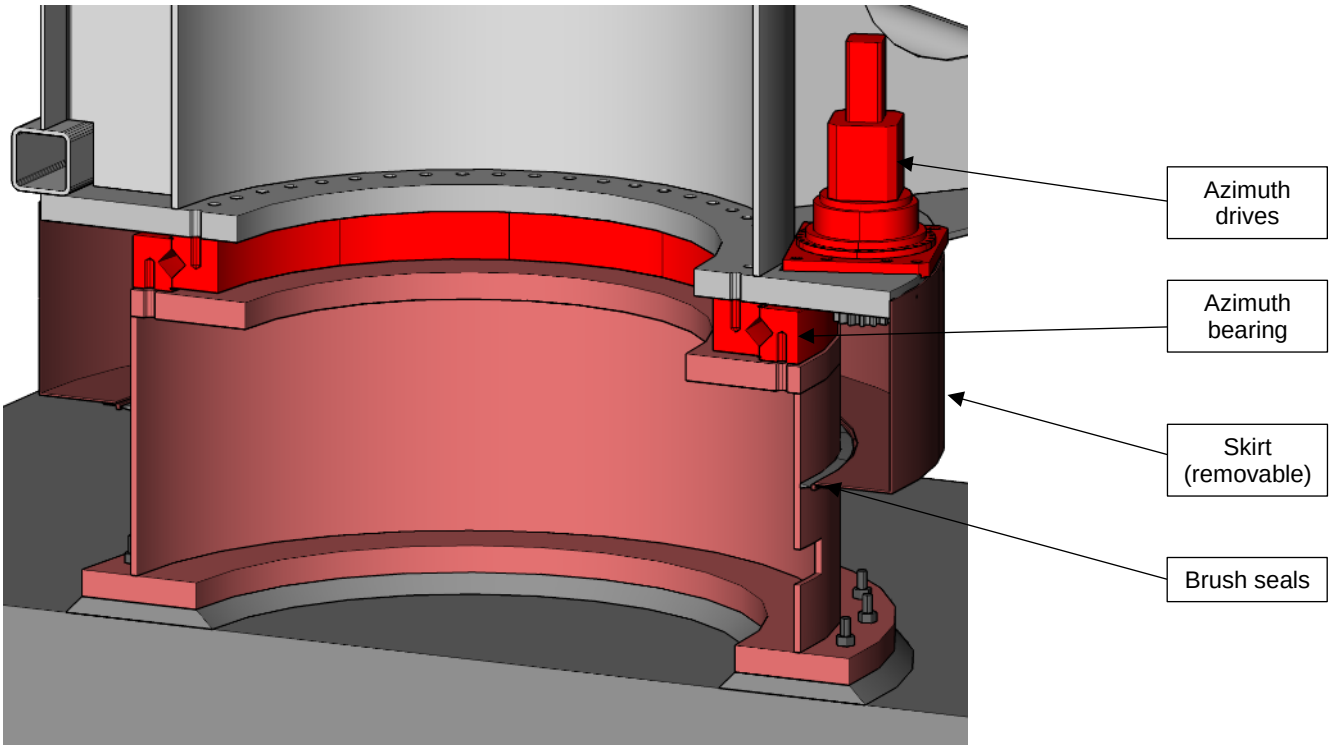

Figure 4-27: Azimuth bearing arrangement

4.3.2 Elevation Bearings

The general arrangement of the elevation bearings is shown in Figure 4-28. The elevation bearings utilize spherical roller bearings to release moments. One of the bearings is fixed axially, and the other is floating axially with axial release provided via a linear rail mount. The linear rail allows a very low friction axial release while restraining rotation of the elevation bearing about its axis. The bearing size is currently set based on the ERA dish stub shaft diameter of 110mm; this size provides a large margin on bearing capacity under operational and survival conditions.

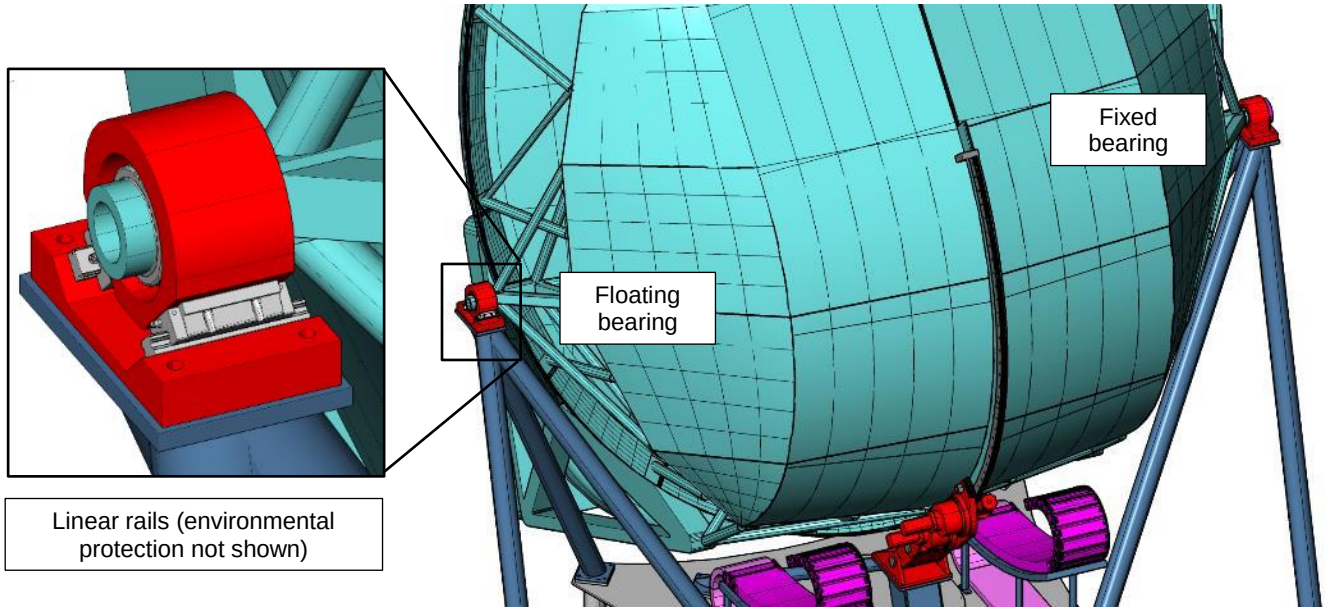

Figure 4-28: Elevation bearing arrangement

24024 CC/W33

Popular item
SKF Explorer

Spherical roller bearings

Bearing data

Tolerances,
Normal, P6, P5, tapered bore 1:12, tapered bore 1:30,
Radial internal clearance,
cylindrical bore, tapered bore

Bearing interfaces

Seat tolerances for standard conditions,
Tolerances and resultant fit

Technical specification

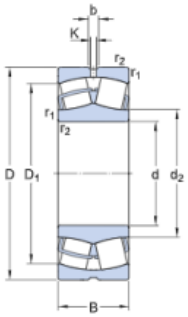

DIMENSIONS

d	120 mm
D	180 mm
B	60 mm
d_2	≈ 132 mm
D_1	≈ 159 mm
b	6 mm
K	3 mm
$r_{1,2}$	min. 2 mm

Figure 4-29: Elevation bearing cut sheet

FLS – Flanged, long, standard height R1653 ... 2.

Dynamic characteristics

Travel speed: v_{max} = 5 m/s

Acceleration: a_{max} = 500 m/s²

(If $F_{comb} > 2.8 \cdot F_{pr}$: a_{max} = 50 m/s²)

Note on lubrication

- Pre-lubricated

Note

Can be used on all SNS/SNO ball guide rails. Ball runner blocks of size 55 and size 65 can be found in chapter "Heavy-duty ball runner block BSHP made of steel" after this chapter.

Options and material numbers

Size	Ball runner blocks with size	Preload class				Accuracy class						Seals on ball runner blocks					
												without ball chain			with ball chain		
		C0	C1	C2	C3	N	H	P	XP	SP	UP	SS	LS[1)]	DS	SS	LS[1)]	DS
15	R1653 1	9				4	3	–	–	–	–	20	21	–	22	23	–
			1			4	3	2	8	1	9	20	21	2Z	22	23	2Y
				2		–	3	2	8	1	9	20	21	2Z	22	23	2Y
					3	–	–	–	8	1	9	20	21	2Z	22	23	2Y
20	R1653 8	9				4	3	–	–	–	–	20	21	–	22	23	–
			1			4	3	2	8	1	9	20	21	2Z	22	23	2Y
				2		–	3	2	8	1	9	20	21	2Z	22	23	2Y
					3	–	–	–	8	1	9	20	21	2Z	22	23	2Y
25	R1653 2	9				4	3	–	–	–	–	20	21	–	22	23	–
			1			4	3	2	8	1	9	20	21	2Z	22	23	2Y
				2		–	3	2	8	1	9	20	21	2Z	22	23	2Y
					3	–	–	–	8	1	9	20	21	2Z	22	23	2Y
30	R1653 7	9				4	3	–	–	–	–	20	21	–	22	23	–
			1			4	3	2	8	1	9	20	21	2Z	22	23	2Y
				2		–	3	2	8	1	9	20	21	2Z	22	23	2Y
					3	–	–	–	8	1	9	20	21	2Z	22	23	2Y
35	R1653 3	9				4	3	–	–	–	–	20	21	–	22	23	–
			1			4	3	2	8	1	9	20	21	2Z	22	23	2Y
				2		–	3	2	8	1	9	20	21	2Z	22	23	2Y
					3	–	–	–	8	1	9	20	21	2Z	22	23	2Y
45	R1653 4	9				4	3	–	–	–	–	20	–	–	22	–	–
			1			4	3	2	8	1	9	20	–	2Z	22	–	2Y
				2		–	3	2	8	1	9	20	–	2Z	22	–	2Y
					3	–	–	–	8	1	9	20	–	2Z	22	–	2Y
E.g.:	R1653 7		1				3					20					

Figure 4-30: Elevation bearing linear guide cut sheet

4.4 Drives

The following were identified as primary candidates for the azimuth and elevation drive mechanisms:

- Option 1: Rack and pinion with servo-based gear motor
- Option 2: Rack and pinion with direct-drive motor
- Option 3: Direct drives

A trade-study of these options is provided in Section 7 below, and recommends that Option 1 and Option 3 are the leading candidate solutions. Option 1 is the lowest cost, however there is an appreciable reduction in mount stiffness, particularly on the azimuth axis. The largest benefit of Option 3 is related to the controllability and settling performance which is outside of the scope of this document. As such, final selection will be made in conjunction with NRC once further analysis and evaluation of controls performance is available.

Option 1 is considered the “baseline” design. This design utilizes a rack and pinion drive where the pinion is driven by a conventional gearbox-servo motor assembly. The pinion drives are provided in pairs such that during observing one pinion is back-driven in order to eliminate backlash. A basic description of the conceptual design is provided below, and further information on component sizing is provided in Section 6.

4.4.1 Azimuth Drives

Figure 4-31 shows the azimuth drive arrangement. The pinions interface with an external gear on the slewing ring. Lubrication for the gears will be provided by means of passive, automatic lubrication units with lubrication pinions as shown in Figure 4-32

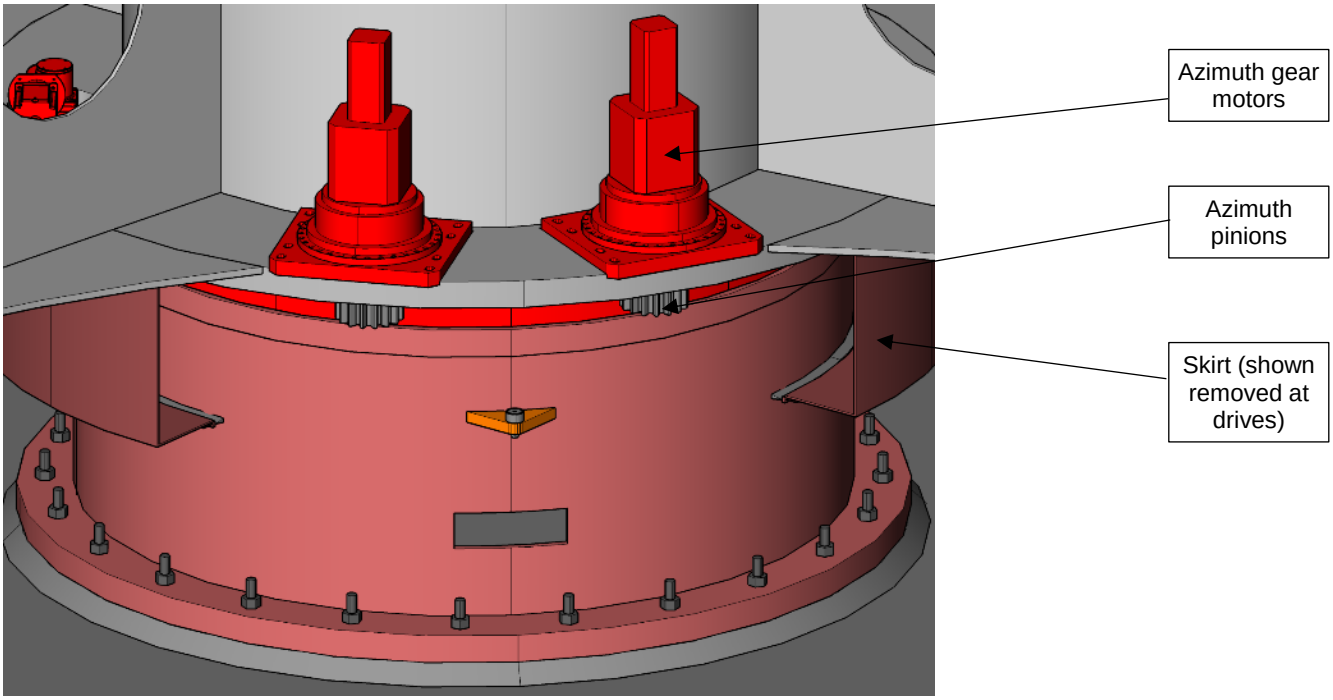

Figure 4-31: Azimuth drives

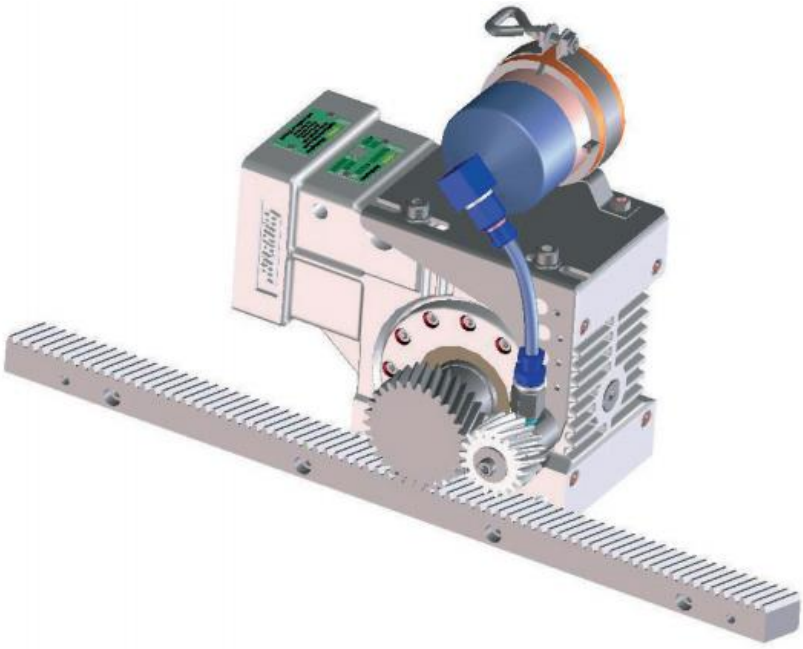

Figure 4-32: Rack lubrication system example

4.4.2 Elevation Drives

Figure 4-33 and Figure 4-34 show the elevation drive concept. The proposed concept utilizes a “tow-link” arrangement where the two pinion drives are mounted to an articulating assembly which is constrained to the rack segments via two cam-followers that guide off of a running surface machined into the rack. This articulating assembly is then connected back to the mount via the tow-link. The tow-link assembly as shown utilizes two cylindrical bearing assemblies, however a flexure-based design will be investigated in future design phases which would eliminate the need for bearings and the associated potential backlash.

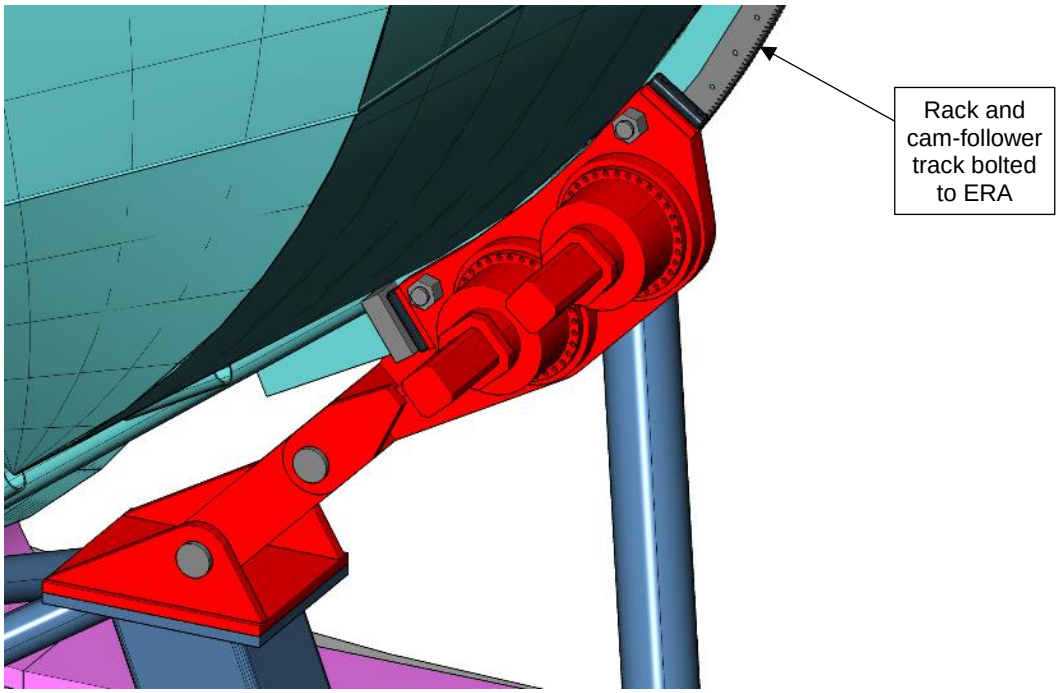

Figure 4-33: Elevation drive integration with ERA

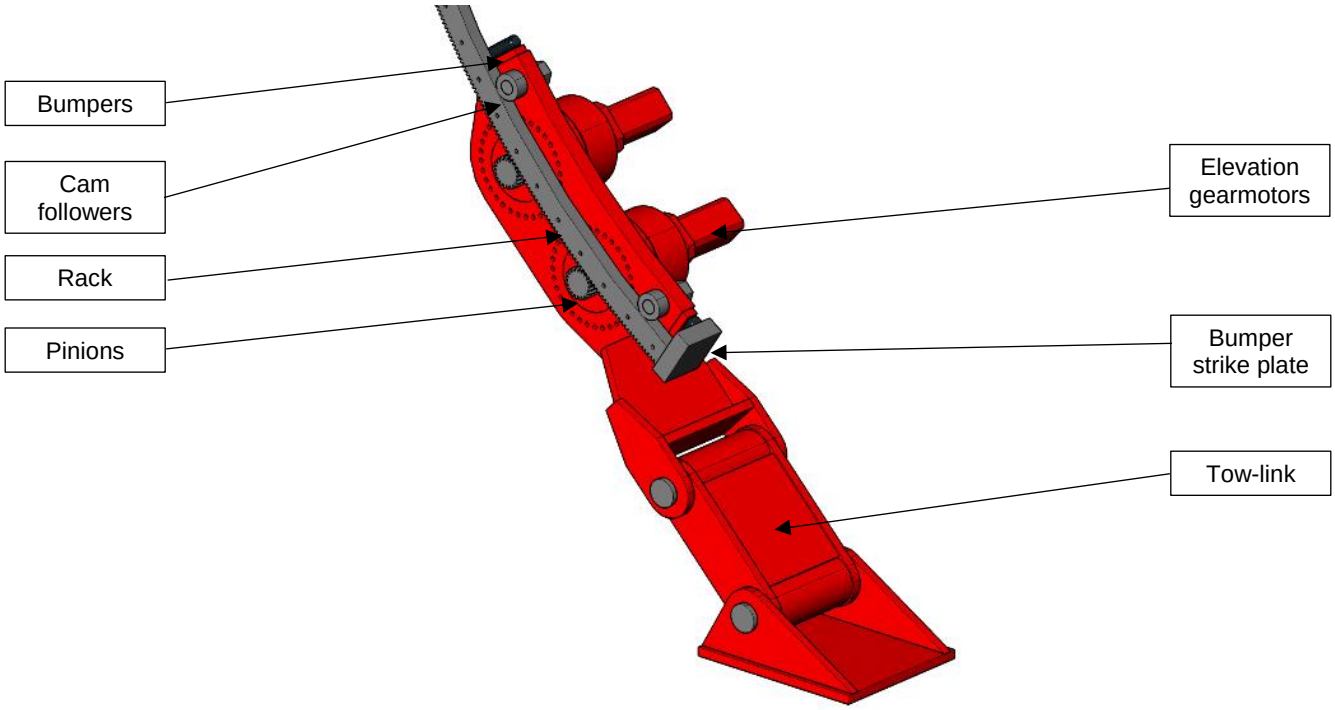

Figure 4-34: Elevation drive assembly

The tow-link approach has two main benefits. Firstly, it ensures that the reaction forces into the ERA from the drive system are purely tangential, as illustrated in the left side of Figure 4-35. The contact geometry between the pinion and gear results in both radial and tangential force components, as illustrated in the right side of Figure 4-35. The radial components are reacted by the cam-followers such that there is no net radial load acting on the ERA. This eliminates deflections in the ERA due to radial loading from the drives. Secondly, the pinion tooth engagement is governed by the tolerances between the rack and the running surface for the cam-followers, which are both contained in a single machined part. This relaxes the overall assembly-level run-out tolerances on the rack and ensures correct tooth engagement. The main drawback of the tow-link approach is the additional complexity. If the above advantages do not warrant the complexity based on additional analysis of the ERA then the gearboxes can be rigidly mounted with adjustment provisions for fine tooth alignment.

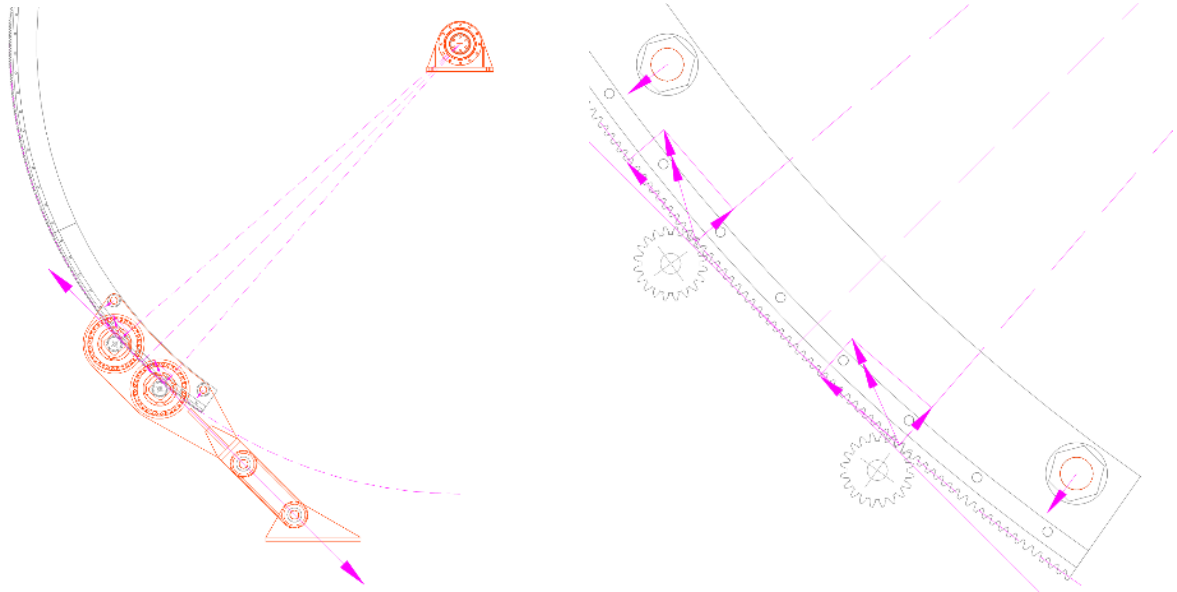

Figure 4-35: Elevation axis tow-link reaction geometry

It is noted that a similar tow-link arrangement is used on the GBT elevation drive. In that case the tow link utilizes two spherical bearings, as opposed to two cylindrical bearings, and as such the articulating assembly requires lateral rollers as well to constrain the drive assembly laterally and in yaw. This has the benefit that it accounts for axial misalignment of the elevation gear, however this additional complexity may not be warranted on the much smaller ngVLA 6m antenna.

4.5 Braking, Travel Stops and Locking Pins

Table 4-1 lists requirements related to travel limits and mechanical safety devices.

Table 4-1: Requirements for travel limits and mechanical safety devices

Parameter	Req.	Description
Hardware limits	SBA1702	The antenna shall be equipped with mechanically-driven switches to inhibit operation outside its safe operating limits

Hard stops	SBA1703	The antenna shall be equipped with hard mechanical stops that physically prevent the antenna from exceeding operating limits when damage is imminent.
Safety lock-out	SBA1704	The antenna shall be equipped with a safety lock-out that inhibits motion of the antenna during service.
Fail safe brakes	SBA1706	The drive brakes shall engage when the antenna experiences a loss of power.

The following outlines the theory of operations and assumptions with regards to braking, travel stops, and locking pins:

- The motor brakes are sized with sufficient capacity hold the full torque of motors; this provides braking torque in excess of “limit operating conditions” requirements
- Limit switches are set to engage at the end of the tracking range to cut drive power and activate motor brakes
- The drive system will utilize safe speed control technology with programmed safe speed limits; it is currently assumed the limit is set at 20% over maximum required slewing speed for the purpose of sizing travel stops
- The travel stops are sized to absorb full kinetic energy at the safe speed limit
- The travel stops are sized to withstand survival level wind torque
- The travel stops will be positioned with 1deg (TBC) over-travel beyond the tracking range
- The locking pins are sized for survival level loads (wind load is governing)

4.5.1 Travel Stops

Due to low peak velocities typical hydraulic dampers are not suitable. The bumper design is governed by peak loads for which elastomeric bumpers are well suited. Commercially available units from ACE controls have been selected based on the azimuth system requirements (more severe than elevation requirements). Final design will include deceleration analysis and optimization.

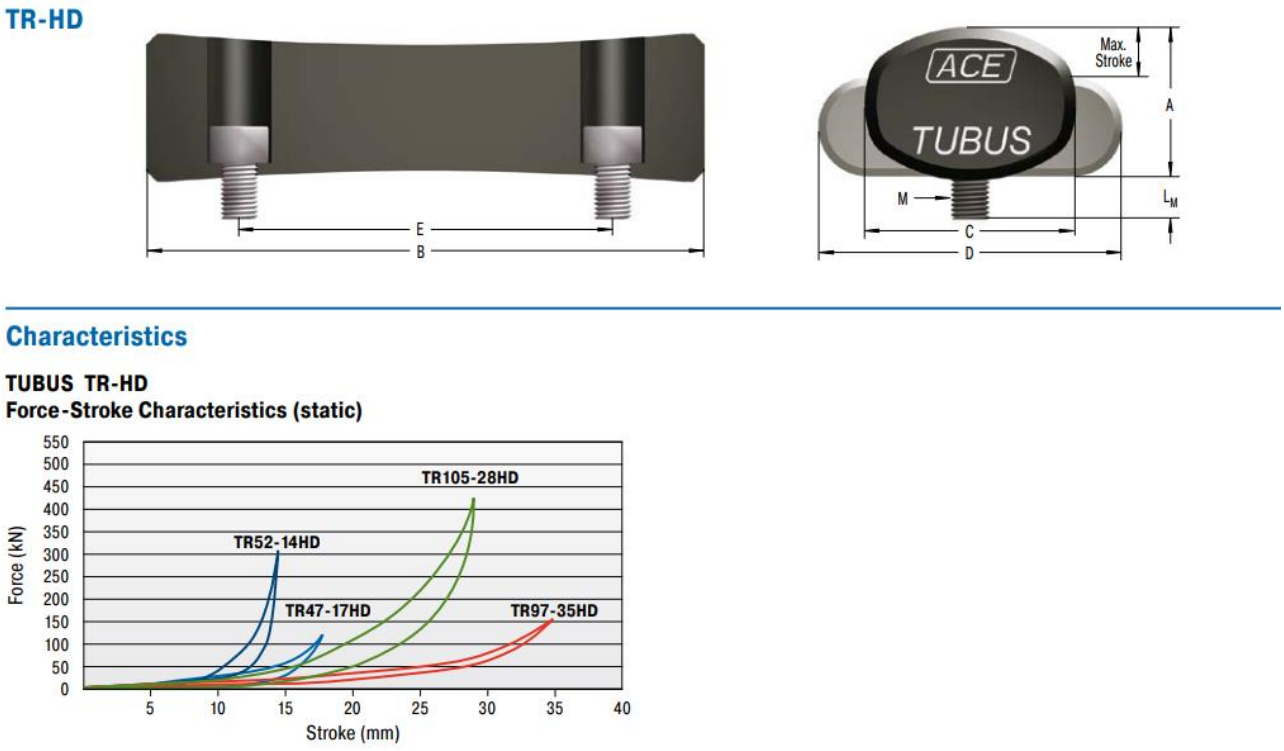

Figure 4-36: Travel stop bumper preliminary selection

The integration of the bumpers into the elevation drive assembly is shown in Figure 4-34 above. For the azimuth axis travel stops a topple block arrangement is required to achieve the +/-270 degree rotation range. This is depicted in Figure 4-37 to Figure 4-39.

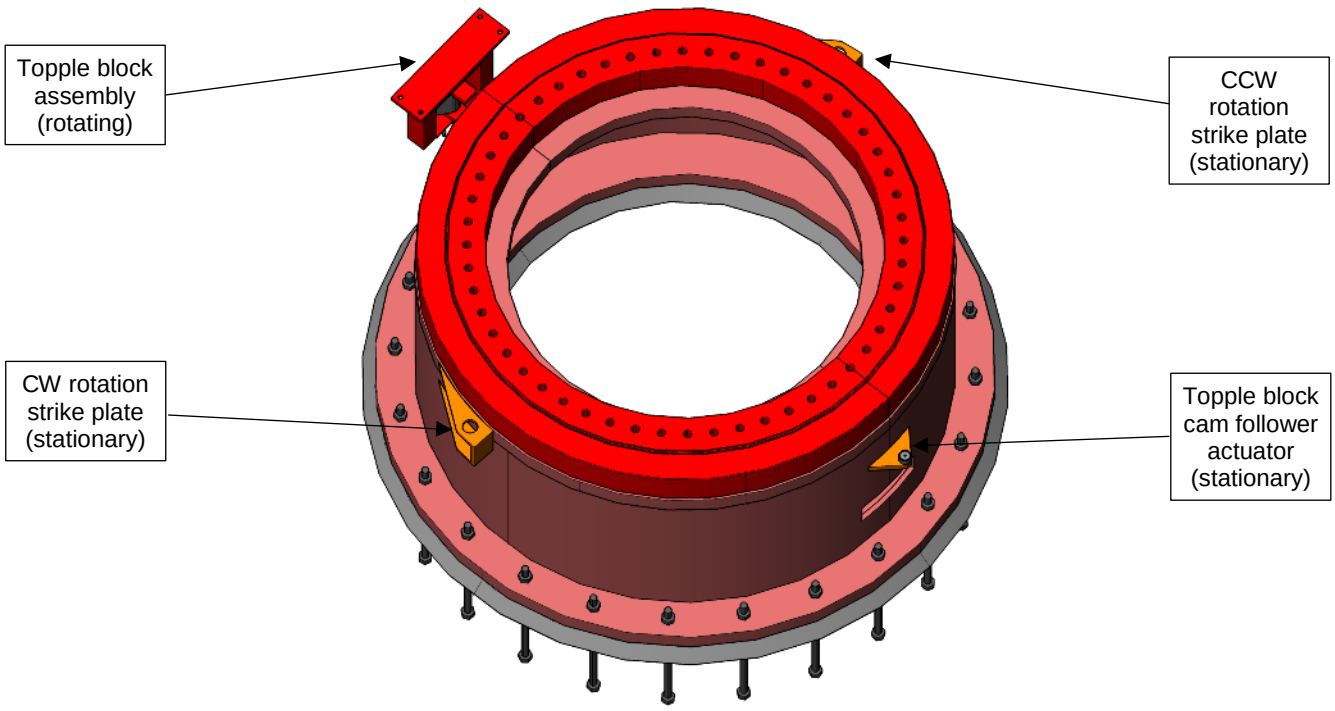

Figure 4-37: Azimuth travel stop arrangement

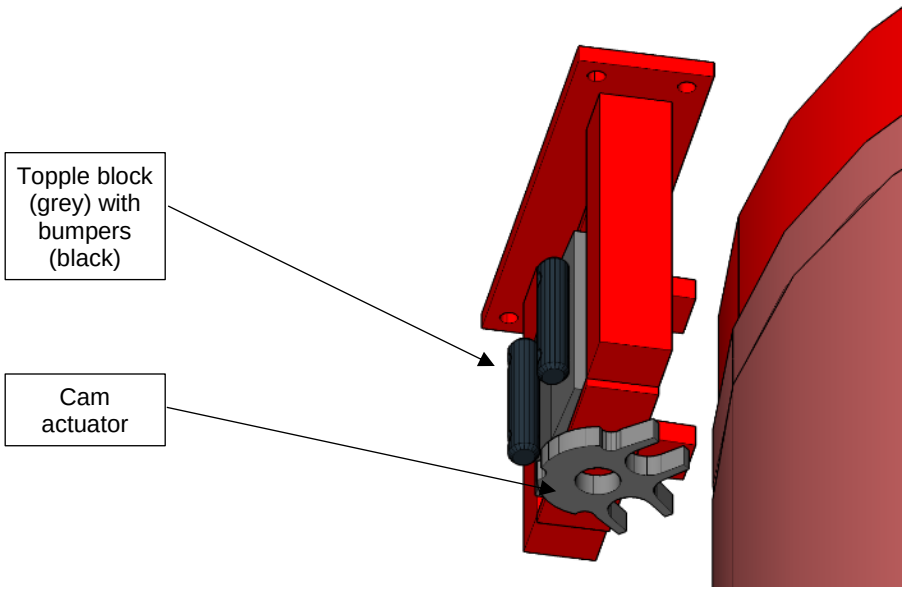

Figure 4-38: Azimuth topple block assembly

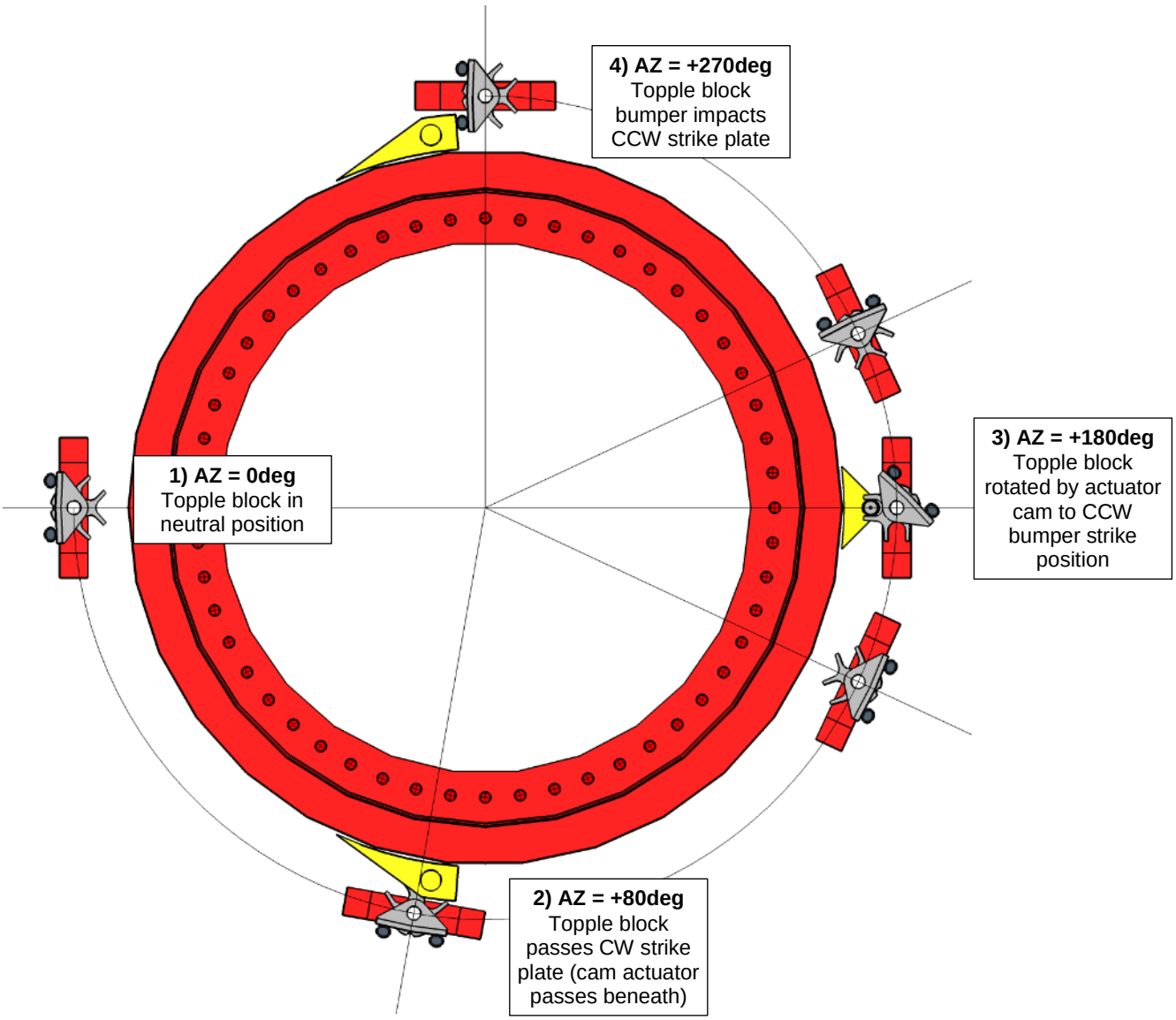

Figure 4-39: Azimuth travel stop functionality for 0deg to +270deg (CCW) travel

4.5.2 Locking Pins

Locking pins are designed for stowing the telescope when not in use and are sized to prevent any rotation during survival conditions. The proposed design uses hardened pins which are driven into a bushing via an integrated machine screw jack. The jacks are conservatively sized to engage or disengage the pin while the pin is loaded against survival level wind. This conservative sizing should prevent the chance of jammed pins. Figure 4-40 shows an exploded view of the azimuth locking pin assembly. The elevation lock is similar.

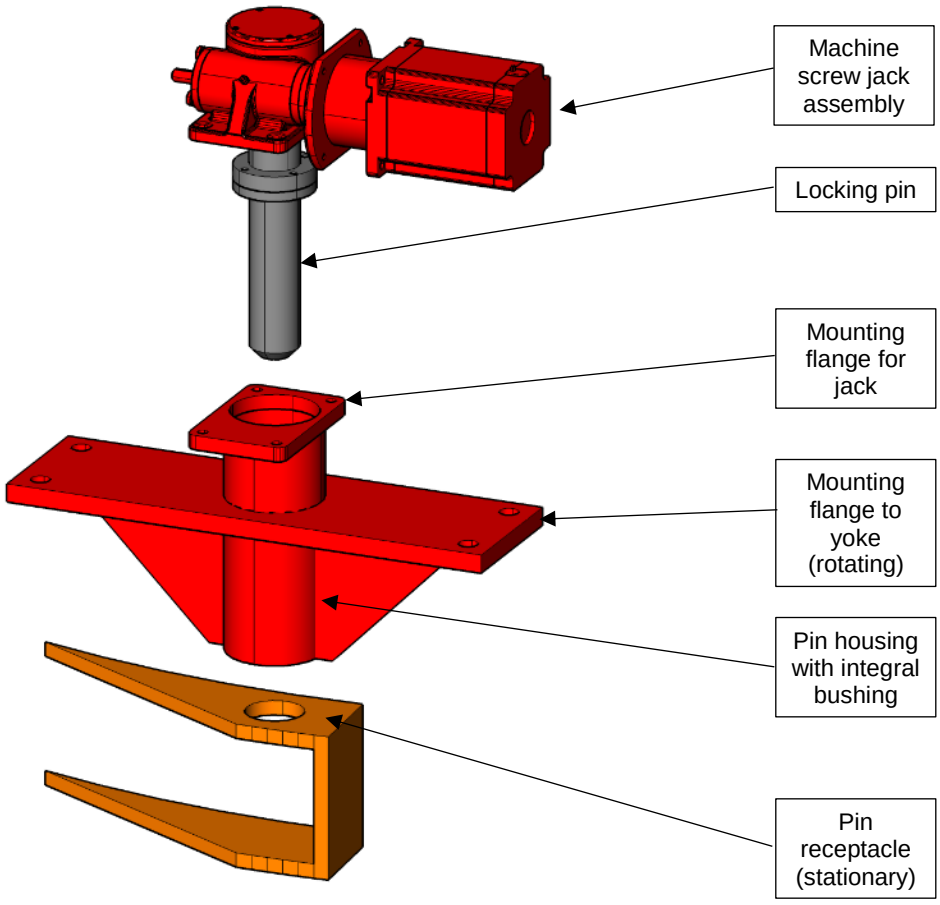

Figure 4-40: Azimuth locking pin assembly, exploded

Figure 4-41 and Figure 4-42 show the azimuth and elevation locking pin integration, respectively. For the elevation locking pin the receptacle is integrated into the drive rack, with receptacles provided at the survival stow position (EL=88deg) and maintenance position (EL=16deg).

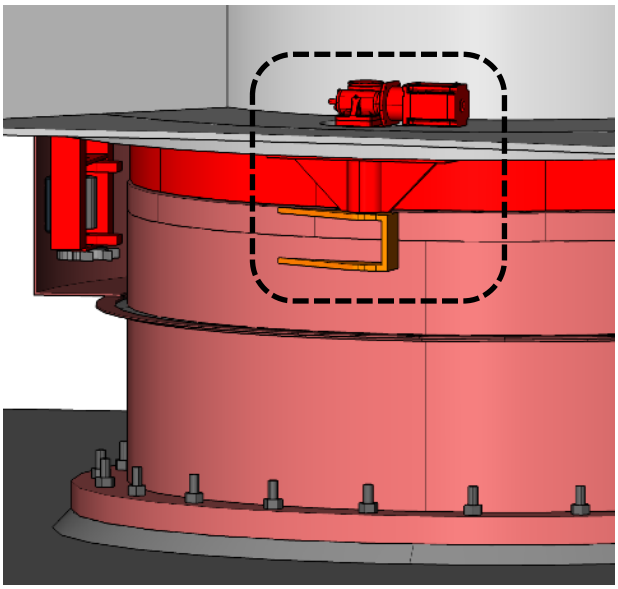

Figure 4-41: Azimuth locking pin integration

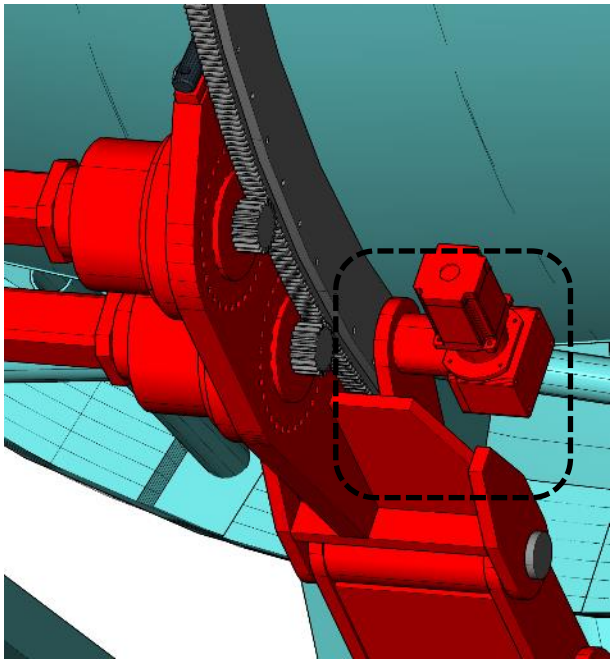

Figure 4-42: Elevation locking pin integration

4.6 Utilities Distribution

Figure 4-43 shows the preliminary cabling plan provided by NRAO.

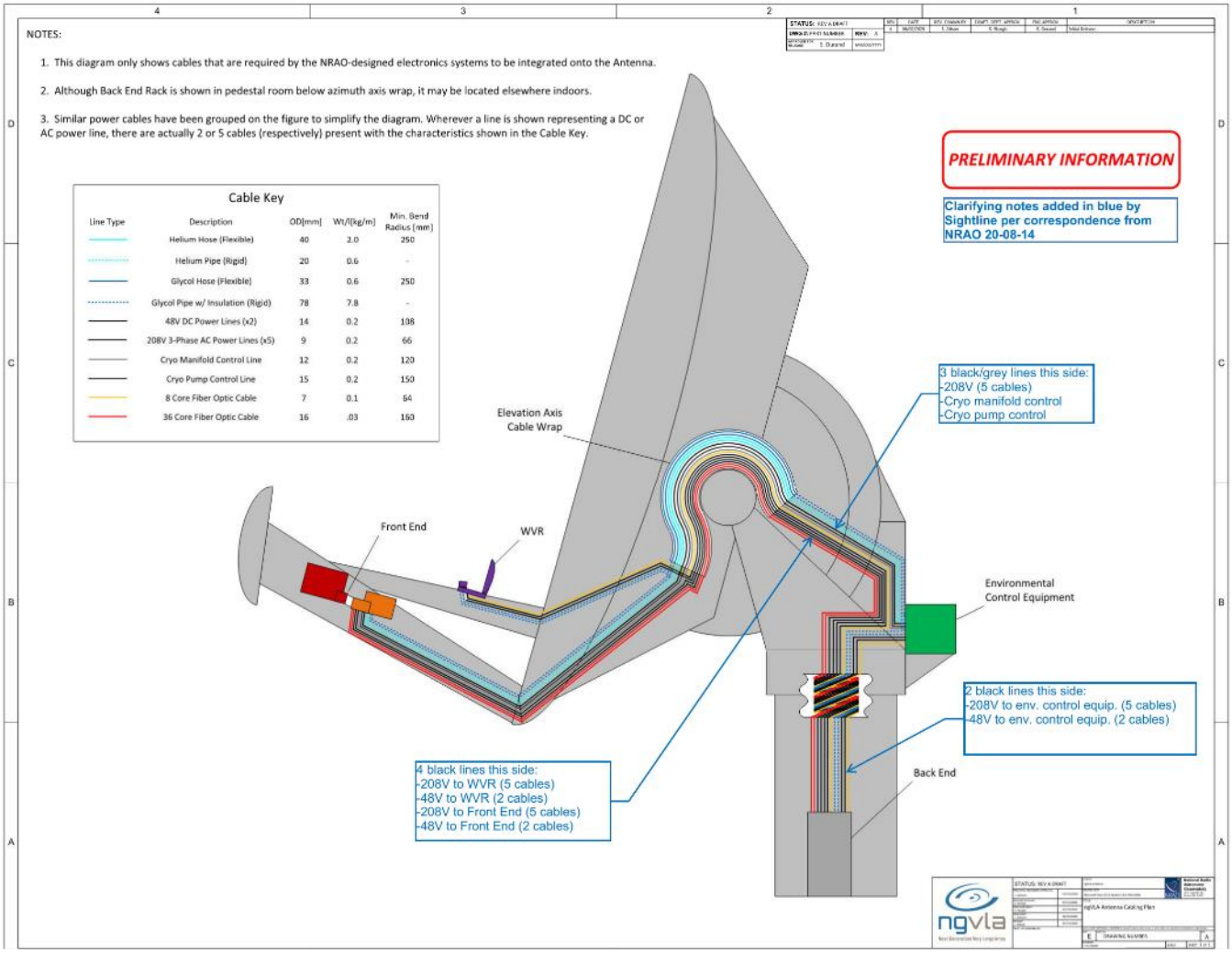

Figure 4-43: NRAO cabling plan

The information above was used to estimate the required width of the utility wraps for the azimuth and elevation axes shown in Table 4-2. Cable spacing requirements are based on 1.25 times the cable diameter, and 50% spare allocation is included. Based on this estimation, the selected cable wrap sizes for conceptual design are as follows:

- Azimuth: 1 x 600mm wide wrap, 150mm bend radius
- Elevation: 2 x 400mm wide wraps, 250mm bend radius

Note that the 150mm bend radius on the azimuth wrap is slightly smaller than the 160mm required for the 36-core fibre optic cable, however the bending radius is specified at the wrap centreline and can be increased slightly if cables are pushed to the outside of the wraps. 150mm is a standard bend radius from IGUS.

Table 4-2: Utility wrap space requirements

CABLE DATA					**AZ WRAP**				**EL WRAP**			
	OD [mm]	Min Bend Rad [mm]	Wt [kg/m]	Est Source	Qty [ ]	Wt [kg/m]	Spacing [mm]	Space Reqm't [mm]	Qty [ ]	Wt [kg/m]	Spacing [mm]	Space Reqm't [mm]
Helium hose (flexible)	40	250	2.0	NRAO	-	-	-	-	2	4.0	50	100
Glycol hose (flexible)	33	250	0.6	NRAO	-	-	-	-	2	1.2	41	83
48V DC Power Lines (x 2) - Front End	14	108	0.2	NRAO	2	0.4	18	35	2	0.4	18	35
48V DC Power Lines (x 2) - WVR	14	108	0.2	NRAO	2	0.4	18	35	2	0.4	18	35
48V DC Power Lines (x 2) - Env. Control Equip.	14	108	0.2	NRAO	2	0.4	18	35	-	-	-	-
208V 3-Phase AC Power Lines (x 5) - Front End	9	66	0.2	NRAO	5	1.0	11	56	5	1.0	11	56
208V 3-Phase AC Power Lines (x 5) - WVR	9	66	0.2	NRAO	5	1.0	11	56	5	1.0	11	56
208V 3-Phase AC Power Lines (x 5) - Env. Control Equip.	9	66	0.2	NRAO	-	-	-	-	5	1.0	11	56
208V 3-Phase AC Power Lines (x 5) - Cryo	9	66	0.2	NRAO	5	1.0	11	56	-	-	-	-
208V 3-Phase AC Power Lines (x 5) - Mount Drives	9	66	0.2	Sightline	5	1.0	11	56	-	-	-	-
Cryo Manifold Control Line	12	120	0.2	NRAO	-	-	-	-	1	0.2	15	15
Cryo Pump Contol Line	15	150	0.2	NRAO	-	-	-	-	1	0.2	19	19
8 Core Fiber Optic Cable	7	64	0.1	NRAO	2	0.2	9	18	1	0.1	9	9
36 Core Fiber Optic Cable	16	160	0.03	NRAO	2	0.1	20	40	2	0.1	20	40
Subtotal				Sightline		**5.5**		**388**		**9.6**		**504**
Margin / Spare Allocation				Sightline			50%	194			50%	252
TOTAL ESTIMATED				Sightline				**581**				**756**
TOTAL PROVIDED				Sightline				**600**				**800**

Figure 4-44 shows an overview of the mount utility distribution system. The dark purple represents flexible utility chain, and the light purple represents rigid utility distribution tray.

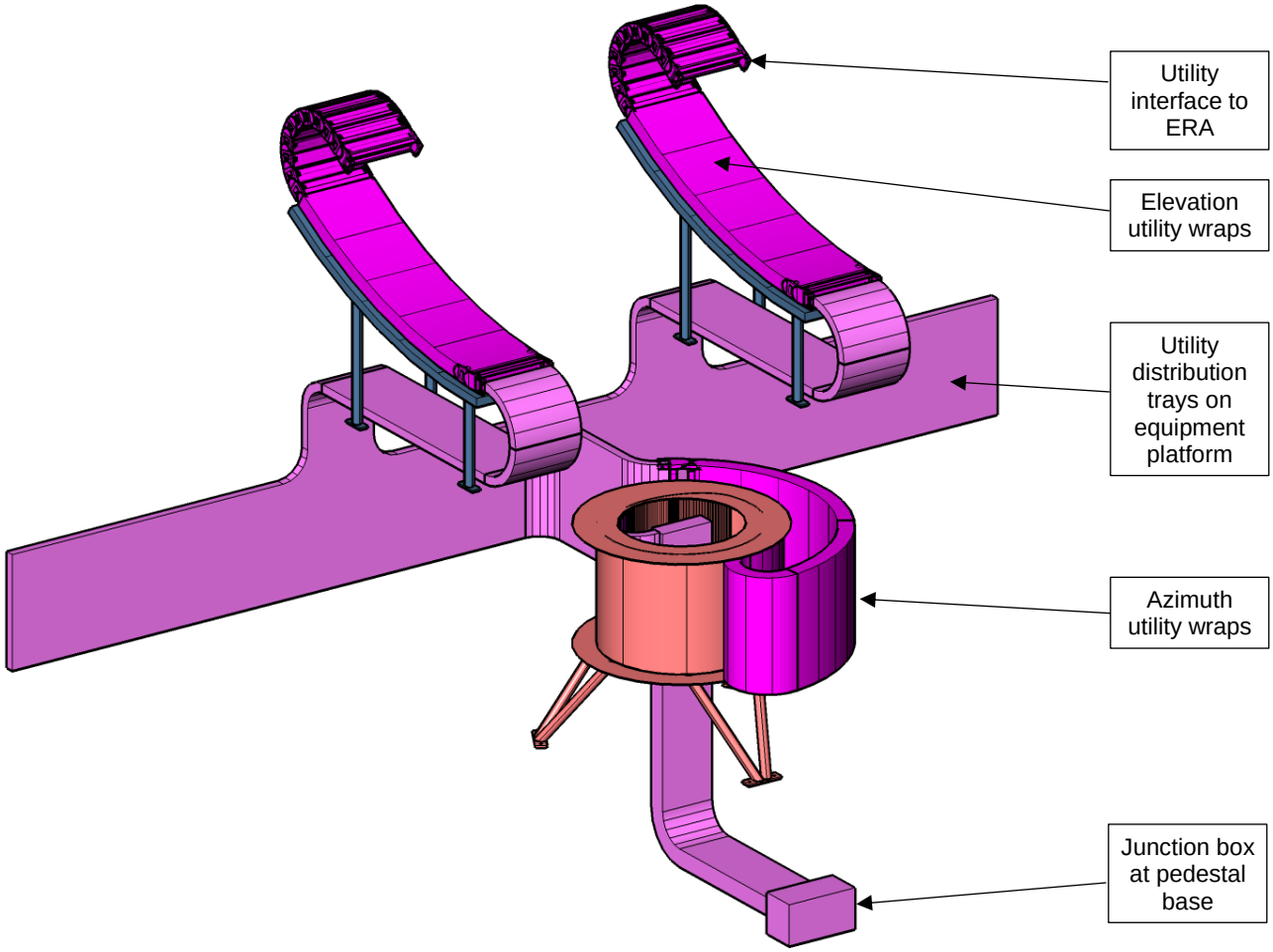

Figure 4-44: Utility distribution overview

Figure 4-45 and Figure 4-46 show the azimuth utility wrap assembly.

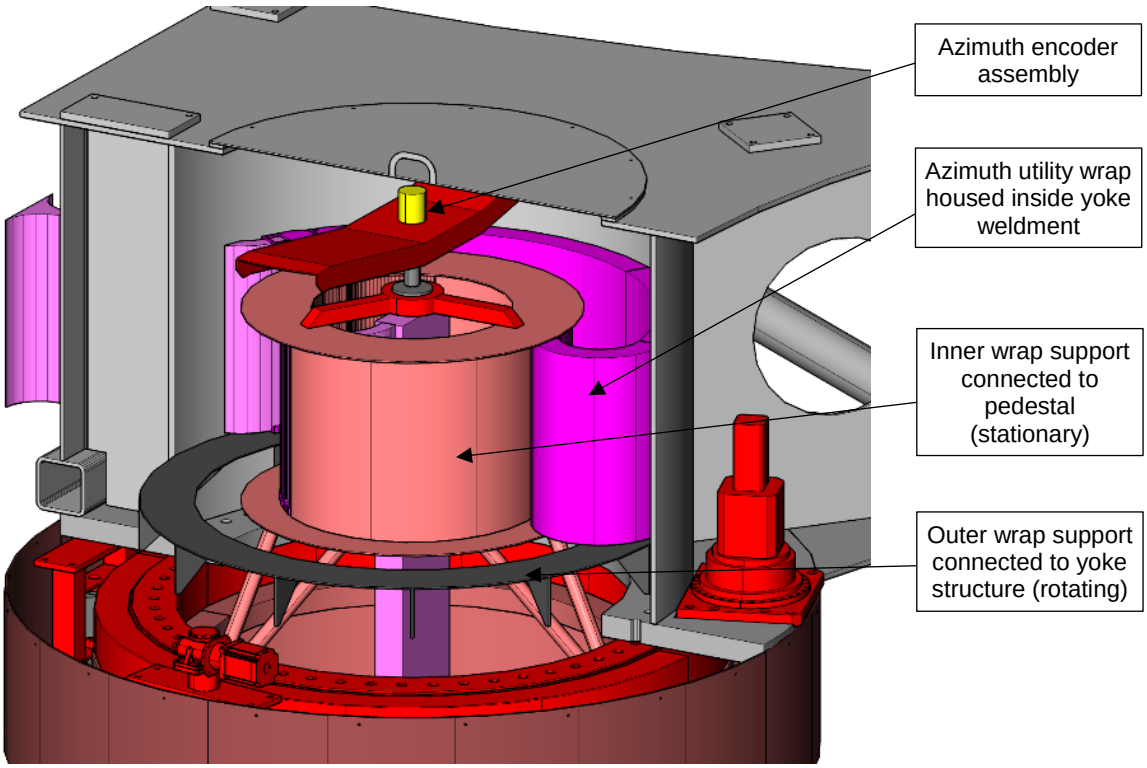

Figure 4-45: Azimuth utility wrap

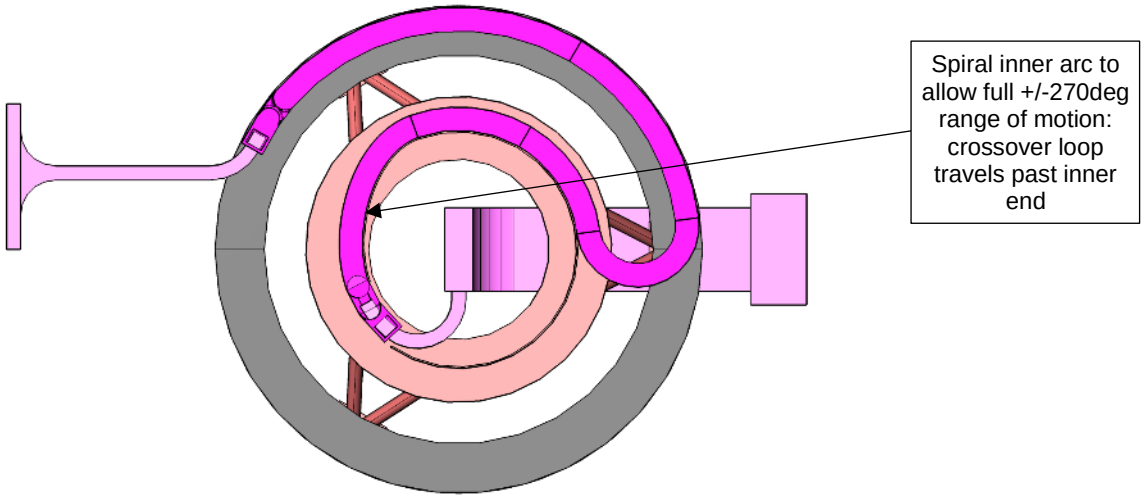

Figure 4-46: Azimuth utility wrap, plan view

Figure 4-47 shows the elevation utility wrap assembly.

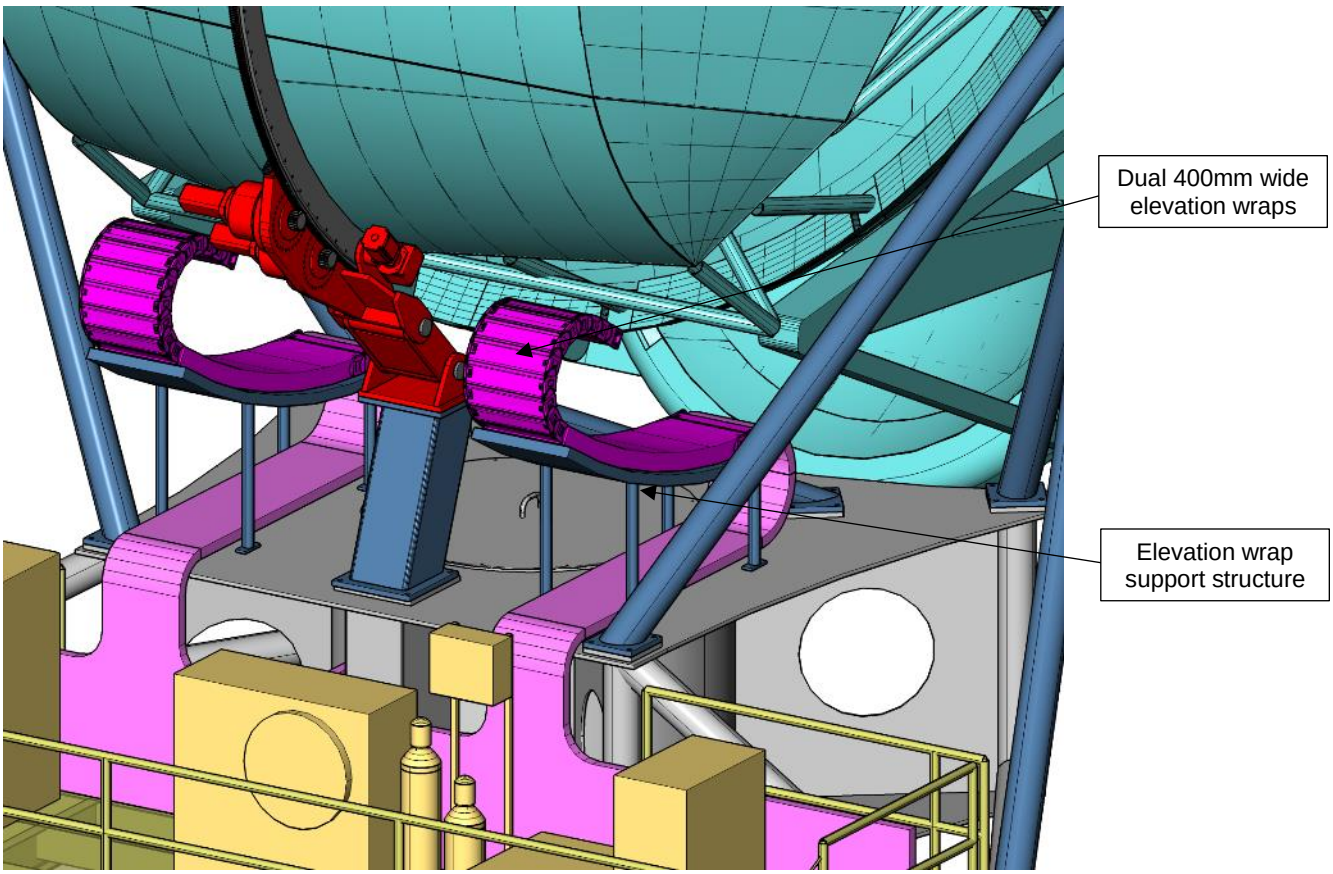

Figure 4-47: Elevation utility wraps

The preliminary cable chain selection utilizes commercially available products from IGUS. The IGUS E-chain series has a large selection of options for cable management and strain relief, and the utility cavity is accessible from both the inside and outside of the wrap. The following are features of the preliminary product selection. IGUS information is provided in Figure 4-48.

- Azimuth wrap:
  - IGUS E-Chain E4
  - 54mm inner height and 600mm inner width
  - 150mm standard bend radius at centreline
- Elevation wraps:
  - IGUS E-chain R188840
  - 56mm inner height and 400mm inner width
  - 250mm standard bend radius at centreline
  - Fully enclosed for protection against dirt (note RD01 indicates the wrap may need to be thermally insulated/regulated)

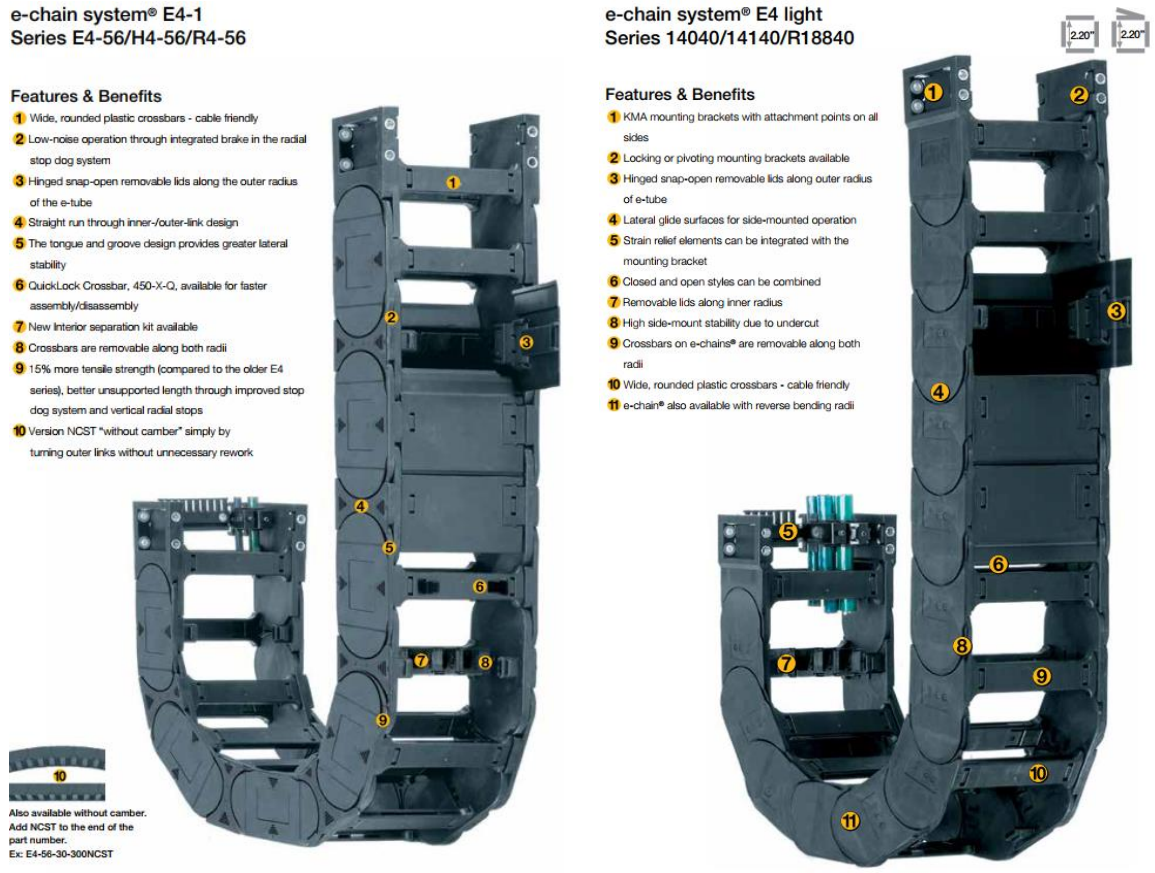

Figure 4-48: IGUS E-chain preliminary selection for azimuth (left) and elevation (right) wraps

4.7 Encoders

On-axis absolute encoders are proposed for both azimuth and elevation axes. The preliminary selection proposes Heidenhain RCN 8000 encoders shown in Figure 4-49. These encoders are self-supporting and have the following performance specifications:

- Resolution: 536870912 steps/revolution (414 steps/arcsec)
- Accuracy: +/-1arcsec

Final selection will require input from control system analysis.

Figure 4-49: Heidenhain RCN 8000 encoder

Figure 4-50 shows the integration of the encoder into the axes.

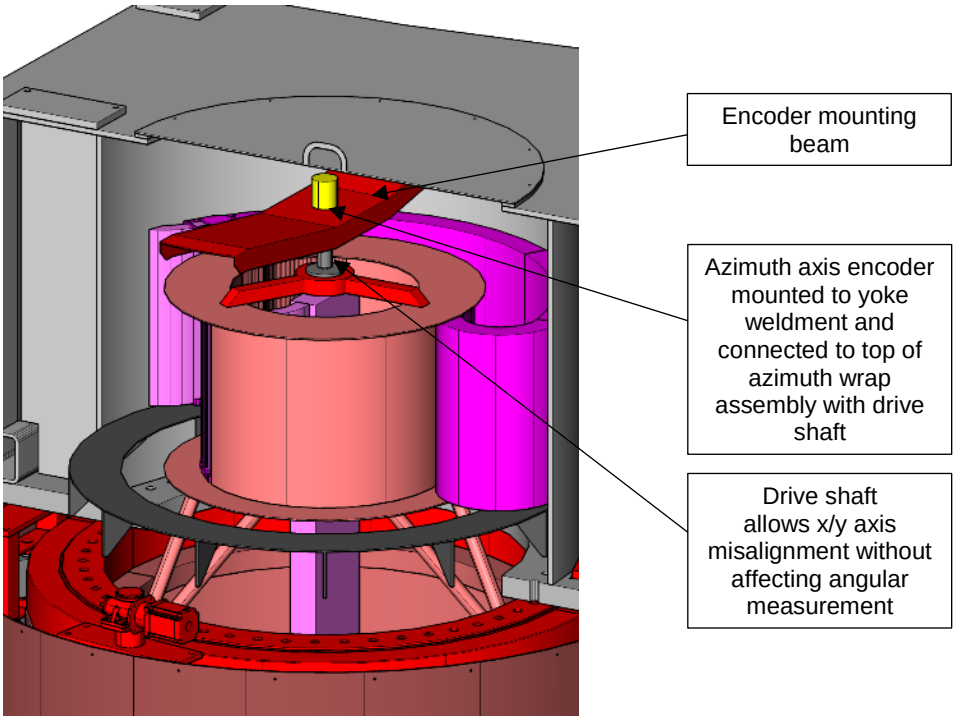

Figure 4-50: Azimuth encoder integration

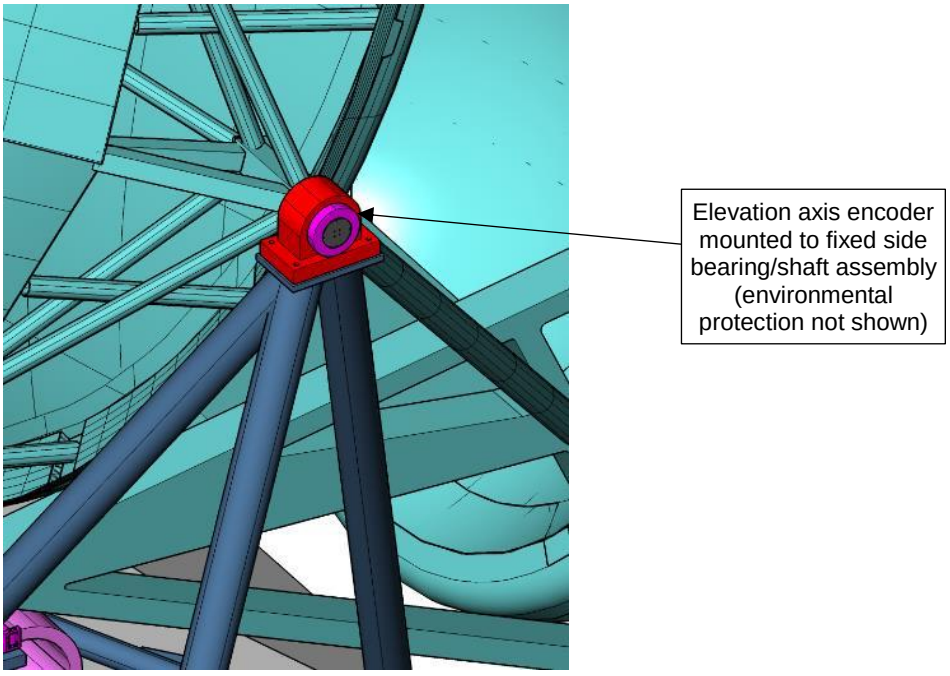

Figure 4-51: Elevation axis encoder integration

4.8 Equipment Platform

Figure 4-52 shows the equipment platform. Preliminary size is 6.5m x 2.0m. NRAO-supplied equipment is shown on the right side of the platform. NRAO access envelopes are shown with partial transparency based on NRAO-supplied interface data.

Mount-supplied electrical cabinets are shown on the left side of the platform, size is notational only and TBD.

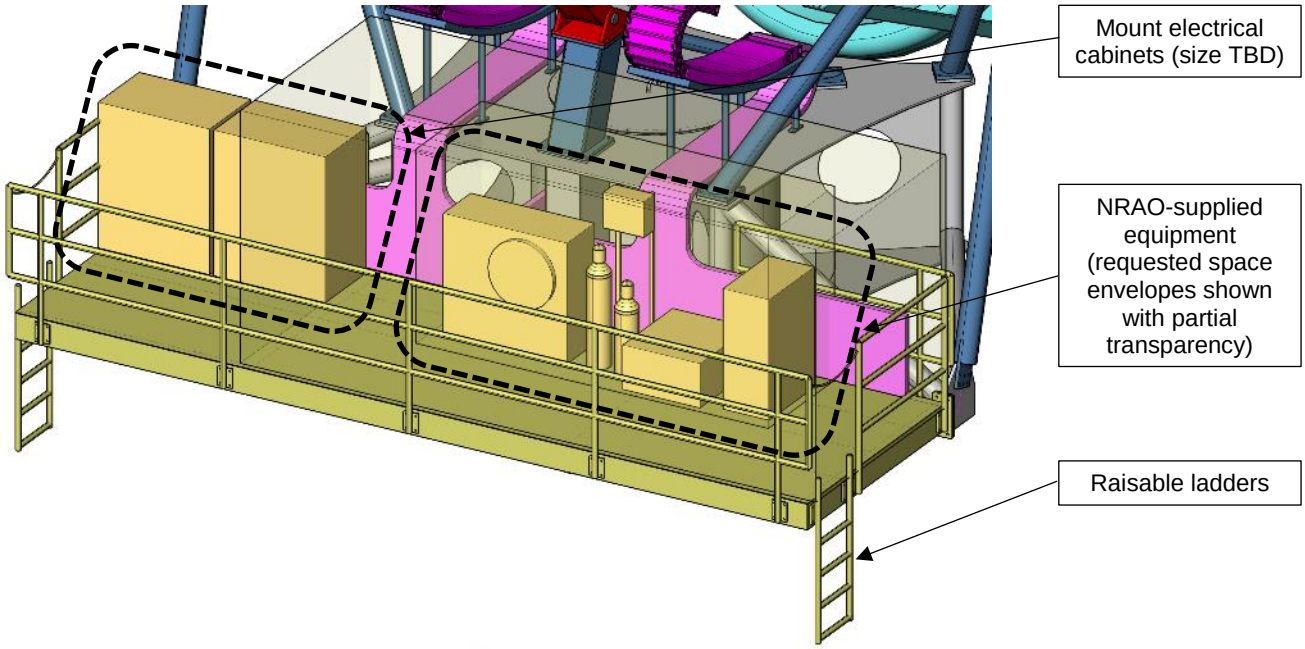

Figure 4-52: Equipment platform

4.9 Mass Estimate

Table 4-3 shows the mass estimate for the mount, which is currently estimated at just over 20 tonnes. The mass estimate for the main components is based on the CAD weight plus 20% allowance for structural detail not modelled such as fasteners, welds, paint, stiffeners. No additional contingency is included in the estimate below.

Table 4-3: Mass Estimate

Description	Mass [kg]	Location FIXED	Location AZ	Location EL	Notes
Structure					
Pedestal	3821	3821			Includes AZ wrap support
Yoke - main weldment	8185		8185		Includes skirts, hatches
Yoke - tripods	1717		1717		Includes EL bearing and EL drive tripods
Equipment platform	1666		1666		Frame, deck, guardrails, ladders
	15390				
Mechanical					
Azimuth bearing	1620	810	810		
Elevation bearings	150		150		Bearing, housing
Azimuth drives	575		575		Gearmotor, pinion, mounting plate
Elevation drive ass'y	682		682		Gearmotor, pinion, mounting frame, tow-link
Elevation gear rack	204			204	Gear sector, mounting sector, end plates
Misc: locking pins, bumpers, encoders	300		300		Allowance
	3531				
Electrical & Payloads					
NRAO-supplied equipment	599		599		Per NRAO drawing 020.30.03.10.00-0001-DWG-Env. Vol. Mass & Loc. Reqs-A
Mount electrical cabinets	400		400		Allowance
Cable wraps, cable tray, wiring	500		500		Allowance (~25m x (10kg/m tray/wrap + 10kg/m cable/hosing))
	1499				
TOTAL - Mount	**20420**				Estimate without margin
TOTAL - ERA	**3302**			3302	Per DRAO, Feb 4, 2020
TOTAL - Telescope	**23722**	**4632**	**15584**	**3506**	

5 STRUCTURAL ANALYSIS

The FEA results presented below are based on a mount FEM with the ERA modelled as a rigid body and lumped mass. The analysis results below including the following:

- Modal properties of the mount (without ERA flexibility contribution)
- Pointing error contribution of the mount (without ERA flexibility contribution)
- Stress analysis of mount under survival conditions

The mount FEM presented herein is ultimately integrated with the ERA FEM by NRC in order to carry out complete performance analyses of the antenna system.

5.1 FEM Description

The stand-alone mount FEM is shown in Figure 5-1. In this model the ERA is modelled as a rigid "dummy" structure (shown in cyan) with a lumped mass/inertia element located at the ERA center of gravity.

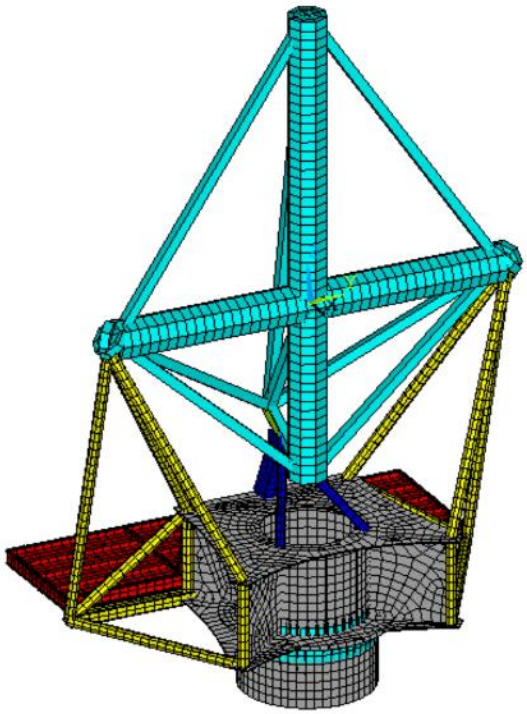

Figure 5-1: Stand-alone mount FEM

The model consists of the following elements types:

- SHELL181: Shell elements, used predominantly to model the yoke and pedestal weldments
- BEAM188: Beam elements
- LINK180: Link (spar) elements
- COMBIN14: Spring elements, linear and rotational
- MASS21: Lumped mass and inertia elements

5.1.1 Boundary Conditions

The ERA is kinematically connected to the mount via the elevation axis (y-axis) as follows:

- 3-DOF are restrained (x,y,z) at the left elevation bearing
- 2-DOF are restrained (x,z) at the right elevation bearing
- 1-DOF is restrained (tangential to elevation axis) at the elevation drive connection
- All restraints are set to be very stiff

The azimuth bearing and drives are modelled via 6 x 1-DOF spring elements at the centre of the azimuth bearing. The spring elements connect back to the pedestal and yoke structures via rigid beams. The 6-DOF spring stiffnesses are set as follows:

- 3-DOF translational springs are set to be very stiff (k=1e+12 N/m) since the radial and axial deflection of the bearing is expected to be negligible
- 2-DOF tilting stiffnesses are set to the specification provided to SKF and Rotek (k=6e+9 N-m/rad)
- 1-DOF rotational stiffness is set very stiff (k=1e+12 N-m/rad) to model locked-rotor frequency

The base of the pedestal is rigidly restrained. Footing and foundation stiffness is not included in the FEM. An estimate of footing and foundation stiffness and contribution to pointing error is provided in Section 5.6 below.

5.1.2 Mass Properties

The ERA is modelled with the following mass properties (per NRC correspondence Feb 4, 2021):

- Mass = 3300kg
- Inertia, x-axis = 3300kg x $(1.05m)^2$ = 3600 kg-m^2
- Inertia, y-axis = 3300kg x $(2.22m)^2$ = 16000 kg-m^2
- Inertia, z-axis =3300kg x $(1.96m)^2$ = 13000 kg-m^2

The equipment platform payload is modelled with a series of lumped masses totalling 1000kg. This includes 599kg for NRAO-supplied equipment (per NRAO drawing 020.30.03.10.00-0001-DWG-Env. Vol. Mass & Loc. Reqs-A) and 400kg allowance for mount electrical cabinets.

The total FEM mass breakdown is as follows:

Mount - FE structural mass	11526 kg
Mount - FE non-structural mass	7492 kg (taken as 65% of structural mass)
Payload - equipment platform	1000 kg
Subtotal - Mount	**20018 kg**
Payload - ERA	3300 kg
TOTAL	**23318kg**

The non-structural mass listed above accounts for items such as mechanical elements, utilities, and structural details not modelled in the FEA. The 65% value is selected such that the total mount mass is nominally 20 tonnes, based on the mass estimate provided in Table 4-3 above. The non-structural mass is applied by increasing the density of steel for the structural elements by a factor of 1.65.

5.2 Modal Analysis

Figure 5-2 below shows the mode shapes of the antenna with a rigid ERA:

- Mode 1, 7.5Hz: Lateral sway
- Mode 2, 10.3Hz: Nodding, equipment platform in-phase
- Mode 3, 11.4Hz: Nodding, equipment platform out-of-phase
- Mode 4-6: Local equipment platform modes (not plotted below)
- Mode 7, 20.2Hz: Yaw (note in the plot below there is significant amplification at the tripod struts that makes the yaw motion of the ERA difficult to see, however the modal participation factors confirm this is the first dominant yaw mode)

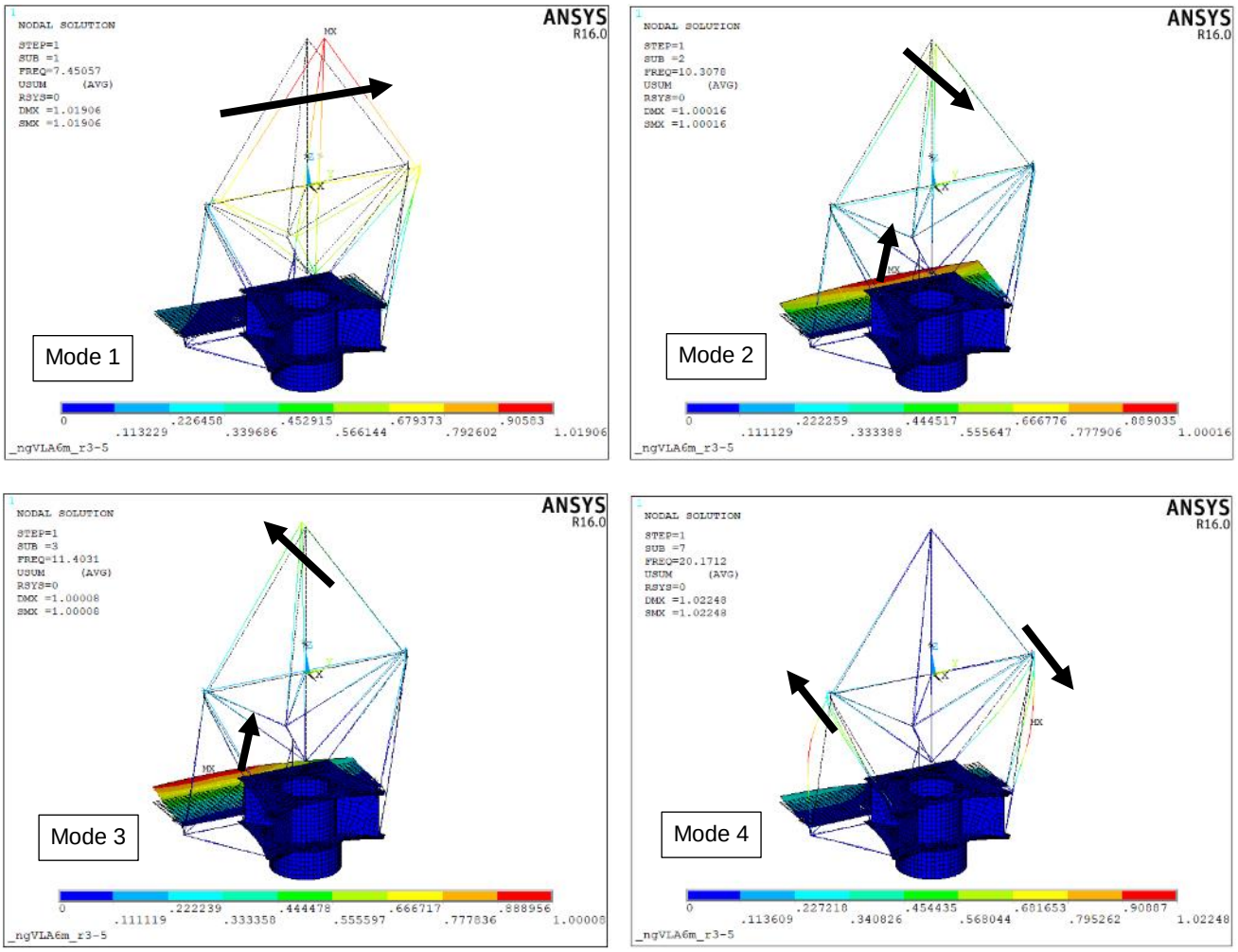

Figure 5-2: Mode shapes

Figure 5-3 shows the effect of azimuth bearing tilting stiffness on the natural frequency. It can be seen that increasing the tilting stiffness beyond the current specified value only results in a minor increase in frequency, so there are limited returns for using a stiffer bearing.

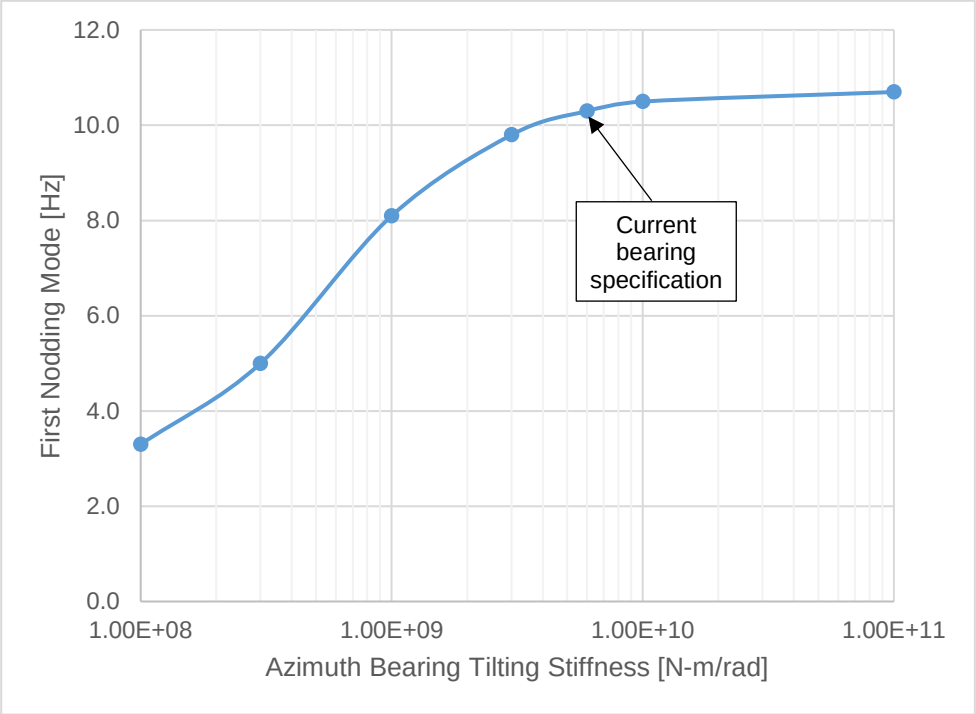

Figure 5-3: Frequency vs azimuth bearing tilting stiffness

The effect of drive stiffness on frequency is documented below in the discussion of drive options.

5.3 Wind Loads

Wind load coefficients on the ERA were taken from NRC-supplied spreadsheet 101-0000-000-MOD-001 Wind Loads Model (RD02). This file was developed based on NRC Offset Reflector wind tunnel test data, and previously used by NRC in the development of the ngVLA 18m antenna, and has been adapted to the ngVLA 6m antenna. Wind load coefficients are used in subsequent estimates of mount pointing error and survival stress analysis.

Figure 5-4 shows the coordinate systems used for the wind data. Figure 5-5 shows 6-DOF wind coefficients as a function of wind azimuth angle and antenna elevation angle. It can be seen in Figure 5-5 that the largest wind loads are fore-aft wind loads (CFP) when the dish is at low elevation angles, and the wind is coming from a frontal direction.

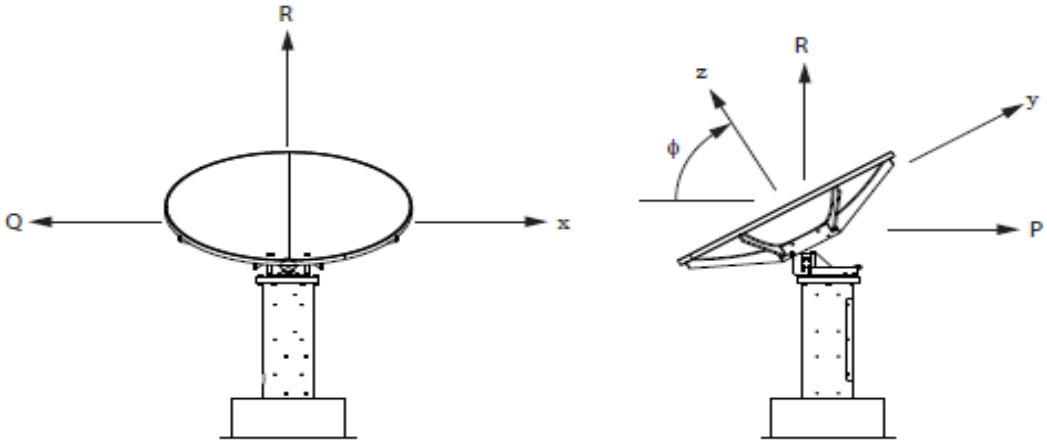

Figure 5-4: Wind load coordinate system

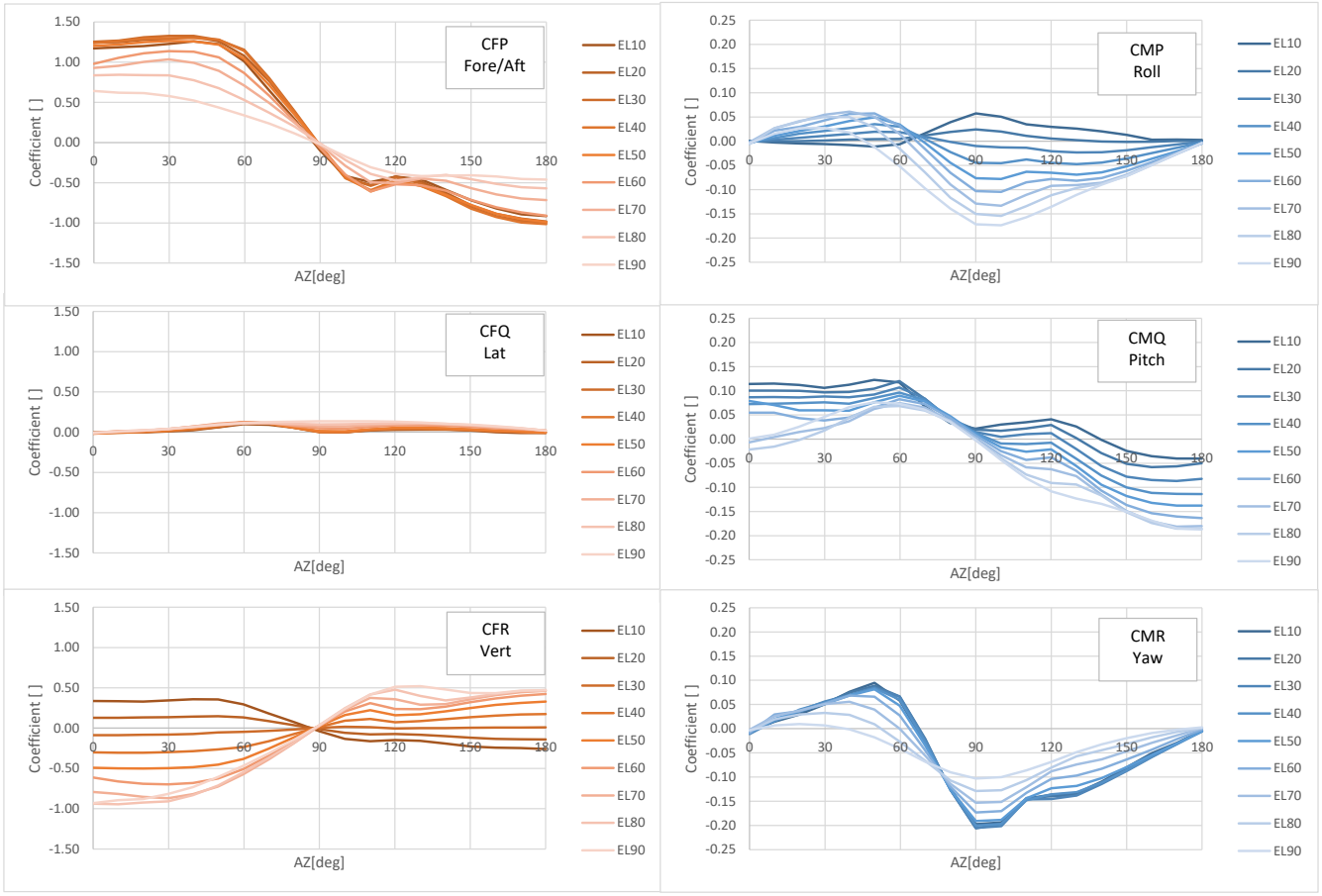

Figure 5-5: Wind coefficients as a function of wind azimuth angle and antenna elevation angle

5.4 Pointing Analysis

This section describes an initial rough-order-of-magnitude estimate of the mount contribution to pointing error due to wind loads on the ERA and temperature gradients within the mount.

Table 5-1 summarizes the pointing accuracy requirements provided by NRAO. Note that these have been reduced from the original requirements RD01 based on direction from NRAO. It is expected that the “normal” condition will govern since the ratio of wind pressure to referenced pointing accuracy is slightly higher for the “normal” condition compared to the “precision” condition. Furthermore, the “normal” condition occurs in combination with daytime solar heating.

Table 5-1: Pointing accuracy requirements

Parameter	Precision Operating Conditions	Normal Operating Conditions
Pointing accuracy, absolute	36 arcsec	70 arcsec
Pointing accuracy, referenced (4deg angle, 15-minute time)	6 arcsec	10 arcsec
Wind, steady (10-minute average)	7m/s	10m/s
Wind, gust	10m/s	15m/s
Temperature range	-15C to +25C (night only)	-15C to +35C

For an initial estimate of wind-induced pointing error, 10m/s wind forces were applied to the FEM and the resulting rotation of the ERA was measured. This was carried out for 6 wind load cases corresponding to the maximum wind forces in the FX, FY, FZ, MX, MY and MZ directions. The results are shown in Table 5-2 below. It can be seen that Case 1, which corresponds to the maximum value of FX (frontal wind), results in the highest mount rotation at 5.56 arcsec, which consumes 56% of the 10 arcsec error budget. This error corresponds to the simplified case of the wind increasing from 0m/s to 10m/s without any referencing. The magnitude of force corresponding with a wind increase from a 10m/s steady wind to a 15m/s gust is 25% larger. More detailed evaluation methods will be required in future design phases.

Table 5-2: Mount rotation under wind and temperature gradient loads

Wind Load Parameters											
	Wind speed	[m/s]	10.0								
	Air density	[kg/m^3]	1.225								
	Primary diameter	[m]	6.0								
	Primary area (ellipse)	[m^2]	34.9								
Load Cases											
-wind load coefficients per 19007-CLC-002-A											
	Case		1	2	3	4	5	6	7	8	9
	Case type		WIND	WIND	WIND	WIND	WIND	WIND	THERMAL	THERMAL	THERMAL
	Case label		CFX_Max (fore-aft)	CFY_Max (lateral)	CFZ_max (vertical)	CMX_max (roll)	CMY_Max (pitch)	CMZ_Max (yaw)	dTX	dTY	dTZ
	Elevation angle	[deg]	30	90	80	90	90	20	-	-	-
	Wind azimuth angle	[deg]	40	110	10	100	180	90	-	-	-
	Wind coefficient, CFx	[ ]	1.33	-0.31	0.84	-0.17	-0.46	-0.07	-	-	-
	Wind coefficient, CFy	[ ]	0.03	0.14	0.00	0.13	0.02	0.01	-	-	-
	Wind coefficient, CFz	[ ]	-0.07	0.42	-0.94	0.24	0.47	-0.01	-	-	-
	Wind coefficient, CMx	[ ]	0.01	-0.16	0.03	-0.17	0.00	0.02	-	-	-
	Wind coefficient, Cmy	[ ]	0.09	-0.08	-0.02	-0.04	-0.19	0.02	-	-	-
	Wind coefficient, CMz	[ ]	0.07	-0.09	0.02	-0.10	0.00	-0.21	-	-	-
	Temperature gradient, dTX	[^{0}C/m]	-	-	-	-	-	-	0.17	0.00	0.00
	Temperature gradient, dTY	[^{0}C/m]	-	-	-	-	-	-	0.00	0.17	0.00
	Temperature gradient, dTZ	[^{0}C/m]	-	-	-	-	-	-	0.00	0.00	0.17
Mount Rotation due to Wind											
-rotations below are measured at ERA origin											
	ROTX	[arcsec]	-0.04	-1.19	0.10	-1.25	-0.08	0.03	-	-	-
	ROTY	[arcsec]	5.55	-2.10	3.57	-1.08	-3.98	-0.01	-	-	-
	ROTZ	[arcsec]	0.37	-0.53	0.11	-0.60	0.01	-1.10	-	-	-
	Total rotation (RSS)	**[arcsec]**	**5.56**	**2.47**	**3.57**	**1.76**	**3.99**	**1.10**	**-**	**-**	**-**
Mount Rotation due to Temperature Gradient											
	ROTX	[arcsec]	-	-	-	-	-	-	0.00	2.44	0.00
	ROTY	[arcsec]	-	-	-	-	-	-	-2.65	0.00	0.11
	ROTZ	[arcsec]	-	-	-	-	-	-	0.00	-0.01	0.00
	Total rotation (RSS)	**[arcsec]**	**-**	**-**	**-**	**-**	**-**	**-**	**2.65**	**2.44**	**0.11**

Temperature gradient cases were also run with gradients of 1^{0}C/6m applied to the mount in x, y and z directions. These correspond to cases 7 to 9 in Table 5-2. At this point these values are simply placeholders. Calculations for expected thermal gradients under various referenced and absolute pointing scenarios will need to be developed and used as input to pointing error calculations and requirements for thermal control.

5.5 Survival Stress Analysis

The following is an initial calculation of the various survival loads acting on the mount, which is used to determine the governing loads for initial stress assessment.

- **Dead Load:** The total ERA assembly weight estimated at 3300kg = **32kN.** Note the ERA assembly weight is currently under review by NRC and will be updated as required for future mount analysis.
- **Wind Loads:** The SBA requirements document (RD01) specifies a 50m/s "average" survival wind speed. Based on consultation with NRAO it was confirmed that this wind speed should be used in conjunction with the minimum safety factors specified in RD01, specifically a stress safety factor of 1.1 under survival conditions. Note that ASCE 7-10 has a mapped wind speed for New Mexico of 51m/s (3 second gust, 700 year return, Occupancy Category II). ASCE 7-10 requires a load factor of 1.0 on survival wind, and a typical resistance factor of 0.9 (effectively corresponds to a safety factor of 1/0.9 = 1.1). Thus, the approach used in RD01 yields similar overall safety factors to ASCE 7-10. The magnitude of the maximum frontal wind pressure is estimated as P = ½ x ro x v^2 x Cp = 0.5 x 1.22kg/m^3 x (50m/s)^2 x 1.33 = 2.0kPa, where 1.33 is the maximum front wind pressure coefficient. The elliptical frontal area of the dish is 34.9m^2, for a total wind force of **70kN**.
- **Snow Load:** RD01 specifies 25cm of snow. Assuming density of 300kg/m^3, the corresponding pressure load is 300kg/m^3 x 9.8N/kg x 0.25m = 0.74kPa, and the total snow weight on the dish is 0.74kPa x 34.9m^2 = **26kN**.
- **Ice Load:** RD01 specifies 2.5cm ice. Assuming density of 900kg/m^^{3} (glaze ice), the corresponding pressure load is 900kg/m^3 x 9.8N/kg x 0.025m = 0.22kPa, and the total ice weight on the dish is 0.22kPa x 34.9m^2 = **8kN**.
- **Seismic:** RD01 species "the antenna and foundation shall be designed to withstand a low probability earthquake with up to 0.2g peak acceleration in either the vertical or the horizontal axis", with low probably being defined as 2% in 50 years in spec. The seismic load imparted by the ERA is thus 32kN x 0.2g = **6kN.** Note that RD01 specifies that response spectrum analysis should be used as the basis of the seismic analysis, using at least 80% effective modal mass, 1.5% damping, and SRSS mode combination. This will be carried out in future phases; however it is not expected to govern the mount design. Note that no response spectra data is included in RD01 at this time.
- **Live Loads:** In addition to any equipment payloads specified, it is proposed that access floor areas be designed for a minimum distributed load of 4.8kPa (100psf) or a point load of 1.33kN (300lbs). This loading should be reviewed with NRC and NRAO.

Based on the above, it can be seen that in survival loads on the main structural and mechanical elements of the mount will be governed by wind. Applicable load combinations in ASCE 7-10 are (1.2D + 1.0W + 0.5S) and (0.9D + 1.0W), where D = dead, W = wind, S = snow.

Sample deflection and stress results are shown below for the case of gravity load plus 50m/s frontal wind load. The results indicate stresses will be less than 20Mpa (2900psi), indicating very large margin of safety (greater than 10:1).

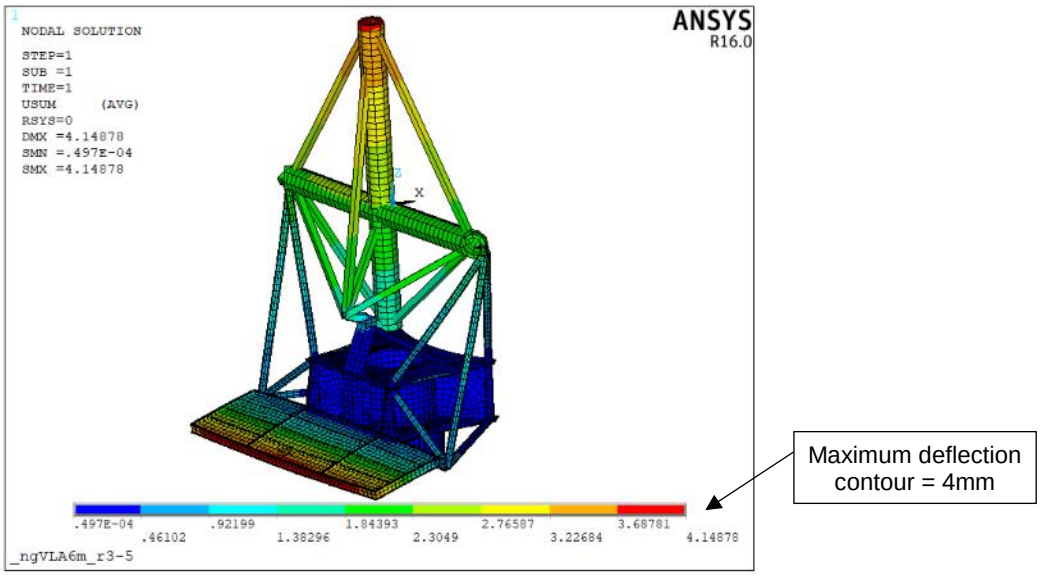

Figure 5-6: Deflection under 50m/s survival wind loads plus gravity

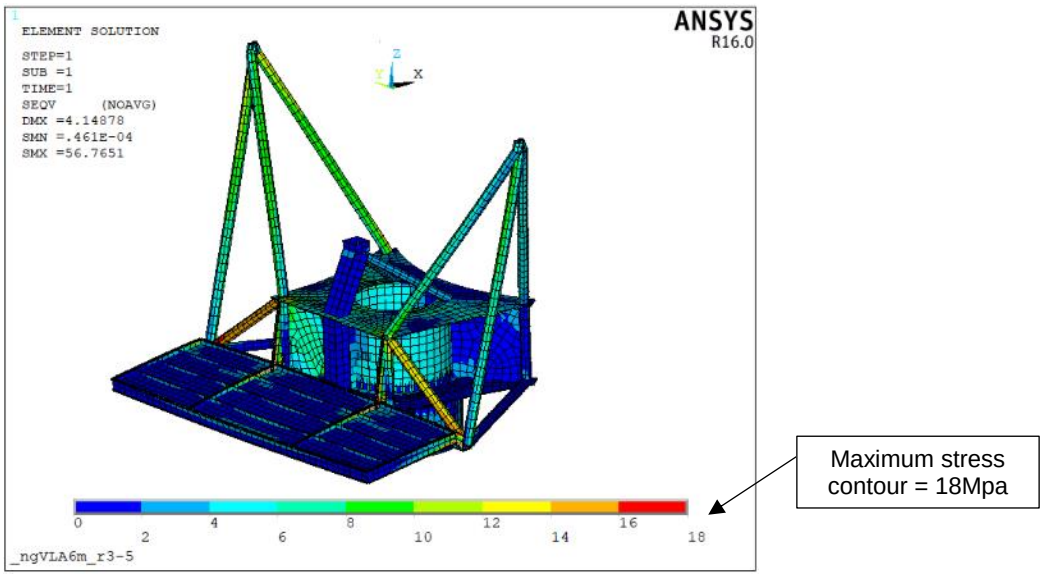

Figure 5-7: Mount stresses under 50m/s survival wind load plus gravity

5.6 Foundation Analysis

The foundation conceptual design utilizes a shallow slab foundation with preliminary dimensions 5.0m x 5.0m x 0.6m. A square footing is assumed for initial sizing, however a circular footing can be considered in future design phases.

Geotechnical information for the site was provided in a 1999 report for the ALMA antennas (RD03). The proposed foundation design for that project was based on a cylindrical slab footing supported by an additional three piers bearing at depth of approximately 6m. In order to limit settlement, it was recommended that bearing pressure at the base of the piers be limited to 287kPa (6000psf). No information was provided for recommended bearing pressure for shallow foundations.

For the survival wind load of 50m/s the calculated bearing pressure for a 5.0m x 5.0m slab foundation is approximately 60kPa (1250psf). This is will likely provide an adequate bearing pressure for a shallow slab foundation, but this should be confirmed via a project-specific geotechnical study.

Soil stiffness data from RD03 was also used to estimate impact of soil stiffness on pointing error. The soil shear modulus in RD03 is listed as 35Mpa (5ksi) at depths from 1-2m. At 10m/s normal operating wind the foundation tilt is estimated at 0.2 arcsec, which is 2% of the 10 arcsec referenced pointing error requirement. Thus, soil stiffness is not a major consideration in overall antenna pointing.

6 CALCULATIONS

Table 6-1 lists calculation files prepared by Sightline for the mount conceptual design. These files are included as an appendix to this report.

Table 6-1: Calculation listing for concept design

Calculation Number	Description
19007-CLC-001-A	Mount mass budget
19007-CLC-002-A	Wind loads
19007-CLC-100-A	Foundation calculations
19007-CLC-200-A	Rack and pinion calculations

7 DRIVE TRADE-STUDY

Note that the majority of the information presented in this section was provided in a separate trade-study report in Nov 2020. It has been included in this document for completeness.

This section summarizes a trade study of various drive mechanisms considered for the ngVLA6m mount. The following were identified as primary candidates for the azimuth and elevation drive mechanisms, each of which are described in the sections below:

- Option 1: Rack and pinion with gearmotor
- Option 2: Rack and pinion with direct-drive motor ("hybrid" option)
- Option 3: Direct drives

The authors would like to express their appreciation to Phase USA who assisted in this study by providing initial sizing and costing inputs for the motor components of Options 2 and 3.

This document focuses on the mechanical aspects of the design trades, and is intended to serve as an input into an overall trade study of the drive systems considering controls aspects, capital cost and operational cost.

7.1 Requirements

Drive system requirements were derived from RD01. The key requirements are summarized in the tables below, with Table 7-1 showing the kinematic requirements and Table 7-2 showing the maximum wind torques for various wind conditions. Wind loads were based on pressure coefficients provided in RD02. In the "limit" wind condition the telescope must be functional, but there are no pointing requirements. In the "survival" wind condition the axes are static and locking devices may be used.

Table 7-1: Kinematic requirements

Parameter	Req. #	Value	Traceability
Range, tracking	SBA0801 SBA0802	AZ: +/-270^0 EL: 12^0 - 88^0	SYS1201
Speed, slewing	SBA0901 SBA0902	AZ: 90^0/min EL: 45^0/min	SYS1107
Speed, tracking	SBA0906 SBA0907	AZ: 7.5^0/min EL: 3.5^0/min	
Acceleration	SBA0903 SBA0904	AZ: 4.5^0/s^2 EL: 2.25^0/s^2	

Table 7-2: Wind torques

Operating condition		Precision		Normal		Limit		Survival
Wind type		**Steady**	**Gust**	**Steady**	**Gust**	**Steady**	**Gust**	**Steady**
Wind speed	[m/s]	5	7	7	10	15	20	50
Azimuth Drive	[kN-m]	0.7	1.3	1.3	2.6	5.9	10.6	66
Elevation Drive	[kN-m]	0.7	1.4	1.4	2.9	6.5	11.5	72

7.2 Option 1: Rack and Pinion with Gearmotor

Option 1 utilizes a rack and pinion drive, where the pinion is driven by a conventional gearbox-servo motor assembly. The pinion drives are provided in pairs such that during observing one pinion is back-driven in order to eliminate backlash.

Preliminary sizing of the main drivetrain components was carried out with the following main assumptions:

- The rack, pinion and gearbox were sized to withstand the survival-case wind loads in order to provide high stiffness and long life, and also to provide the option of using parking brakes on the drive train instead of stow pins
- The rack, pinion and gearbox were sized assuming only one pinion drive on each axis takes the entire load in order to provide redundancy
- The motors were sized with sufficient torque and power to operate in the limit-case wind loads
- If the brakes are to be used for stowing, standard motor parking brakes will not be sufficient, and higher capacity brakes would need to be provided between the gearbox and motor

The following summarizes the preliminary component sizes:

- Rack and pinion gear size
  - Azimuth
    - Gear module: 10
    - Gear contact width: 100 mm (pinion)
    - Pinion pitch radius: 82.1 mm
    - Slewing gear radius: 901.7mm
  - Elevation:
    - Gear module: 4
    - Gear contact width: 45 mm (pinion)
    - Pinion pitch radius: 40.8 mm
    - Elevation rack radius: 2500 mm
- Gearbox
  - Azimuth:

        - Stober, multi-stage planetary gear reducer with flanged output
        - Overall gear ratio: 600:1
    - Elevation:
        - Stober, multi-stage planetary gear reducer with flanged output
        - Overall gear ratio: 91:1
- Motor
    - Azimuth & Elevation motors
        - Allen Bradley, Kinetix increased inertia, servo motor
        - 1.4kW rated output
        - 4.74 N-m continuous rated stall torque

7.2.1 Azimuth Axis

Refer to Section 4.4.1 above for description of rack and pinion design for azimuth axis.

7.2.2 Elevation Axis

Refer to Section 4.4.2 above for description of rack and pinion design for elevation axis.

7.2.3 Variation 1 – Industrial gearboxes vs servo-precision units

The Stober gearboxes specified above are precision servo style units which carry a higher cost, especially in larger sizes. Since backlash will be actively compensated for in this application, the extra accuracy may not warrant the extra cost. As such, industrial planetary units were also investigated. The units selected for evaluation are made by Bonfiglioli and are sized to have the same torque capacity and gear ratio as the servo units. Key considerations for the industrial gearboxes are:

- The overall size of the industrial units is comparable with the servo units, therefore there are no driving packaging concerns.
- The industrial units are approximately 1/3 the cost.
- The industrial units have approximately 10-20% the stiffness of the servo units.

Further info on stiffness comparison is provided in section 0 below.

7.2.4 Variation 2 – Roller pinion system for elevation drive

A key maintenance concern of the elevation rack and pinion is the external gear lubrication required. A roller pinion system was investigated as it can typically operate without external lubrication. The system uses internally lubricated rollers on the pinion which engage with chain sprocket like teeth on the rack. The image below shows the arrangement of the pinion and gear teeth.

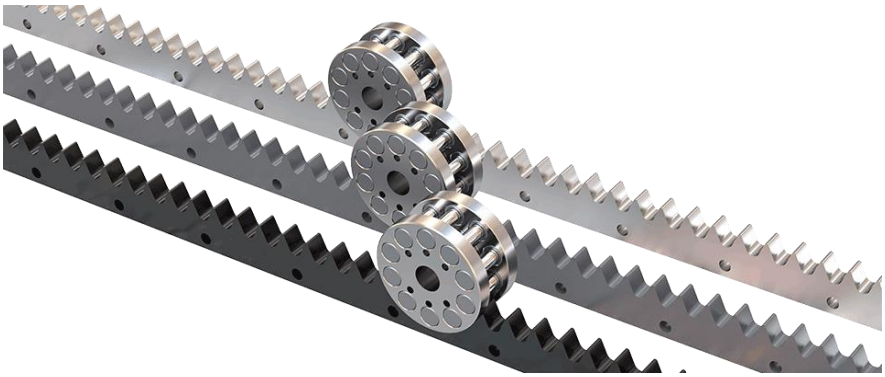

Figure 7-1: Roller pinion components

Nexen group was contacted to provide a system as they are one of only two known manufacturers of commercial roller pinion systems. Key details of their proposed system are as follows:

- RPS32 size components are capable of meeting limit level performance requirements.
- Nexen confirmed that the system will be able to operate without external lubrication in this application.
- Standard available curved rack segments are available with a 2.2m radius. Custom racks are possible, however at a substantial cost penalty.

Further comparison of the roller pinion system vs rack and pinion is provided in section 7.6 below.

7.3 Option 2: Rack and Pinion with Direct Drive Motor

Option 2 utilizes a rack and pinion drive similar to Option 1, except instead of a gearmotor driving the pinion a direct-drive motor is used. The main advantage of this approach is that the additional flexibility of the gearbox is eliminated. The main disadvantage of this approach is that the direct drive motors are larger and more expensive than more common gearmotors. The impact of gearbox stiffness is described in section 0.

Phase USA provided preliminary sizing and costing information for this drive option.

7.3.1 Azimuth Axis

The azimuth drive motors proposed by Phase are high torque TK series units with an integral pinion. For comparison purposes the drives are shown driving the outer ring of the slewing bearing as with the Option 1 drive system. Details of the motors are as provided in Table 7-3.

Table 7-3: Azimuth drive specifications – "Hybrid" drive option

TK370-380 AZ Axis		
Nominal Torque	Nm	1,276
Rated Speed	rpm	26
Nominal Power	kW	3.47
S6 Duty Torque	Nm	2,026
Peak Torque	Nm	4,835
Motor Constant	N*m/sqrt(watt)	24.221
Torque Constant	N*m/Amp	87
Nominal Current, 1rpm, S1	Amp RMS	16.00
Max. S6 Current 40%, 1 rpm, 10min	Amp	34.00
Peak Current at Max Torque	Amp	76.50

The following images show how the direct drive motors package.

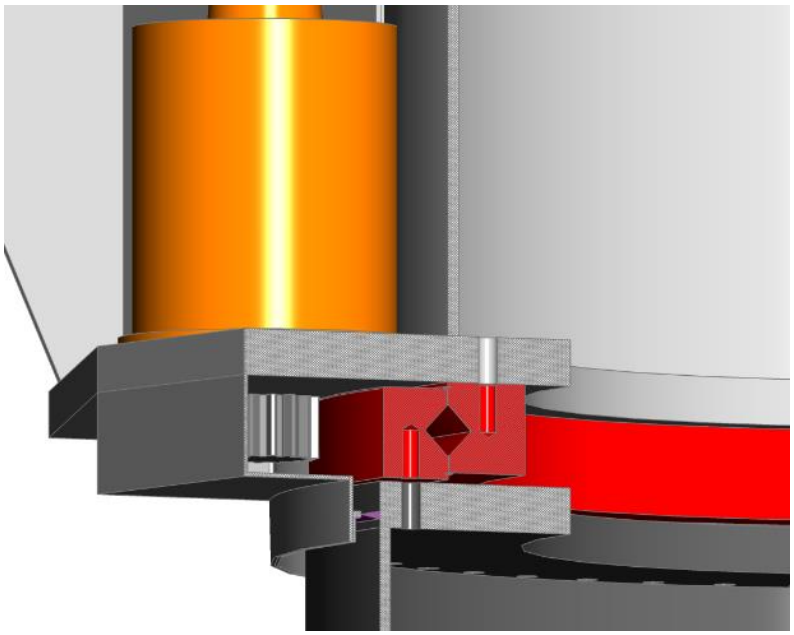

Figure 7-2: Azimuth direct drive motor packaging

As shown in the following image, the direct drive motor is larger than the gearmotor assembly. This makes packaging more difficult, particularly with regard to placement of the motor flange relative to the slewing bearing and pinion, but it is still feasible without significant structural redesign. If the pinion is moved further away from the motor flange (to provide clearance with the slewing bearing), additional support of the motor shaft may be required.

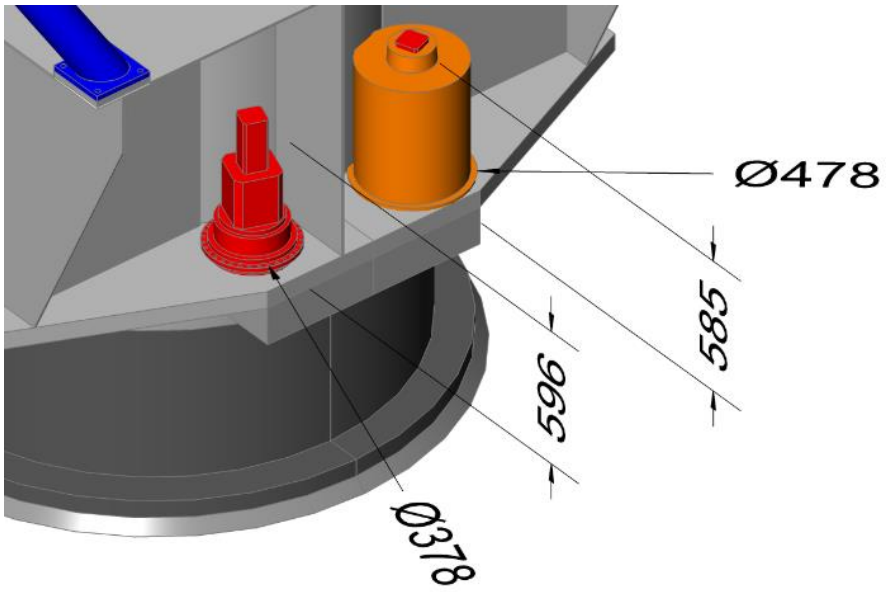

Figure 7-3: Azimuth direct drive motor (orange) vs gearmotor (red) size comparison

7.3.2 Elevation Axis

The motors proposed for the elevation axis are the same style TK series units as the azimuth drives, albeit with a slightly smaller size. Details of the proposed motors are provided in Table 7-4.

Table 7-4: Elevation drive specifications – "Hybrid" drive option

Torque Motor EL Axis		
Nominal Torque	Nm	228
Rated Speed	rpm	73
Nominal Power	kW	1.75
S6 Duty Torque	Nm	354
Peak Torque	Nm	881
Motor Constant	N*m/sqrt(watt)	8.65
Torque Constant	N*m/Amp	76
Nominal Current, 1rpm, S1	Amp RMS	2.99
Max. S6 Current 40%, 1 rpm, 10min	Amp	4.94
Peak Current at Max Torque	Amp	14.21

Key considerations for this option are as follows:

- As with the azimuth drive, the direct drive motor is larger in diameter than the gearmotor assembly. The larger size will require a larger angular spacing than the gearmotor assembly and therefore a longer gear segment (approximately 4 degrees, ~200mm).
- Other packaging and guiding requirements are similar to Option 1.
- If stowing with the pinion gears are to be used, this option would require significantly larger capacity brakes since there is no gear reduction.

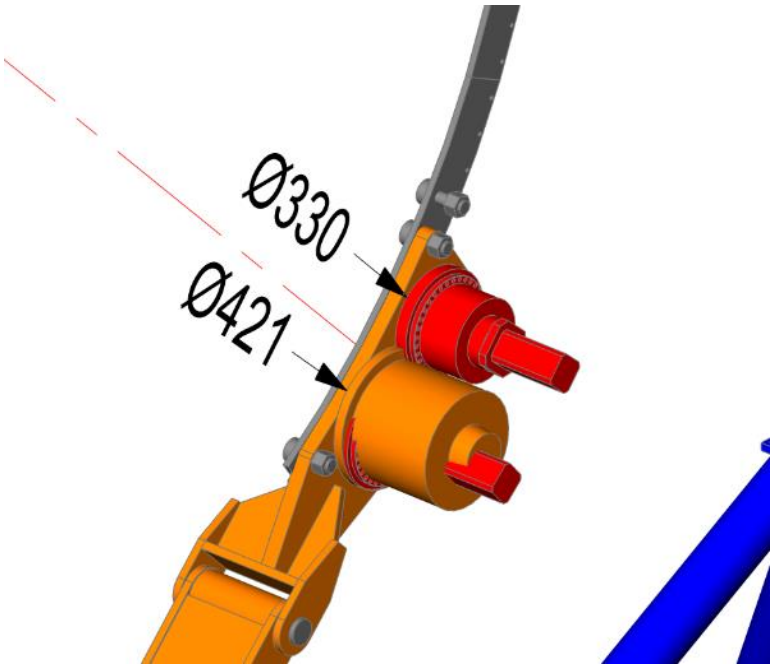

Figure 7-4: Elevation direct drive motor (orange) vs gearmotor (red) size comparison

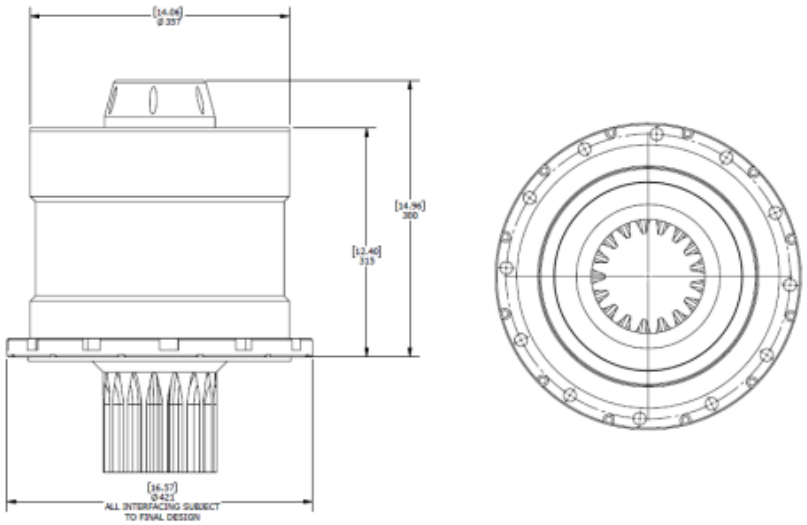

Figure 7-5: Elevation axis direct drive motor dimensions

7.4 Option 3: Direct Drive

The direct drive option provides non-contact drive system for both axes. Again, Phase USA was consulted to provide preliminary specification of the azimuth and elevation drives. This drive system has two fundamental benefits:

1. No mechanical contact or wear items
2. Increased control capability and better control system bandwidth due to minimized mechanical compliance

7.4.1 Azimuth Axis – Internal Drive

For the azimuth axis, Phase proposed two supply options: 1) supply of only the stator and rotor for integration by the telescope designers, or 2) supply of an integrated package with the slewing bearing. Figure 7-6 shows the basic rotor and stator components, and Figure 7-7 integrated concept.

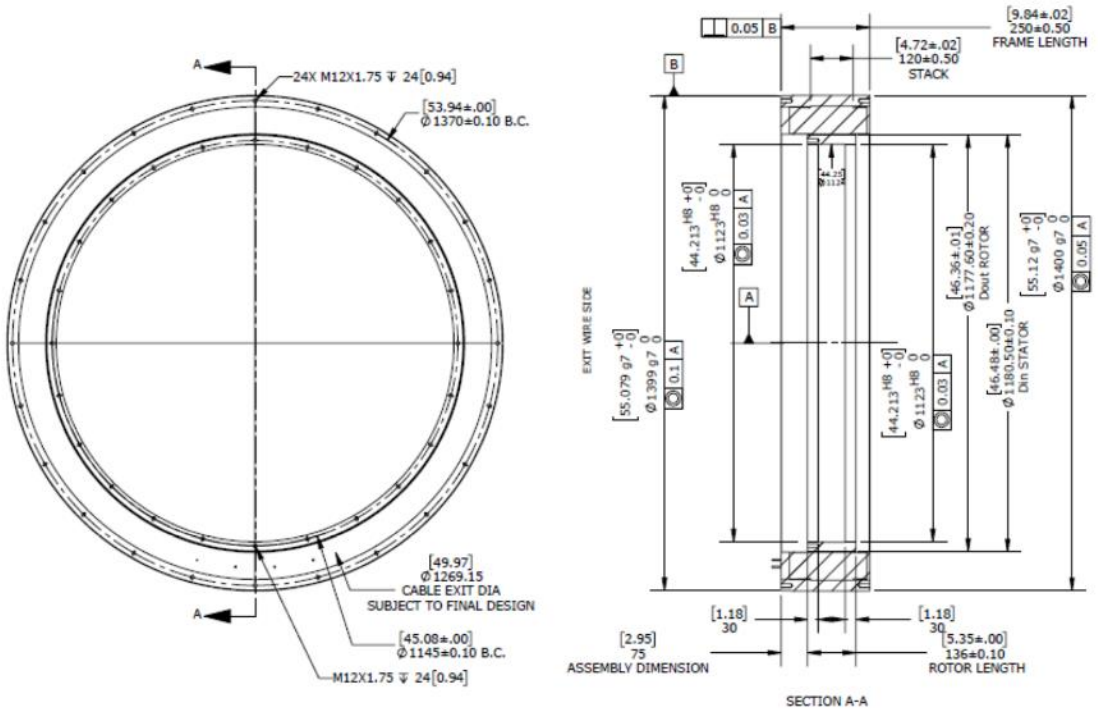

Figure 7-6: Azimuth axis, direct drive rotor and stator concept from Phase

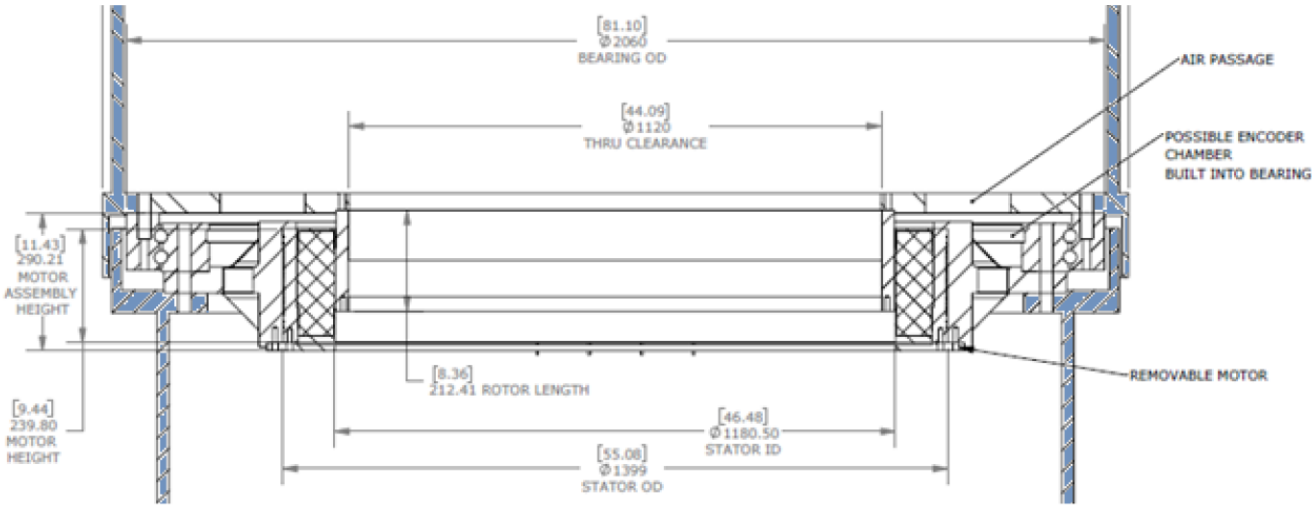

Figure 7-7: Azimuth axis, direct drive integrated concept from Phase

The integrated concept provides the rotor and stator as a complete motor which can be pre-assembled prior to site assembly. A complete integrated motor assembly offers benefits including capability of pre-testing of the motor and encoder, simplified logistics via shipping of a single component, and easier system assembly on site. The final motor package would include the following components:

- Main bearing
- TK rotor and stator
- Encoder tape and read head(s)
- Flanging for mechanical interfaces to the main structure
- Brake disc and/or other provisions to assist in supporting the braking units
- No-load testing results and certification

The specifications of the proposed drive are provided in Table 7-5.

Table 7-5: Azimuth drive specifications - direct drive option

TK1340-120 AZ Axis		
Nominal Torque	Nm	6,114
Rated Speed	rpm	7
Nominal Power	kW	4.45
S6 Duty Torque	Nm	19,333
Peak Torque	Nm	26,246
Motor Constant	N*m/sqrt(watt)	151.81
Torque Constant	N*m/Amp	675
Nominal Current, 1rpm, S1	Amp RMS	9.05
Max. S6 Current 40%, 1 rpm, 10min	Amp	28.36
Peak Current at Max Torque	Amp	49.00

At the time that Phase was consulted for sizing of the azimuth drive system the utility wrap and encoder systems were not yet conceptualized. In the current concept the utility wrap is located above the slewing ring and drive, which would block access to the drives. If an internal drive system were to be viable, the packaging of the bearing, drives, utility wraps and encoders would need to be revisited in order to ensure a viable solution.

7.4.2 Azimuth Axis – External Drive

To improve on the packaging issues with the internal direct drive motor on the azimuth axis, it may be possible to use an externally mounted drive system with a segmented direct drive design (similar to that proposed by Phase for the elevation drive which is described below) located on the outside of the azimuth bearing. Since the torque requirements for the azimuth and elevation axis are similar but the

azimuth drive radius is approximately 36% of the elevation axis, 3-4 of the drive units proposed for the elevation axis would be required. The image below shows a rough layout of this option.

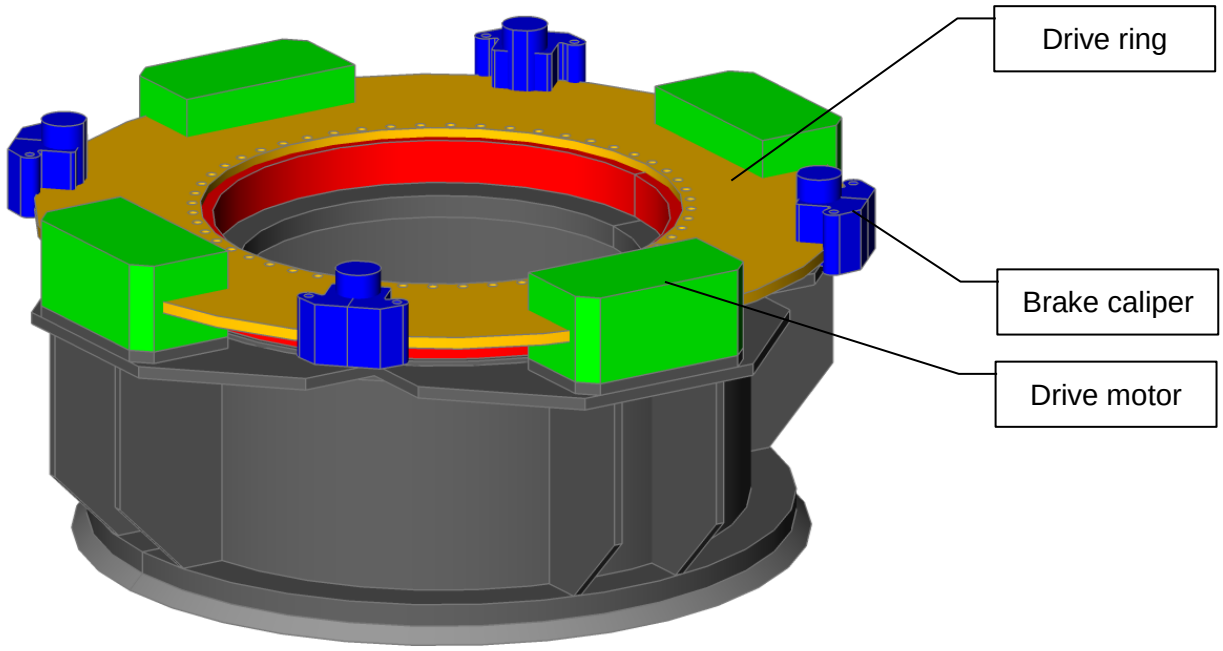

Figure 7-8: Segmented azimuth drive concept

Key observations about this option are as follows:

- Minimal changes are required to current azimuth bearing and pedestal design
- The same motors can be used for both the azimuth and elevation axes (assuming packaging with a smaller drive radius is possible, this would need to be reviewed with Phase)
- Motors are placed outside of the yoke which provides clear access for maintenance and removal
- External mounting may improve cooling

7.4.3 Elevation Axis

The elevation motor proposed by Phase is composed of one double sided module with 90 mm radial width magnets, a circumferential length of 660 mm and a mass of approximately 100kg. Coil sections

and magnet segments are assembled on a 2.575 m radius. The rotor consists of 4 double sided segments carrying the magnet poles. The segments are joined together to create the full arc defining the overall angular thrust area. This segmented ring is integrated to the main backing structure of the telescope.

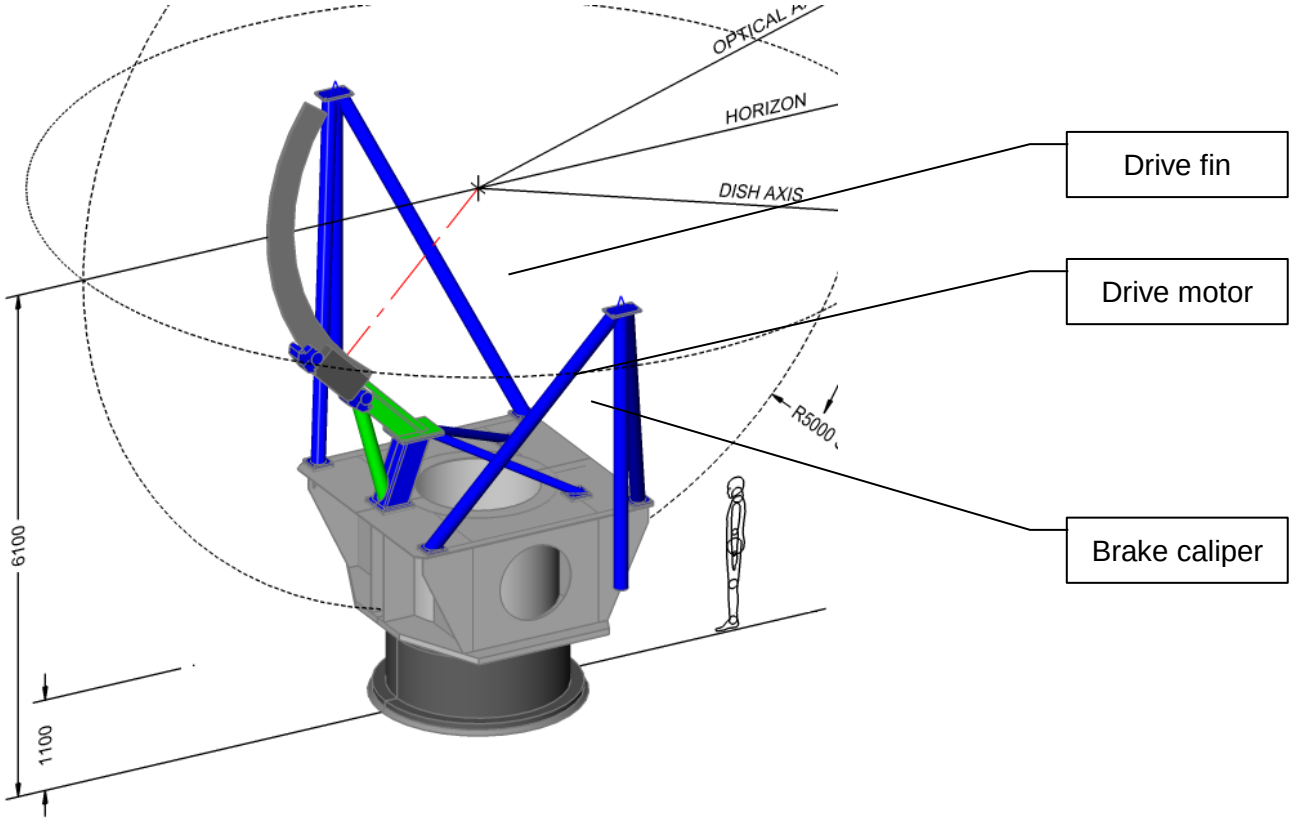

Figure 7-9: Elevation axis, direct drive concept

The motor section is equipped with a side slot which can be used to axially pull out the section against the magnetic attraction for maintenance purposes. The motor section will be mounted on a linkage system, similar to the rack and pinion drive. As the air gap is critical to motor operation and performance, the linkage likely needs to be axially guided relative to the stator fin using rollers.

From an electrical point of view, each coil section is independent and is equipped with an embedded power drive which is fed through a DC bus line. The interface with the control system is through an Ethernet bus with EtherCat protocol. Additionally, a 24 VDC auxiliary supply is required for the drive control power. Phase implemented this approach on GTC, ALMA, and LSST telescopes, among others, and further developed this technology for large windmill applications where the flexibility of the hub under high wind load presents similar considerations to this project. The specifications of the proposed drive are provided in Table 7-6.

Table 7-6: Elevation drive specifications – direct drive option

TK5000-090 EL Axis		
Nominal Torque	Nm	10,443
Rated Speed	rpm	2.1
Nominal Power	kW	2.26
S6 Duty Torque	Nm	30,671
Peak Torque	Nm	30,671
Motor Constant	N*m/sqrt(watt)	485.06
Torque Constant	N*m/Amp	2,097
Nominal Current, 1rpm, S1	Amp RMS	4.94
Max. S6 Current 40%, 1 rpm, 10min	Amp	14.28
Peak Current at Max Torque	Amp	18

7.4.4 Brakes

To meet the project design requirements, the direct drive option would require a separate braking system to stop the telescope in the event of power failure. The proposed concept is to use spring applied, hydraulically released brake calipers that engage the drive fins on the elevation and azimuth axes (see Figure 7-8 and Figure 7-9). The calipers will be operated with dedicated hydraulic powerpacks that can be placed on the equipment platform

VCS-FL **Spring Applied – Hydraulically Released**

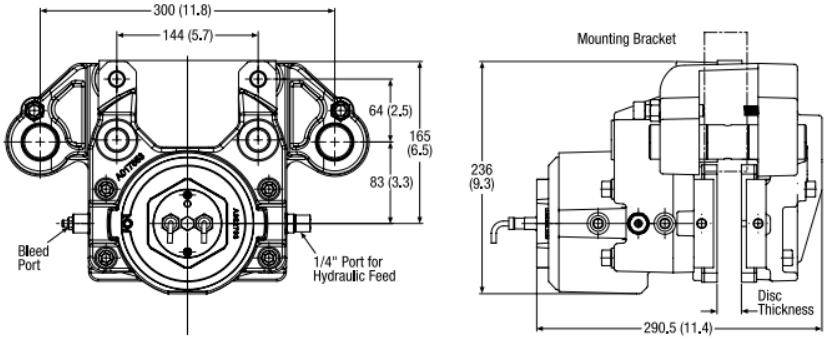

The Twiflex VCS-FL disc brake caliper comprises a single spring module forming the 'active' side of this floating unit and is available for use where space is limited or to accommodate axial disc float of ±6mm (0.24 in).

Braking force ratings are achieved through a combination of shim number and air gap setting. Spring fatigue life is a function of the caliper rating.

The ratings shown in the table are based on fully bedded in and conditioned brake pads with a nominal friction coefficient μ = 0.4. Twiflex disc brakes must be used with Twiflex asbestos free brake pads.

Effective disc radius = actual radius (m) – 0.064m
(Effective disc radius = actual radius (ft) – 0.21 ft)

Figure 7-10: Direct drive brake calliper

7.5 Effect of Drivetrain Stiffness on Natural Frequency

Table 7-7 shows drivetrain stiffness calculations based on catalogue data provided by Stober, Atlanta and Bonfiglioli for the following configurations:

- Option 1: Rack and pinion with servo gearmotor
- Option 1-v1: Rack and pinion with industrial gearmotor
- Option 2: Rack and pinion with direct drive motor

Option 1 includes the stiffness of the gearbox, pinion, and rack, whereas Option 2 includes the stiffness of the pinion and rack only. Option 3 effectively has no mechanical drivetrain compliance and is thus not included in the table. Local flexibility of mounting structures, tow-links, etc, is not accounted for.

The calculations indicate that for the azimuth axis the addition of a gearbox has a significant impact on stiffness, whereas for the elevation axis there is less of an impact:

- Option 1
  - Azimuth stiffness is 41% of Option 2
  - Elevation stiffness is 82% of Option 2
- Option 1-v1
  - Azimuth stiffness is 12% of Option 2
  - Elevation stiffness is 33% of Option 2

The rotational frequencies due to drive compliance (assuming a rigid structure) are estimated at the bottom of the table for a rigid structure assumption.

Table 7-7: Drivetrain stiffness calculations

		Units	OPTION 1: Rack and Pinion with Servo gearmotor		OPTION 1-v1: Rack and Pinion with Industrial gearmotor		OPTION 2: Rack and Pinion with Direct-Drive Motor	
			AZ	EL	AZ	EL	AZ	EL
Calculate drivetrain linear stiffness								
	Gearbox stiffness	[N-m/arcmin]	1969	837	393.5	90	n/a	
	Gearbox stiffness	[N-mm/rad]	6.8E+09	2.9E+09	1.4E+09	3.1E+08		
	Pinion radius	[mm]	82.1	40.8	82.1	40.8		
	Linear stiffness, gearbox only	[N/mm]	1.0E+06	1.7E+06	2.0E+05	1.9E+05		
	Linear stiffness, pinion + rack only	[N/mm]	1.4E+06	3.7E+05	1.4E+06	3.7E+05	1.4E+06	3.7E+05
	Linear stiffness, gearbox + pinion + rack	[N/mm]	**5.9E+05**	**3.1E+05**	**1.8E+05**	**1.2E+05**	**1.4E+06**	**3.7E+05**
Calculate drivetrain total rotational stiffness								
	Rack radius	[mm]	900	2500	900	2500	900	2500
	Stiffness at rotation axis	[N-mm/rad]	**4.8E+11**	**1.9E+12**	**1.4E+11**	**7.8E+11**	**1.2E+12**	**2.3E+12**
	Stiffness ratio Option 1 to Option 2	[ ]	**41%**	**82%**	**12%**	**33%**		

Figure 7-11 and Figure 7-12 plot natural frequency of the total antenna, including structural stiffness, as a function of drive stiffness based on mount FEA. It can be seen that the drivetrain stiffness does not significantly impact the natural frequency of the overall antenna, except for the azimuth axis with Option 1-v1. Therefore, the additional stiffness of Options 2 and 3 may be of little benefit strictly from the perspective of overall antenna frequency, however this should be reviewed with drive and controls specialists for further evaluation.

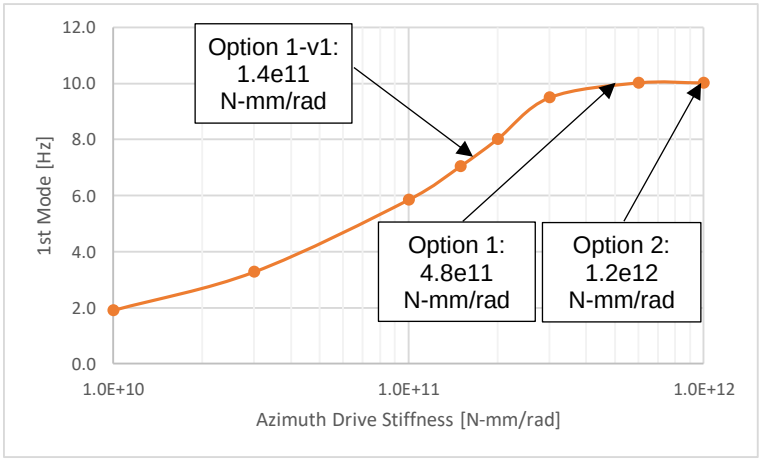

Figure 7-11: Frequency vs azimuth drive stiffness

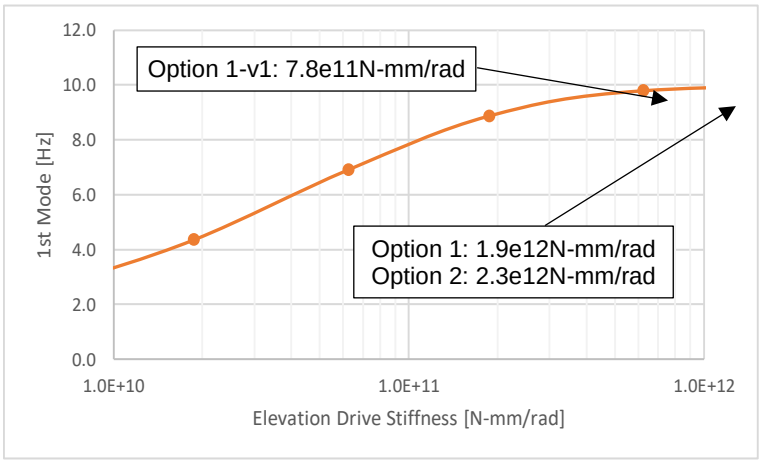

Figure 7-12: Frequency vs elevation drive stiffness

7.6 Comparison Matrix

The following table summarizes the design and operational considerations for all drive options. Cost is evaluated qualitatively below, and a quantitative cost estimate has been provided separately to NRC.

- Green text indicates a significant advantage
- Orange text indicates a minor disadvantage
- Red text indicates a significant disadvantage

Table 7-8: Drive option comparison matrix

	OPTION 1 Precision Gearbox	OPTION 1 – v1 Industrial Gearbox	OPTION 1 – v2 Roller Pinion	OPTION 2 Hybrid Drive	OPTION 3 Direct Drive
Capital Cost	Med	Low	High	High	High
Performance	High accuracy gearing in gearbox Small motors possible due to higher overall gear reduction	Standard quality gearing in gearbox Small motors possible due to higher overall gear reduction	Provides near-zero backlash operation on elevation axis Small motors possible due to higher overall gear reduction	Removes stiffness effects of gearboxes Oversize motors required for thermal stability	Mechanical stiffness only affected by mounting of motors Oversize motors required for thermal stability Control bandwidth is higher than geared solutions allowing performance gains in settling times; performance benefit needs to be quantified by controls analysis
Operations and maintenance considerations	Rack & pinion lubrication via auto lubrication system Periodic check and adjustment of R&P backlash likely required, possible wear Gearboxes are claimed to be maintenance free, however it would need to be confirmed for this specific application	Rack & pinion lubrication via auto lubrication system Periodic check and adjustment of R&P backlash likely required, possible wear Gearboxes are oil filled and require periodic fluid change (~annually)	Roller rack & pinion does not require external lubrication Periodic check and adjustment of R&P backlash likely required, possible wear	Rack & pinion lubrication via auto lubrication system Periodic check and adjustment of R&P backlash likely required, possible wear	No mechanical contact and wear items If external direct drive can be adopted, good maintenance access is possible
Other	Multiple vendor options and standardized products allow easy path for future replacements/upgrades	Multiple vendor options and standardized products allow easy path for future replacements/upgrades	Proprietary components from single vendor may cause availability problems over life of telescope	Fixed form factor components may limit future upgrade possibilities	Fixed form factor components may limit future upgrade possibilities

7.7 Drive Trade-Study Recommendations

Based on the information collected during this trade study, Sightline recommends that Option 1 (servo-based rack and pinion) and Option 3 (direct drive with segmented azimuth motor) be selected for further evaluation. The key reasons are as follows:

- The servo-based rack and pinion system provides a good balance of cost and performance with the added benefit that it allows component selection from a multitude of vendors as well as the simplest option for future upgradability.
- The largest benefit of the direct drive system is related to the controllability and settling performance which is outside of Sightline's expertise. As such selection between the direct drive and rack and pinion options cannot be made without analysis and input from further control evaluation.
- While lower in cost, the low stiffness of the industrial gearbox option results in a noticeable effect on the overall telescope stiffness, particularly on the azimuth axis.
- The roller pinion option is comparatively expensive and limited in availability which overshadows the benefit of not requiring external lubrication.
- The hybrid drive system does not offer appreciable cost savings or performance improvement over the direct drive option while still having the main disadvantages of a rack and pinion system.

8 ERROR BUDGETS

8.1 Surface Accuracy Error Budget

Surface accuracy is defined as the deviation of the manufactured reflector surface from the designed surface profile. The accuracy can be stated either in the plane tangent to the reflector surface or in the main aperture plane normal to the boresight direction (the main reflector optical axis). For the ngVLA the surface accuracy specifications are stated in the main aperture plane (see Table 9-1 below). The specifications are for different operating conditions (precision or normal).

Surface error can be caused by the manufacturing process (mould accuracy, part separation from the mould, tensioning of the reflector) or by dynamic wind, gravity, and thermal effects (differential rates of thermal expansion/contraction, or thermal gradients set up by solar irradiation). The dynamic effects will deform the reflectors and the mounting structure, which will cause surface error.

The surface accuracy error budget identifies sources of surface error for both the primary and secondary reflectors, allocates error amounts to the sources and both reflectors, and defines the calculation of overall error using the allocated amounts. The budget is used both to determine compliance with the specifications when the achievable accuracy is known or estimated for each error source, and to estimate the available error margin in a source using the total allowed error in the specification. Surface accuracy budgets with the most recent accuracy data and estimates are shown in Table 8-1 for precision operating conditions and Table 8-2 for normal operating conditions. The tables include manufacturing error derived from the mould surface accuracy and the accuracy ratio of the mould and the part built from it. Totals for primary and secondary reflector surface accuracy and overall combined accuracy are shown, as well as antenna efficiency at selected frequencies across the operational band (calculated from the total surface accuracy).

Table 8-1 Antenna Surface Accuracy Error Budget – Precision Operating Conditions

Precision							
Wind	7	m/s	Night	Temperature	15	C min	
Requirement	160	micron RMS					
Primary			BOE	**Secondary**			BOE
Mold	**0.080**		a	Mold	0.050		a
Manufacturing	0.100	mm rms	b	Manufacturing	0.035	mm rms	b
Gravitational	0.042	mm rms	c	Gravitational	0.020	mm rms	c
Wind	0.010	mm rms	c	Wind	0.010	mm rms	c
Thermal	0.050	mm rms	c	Thermal	0.010	mm rms	c
Ageing	0.014		a	Ageing	0.007		a
Total	0.145	mm rms		Total	0.066	mm rms	
Combined Total (RSS)		**0.159**	mm rms				
Frequency (GHz)	**2**	**10**	**30**	**80**	**100**	**116**	
Surface eff	100.0%	99.6%	96.1%	75.2%	64.1%	54.9%	

Table 8-2 Antenna Surface Accuracy Error Budget – Normal Operating Conditions

Normal							
Wind	10	m/s	Day/night	Temperature	15	C min	
Requirement	300	micron RMS					
Primary			BOE	**Secondary**			BOE
Mold	**0.080**		a	Mold	0.050		a
Manufacturing	0.100	mm rms	b	Manufacturing	0.035	mm rms	b
Gravitational	0.042	mm rms	c	Gravitational	0.020	mm rms	c
Wind	0.020	mm rms	c	Wind	0.020	mm rms	c
Thermal	0.080	mm rms	c	Thermal	0.050	mm rms	c
Ageing	0.016		a	Ageing	0.008		a
Total	0.159	mm rms		Total	0.084	mm rms	
Combined Total (RSS)		**0.180**	mm rms				
Frequency (GHz)	**2**	**10**	**30**	**80**	**100**	**116**	
Surface eff	100.0%	99.4%	95.0%	69.5%	56.7%	46.5%	

8.2 Pointing Error Budget

Pointing error is defined as the angular difference between the commanded antenna pointing direction and the resulting main lobe peak gain. Pointing error specifications are for different operating conditions (precision or normal) and whether the pointing currently falls within an angular offset and time offset of a calibration source location that is suitable for a pointing error measurement. The specifications are shown in Table 9-7 and Table 9-8.

Pointing error can be repeatable or non-repeatable. Repeatable pointing error can be compensated to some degree. Residual error or error introduced by compensations are treated as non-repeatable pointing error in this document. Systematic pointing errors due to mechanical misalignments and gravity are compensated by using a systematic pointing error correction model (SPEM) as the basis of a compensation. The SPEM model coefficients are determined from a least squares determination according to measurements of pointing error from calibration sources. Other means of correcting systematic pointing error include atmospheric refraction correction, tiltmeters, temperature measurements, and antenna modelling for strain induced by gravity, wind, and thermal effects.

The pointing error budget identifies sources of pointing error in the bias (systematic) and random categories, allocates error amounts to the different sources, and defines the calculation of total pointing error from the allocated amounts. The budget is used both to determine compliance with the specifications when the achievable pointing error contribution for each source is known or estimated, and to determine the available error margin in a source using the allowed total pointing error from the specification.

An example pointing error budget from ngVLA 18 m antenna is shown in Table 8-3. Both elevation and cross-elevation (XEL) errors are included. Each error is given for absolute pointing (pointing directly to a commanded direction) with and without compensation, and for referenced pointing (pointing relative to a well-known pointing “landmark”) as an applicable fraction of the absolute pointing error contribution. Contributions are divided into categories as they apply to the major components of the antenna system (elevation assembly, pedestal, servo system, and foundation). Examples of error sources include errors in alignment and perpendicularity of the antenna components and deformation by gravity, wind, and thermal expansion/contraction.

Table 8-3 Example Pointing Error Budget from 18m

Precision Operating Environment **Elevation angle;** **66** Degrees

Wind Speed [m/s]	Equivalent Wind Speed w/Gusts [m/s]	Max Wind Gust Speed [m/s]	Thermal Soak [C]	Thermal Gradient [dT]	Thermal Change [C/hr]
5	5.3	7	20	0	1.8

PE Contributor	Elevation PE Without Compensation (arcsec)	Elevation PE With Compensation (arcsec)	Elevation Applicabilty to Referenced Pointing (%)	Referenced El Pointing Error (arcsec)	XEL PE Without Compensation (arcsec)	XEL PE With Compensation (arcsec)	XEL Applicabilty to Referenced Pointing (%)	Referenced XEL Pointing Error (arcsec)	BOE	Notes
Structure Deformation Due to Gravity	86.40	0.00	100%	0.00	0.00	0.00	100%	0.00	b	Compensated by SPEM
Structure Deformation Due to Thermal Soak	11.00	11.00	10%	1.10	0.00	0.00	10%	0.00	b	Very slow change, assumed 100% compensated in Reference Pointing
Structure Deformation Due to Thermal Gradient	0.00	0.00	50%	0.00	0.00	0.00	50%	0.00	b	Slow change, assumed 75% compensated in Reference Pointing
Structure Deformation Due to Constant Wind	2.00	2.00	50%	1.00	0.00	0.00	25%	0.00	b	Moderate change, assumed 50% compensated in Reference Pointing
Structure Deformation Due to Wind Gusts	0.25	0.25	100%	0.25	0.00	0.00	100%	0.00	c	
Subtotals (RSS + Wind)	97.63	11.23		1.66	0.00	0.00		0.00		
Elevation Assembly										
Orthogonality error, Reflectors to Elevation Axis	10.00	0.00	100%	0.00	10.00	0.00	100%	0.00	a	Compensated by SPEM
Pedestal										
Tower Tilt Fixed	1.00	0.00	100%	0.00	1.00	0.00	100%	0.00	a	Compensated by SPEM
Othogonality of the Az/El Axes	4.00	0.00	100%	0.00	4.00	0.00	100%	0.00	a	Compensated by SPEM
Subtotals	4.12	0.00		0.00	4.12	0.00		0.00		
Servo										
Encoder Mounting and Gearing With Temp.	1.00	0.00	100%	0.00	1.00	0.00	100%	0.00	a	Compensated by SPEM
Encoder Calibration error or Fixed Offsets	2.00	0.00	100%	0.00	2.00	0.00	100%	0.00	a	Compensated by SPEM
Wind Gusts	0.59	0.59	100%	0.59	0.00	0.00	100%	0.00	d	
Subtotals (RSS + Wind)	2.31	0.59		0.59	2.24	0.00		0.00		
Foundation										
Foundation change (long-term)	1.00	0.00	0%	0.00	1.00	0.00	0%	0.00	a	Compensated by SPEM
Foundation deformation with Constant Wind	0.50	0.50	50%	0.25	0.50	0.50	50%	0.25	a	Moderate change, assumed 50% compensated in Reference Pointing
Foundation deformation with Wind Gusts	0.48	0.48	100%	0.48	0.06	0.06	100%	0.06	c	
Subtotals (RSS + Wind)	1.40	0.98		0.73	1.15	0.56		0.31		
SPEM Residuals										
SPEM Residuals	0.50	0.50	25%	0.13	0.50	0.50	25%	0.13	a	
Totals and Comparison With Specification										
Total PE (RSS + Wind)	97.75	11.30		1.91	4.85	0.75		0.34		

Total El and XEL Compensated PE (RSS'd)	**11.32**
Non-Repeatable Pointing Error Spec. (arcsec)	18.00
Total EL and XEL Referenced Pointing Error	**1.94**
Referenced Pointing Error Specification	3.00

9 PERFORMANCE

9.1 Aperture Efficiency

The key requirements for aperture efficiency relate to surface accuracy and reflector surface continuity, Table 9-1.

Table 9-1 Aperture Efficiency Related Requirements [AD01]

Parameter	Req. #	Value	Traceability
Surface Accuracy, Precision	SBA0501	Surface errors shall not exceed 160 μm RMS, for the primary and secondary reflector combined when operating in the Precision operating environment.	SYS0501
Surface Accuracy, Normal	SBA0502	Surface errors shall not exceed 300 μm RMS, for the primary and secondary reflector combined, when operating in the Normal operating environment.	SYS0501
Reflector Construction	SBA0503	Each reflector may be constructed as a single piece or as multiple panels. If constructed of multiple panels, gaps between panel edges shall not exceed 1 mm.	

9.1.1 Primary Reflector Surface Deformation

Surface deformation due to gravitational and thermal load cases are discussed in this section. Surface deformation results are obtained using Finite element analysis (FEA) of dish structure without the mount and pedestal (discrete dish model) in the first phase. The FEA data are then processed through a routine that calculates the rigid body motions and the residual error on the surface after rigid body motion correction. The secondary reflector and the receiver were modelled as lumped mass in the preliminary results while the secondary support structures were modelled as 1D elements. In the second phase the mount, pedestal, secondary reflector and the support structures were integrated with the primary reflector model. At the time of writing, work on the integrated model had just begun so this report focuses on the primary reflector and effects of various gravity cases and temperature variation.

The following table will present the FEA parameters of the model.

Table 9-2 FEA parameters

Parameter	Comment
Elevation axis	y-axis
Constraints	1. x and z translation at the elevation mount 2. tangential at the drive arc
Tubes	CROD and CBEAM
Secondary + receiver	Lumped mass
Secondary support structure	CBEAM
Secondary + receiver mass	900 kg
Counterweight	350 kg
Gravity load cases	15° and 90°
Temperature change	20°C

9.1.1.1 Gravitational distortion (Discrete model)

In the discrete model, incremental changes at different stages helped to reduce the primary surface error from 70 micron to 37 micron. Also, the errors at 15 degrees are always lower than errors at 90 degrees therefore only the 90 degree cases have been considered in most of the iterations. Natural frequency was also obtained at every iteration. The following table presents a few major landmarks in the development.

Table 9-3 Surface RMS errors summary

Design iteration	Changes made	Surface RMS error at 90 degrees [μm]	Natural frequency, [Hz]
00	Baseline	78	
01	Reinforced sections	69.5	3.305
02	Soft connection at the elevation support hinge	49.6	3.337
03	Double hinge	36.9	3.65

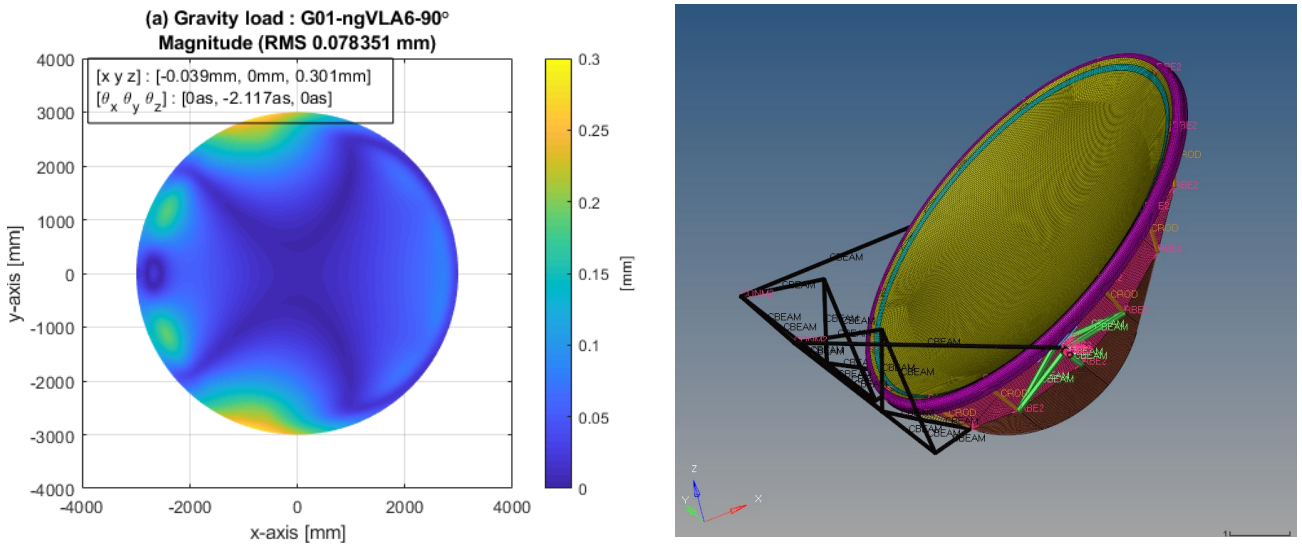

Figure 9-1 Design iteration 00 (90 degrees)

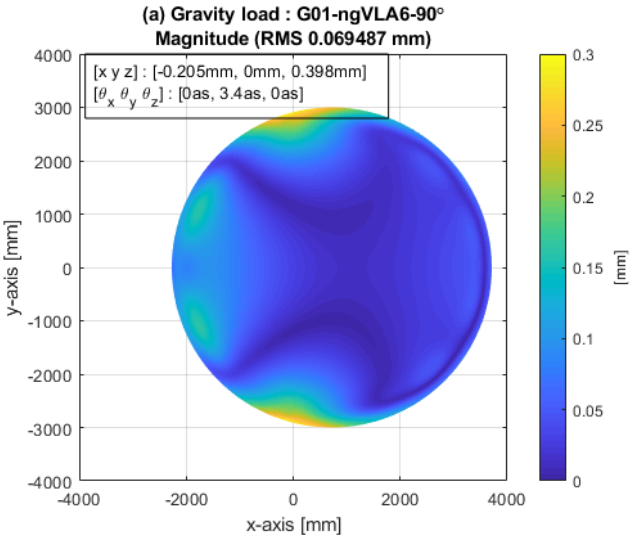

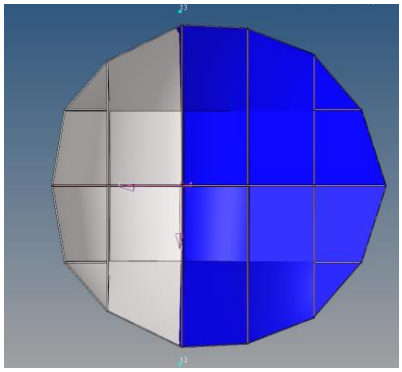

Stiffening the BUS structure (white color) improves the surface RMS error by ~11%

Figure 9-2 Design iteration 01 (90 degrees)

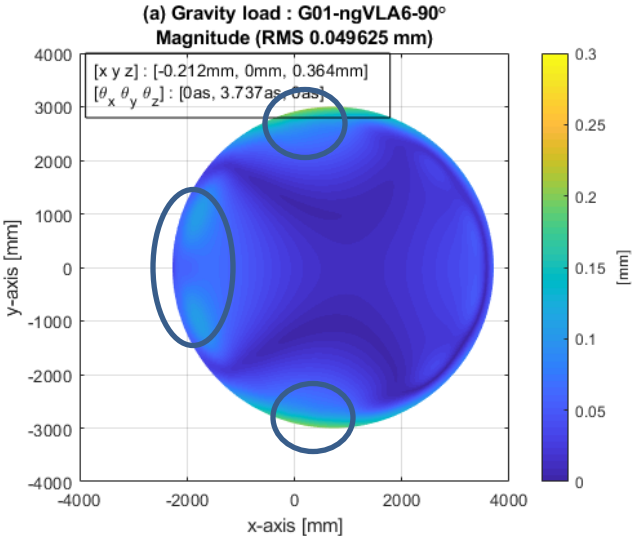

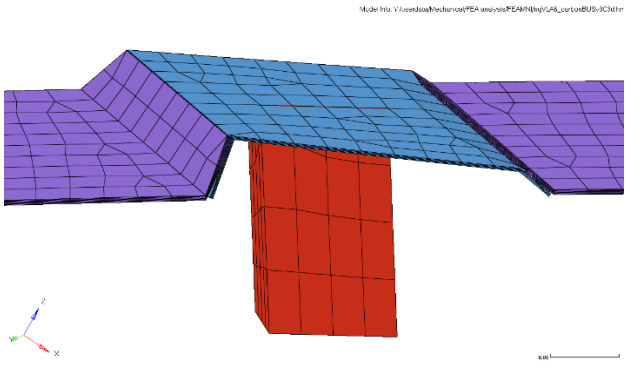

Soft connection was introduced by changing the laminate thickness to remove the hard points around elevation axis and the secondary feed le connections. This is done only at 5 locations.

Figure 9-3 Design Iteration 02 (90 degrees)

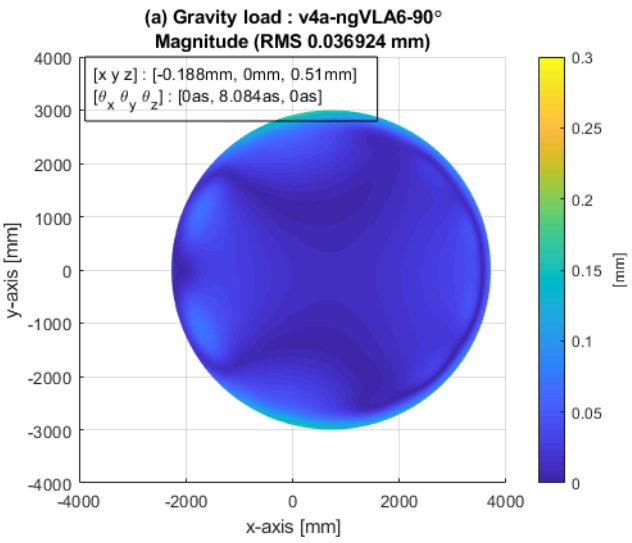

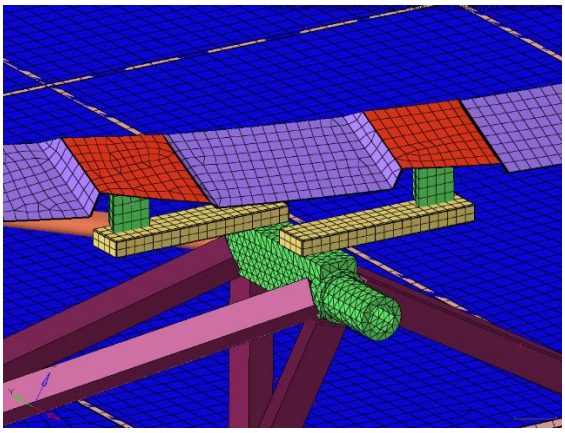

Double hinge was introduced to provide better shear connection and distribute the load more evenly

Figure 9-4 Design Iteration 03 (90 degrees)

The surface deviation at 15 degrees (design iteration 03) was obtained at 34.1 micron (**Figure 9-5**).

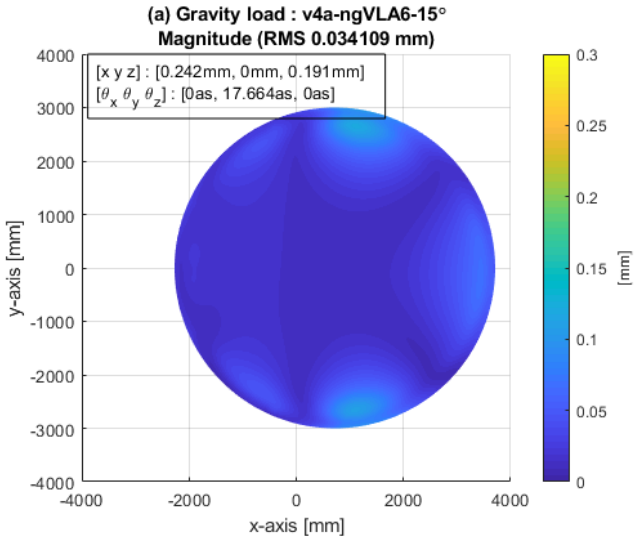

Figure 9-5 Design Iteration 03 (15 degrees)

9.1.1.2 Gravitational distortion (Integrated model)

The mount, pedestal, secondary reflector and the support structures were integrated with the primary reflector model. The azimuth bearing is modelled as spring element (CBUSH) with stiffness values at different DOFs provided by Sightline Engineering. The secondary support structure is also modelled with the receiver load. The secondary dish and support structure has yet to be optimized for local distortions.

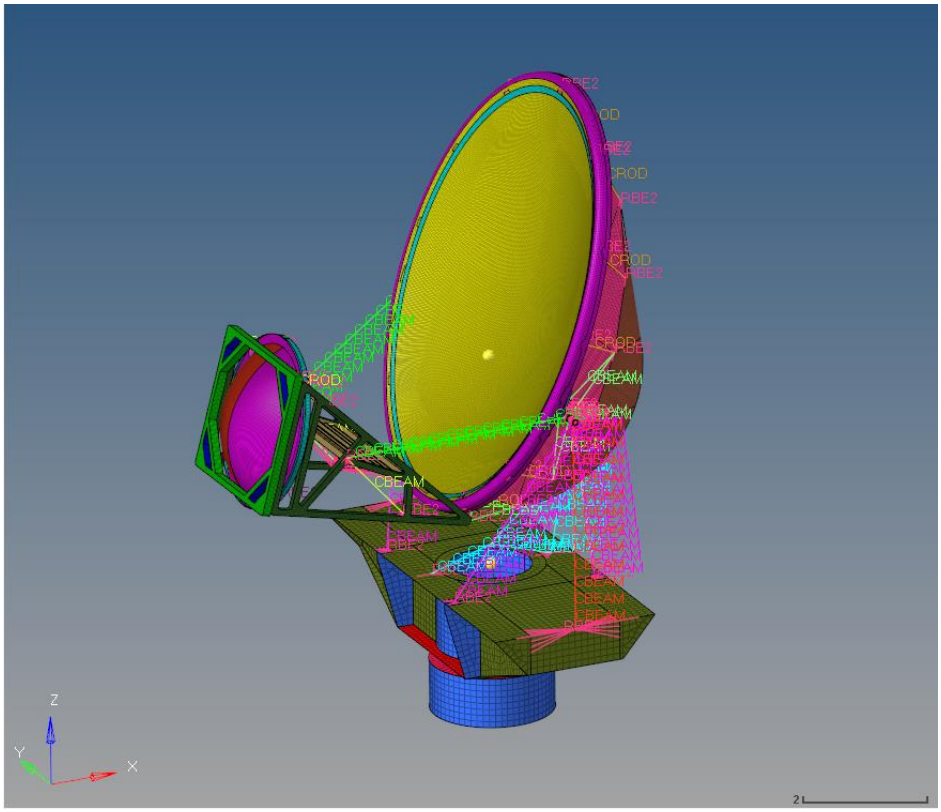

Figure 9-6 Integrated FEA model of the 6m dish (53 degrees elevation angle)

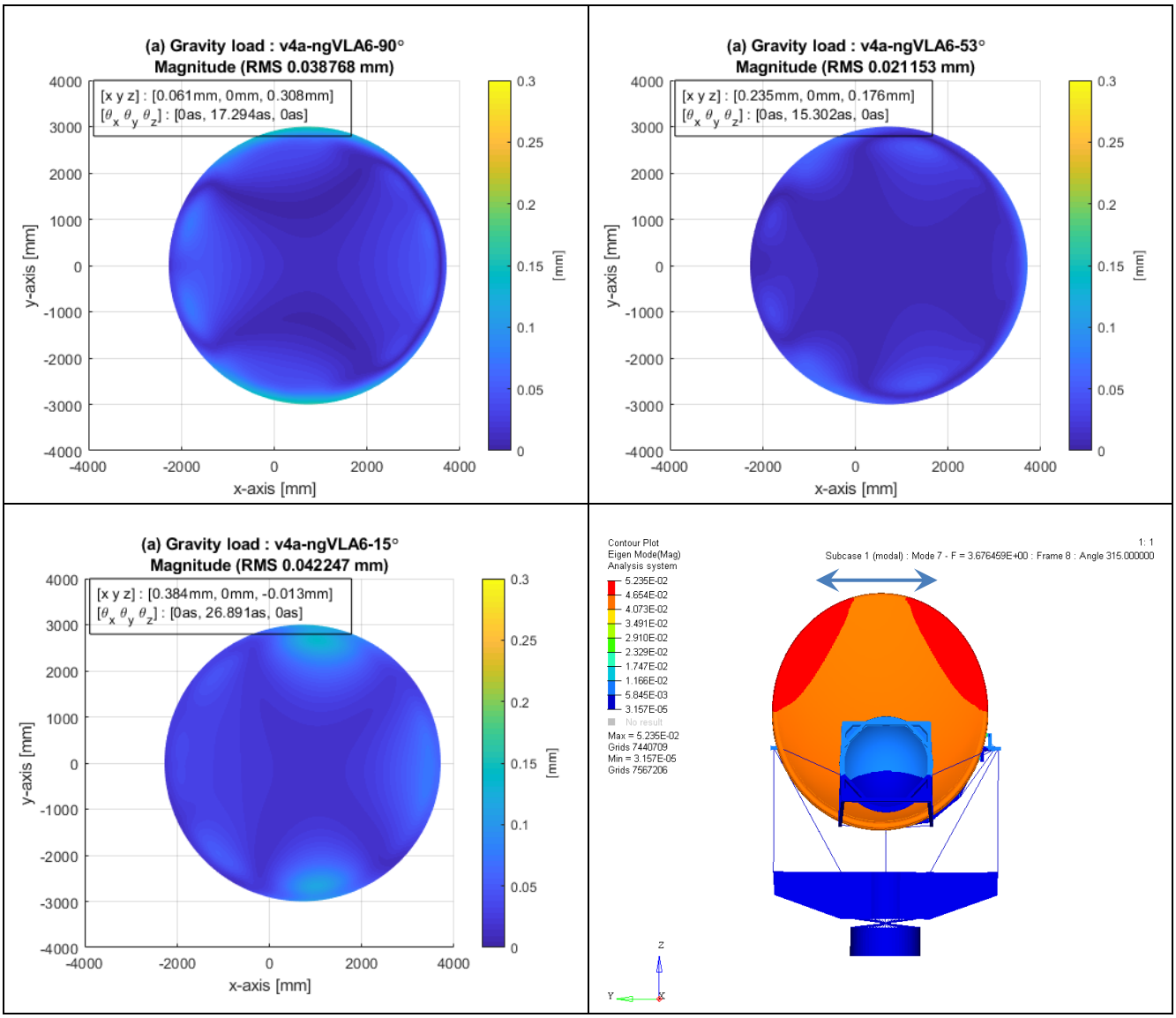

Figure 9-7 Primary surface deviation results from the integrated model

- The 90 degree case is not affected by the integration of the mount and secondary and support structure.
- The 15 degree case is affected after the integration, it is expected that the mount stiffness will only add the solid body rotation and translation so the surface distortion may due to the larger moment imparted on the primary by the secondary and support structure.
- The approximate rigging angle was obtained near the middle of the elevation range (53 degrees). The error is 21 micron.

- It is planned to obtain the surface accuracy vs elevation angle plot to find the true rigging angle.
- The 1st mode is the primary reflector surface oscilating lateraly on the OBUS tubes at a frequency of 3.67 Hz at 53 degree elevation angle.

9.1.1.3 Update on the Gravity induced Surface distortion (Integrated model)

There are a few changes occurred in the updated FEA analysis. They are listed below:

1. The placement of the primary BUS tube locations are changed. Please see section 4.1.1 and 4.1.2
2. The hinge type support mentioned in **Figure 9-4** is replaced with regular tube connections
3. The mount is updated to the latest version designed by Sightline Engineering.
4. The BUS Tub laminate schedule is optimized as shown in **Figure 9-8.**
5. The tubes are optimized for gravity (self-weight of the tubes) and presented in **Figure 9-9.**
6. The secondary mass has been changed to 900 kg to include the indexer, support structures and feed weights
7. The secondary reflector support structures are optimized
8. The secondary reflector rim and backing pieces are optimized

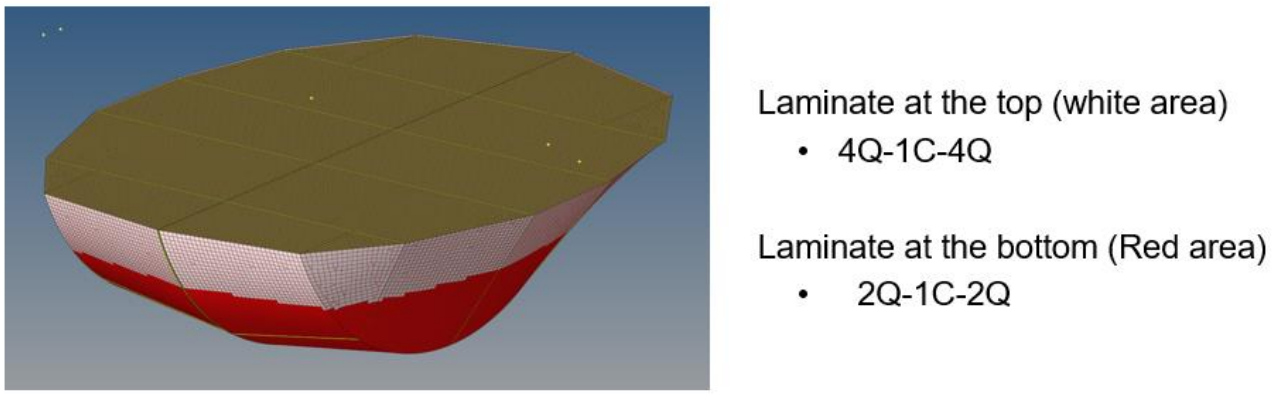

Figure 9-8 Laminate schedule of the BUS Tub (Q= QISO, C=Core)

The worst case gravity induced primary surface distortion is 42 μm at 90° elevation angle. **Figure 9-10** presents the errors at different elevation angles. At 90° elevation, the whole dish sags down while at 15° elevation, the dish tilts forwards which creates some localized distortions at the primary surface near the elevation axis. At 53° elevation, least surface distortion is observed. Secondary surface distortion results are presented in section 9.1.2.

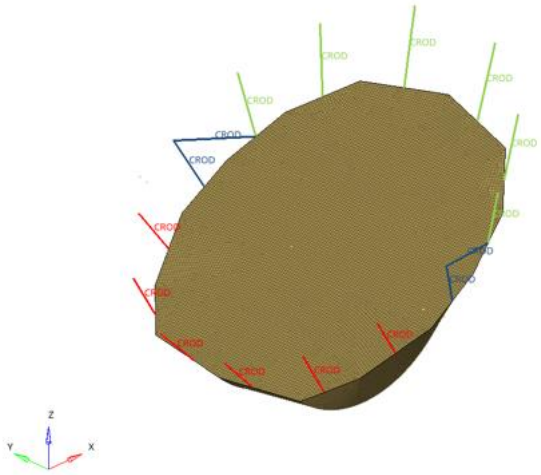

- Green – Carbon tubes – 175 GPa
- Blue tubes – Steel tubes
- Red tubes – Steel tubes
- Tube cross section – OD 100 T6.35 mm
- Further optimization is possible

Figure 9-9 Optimized OBUS tubes

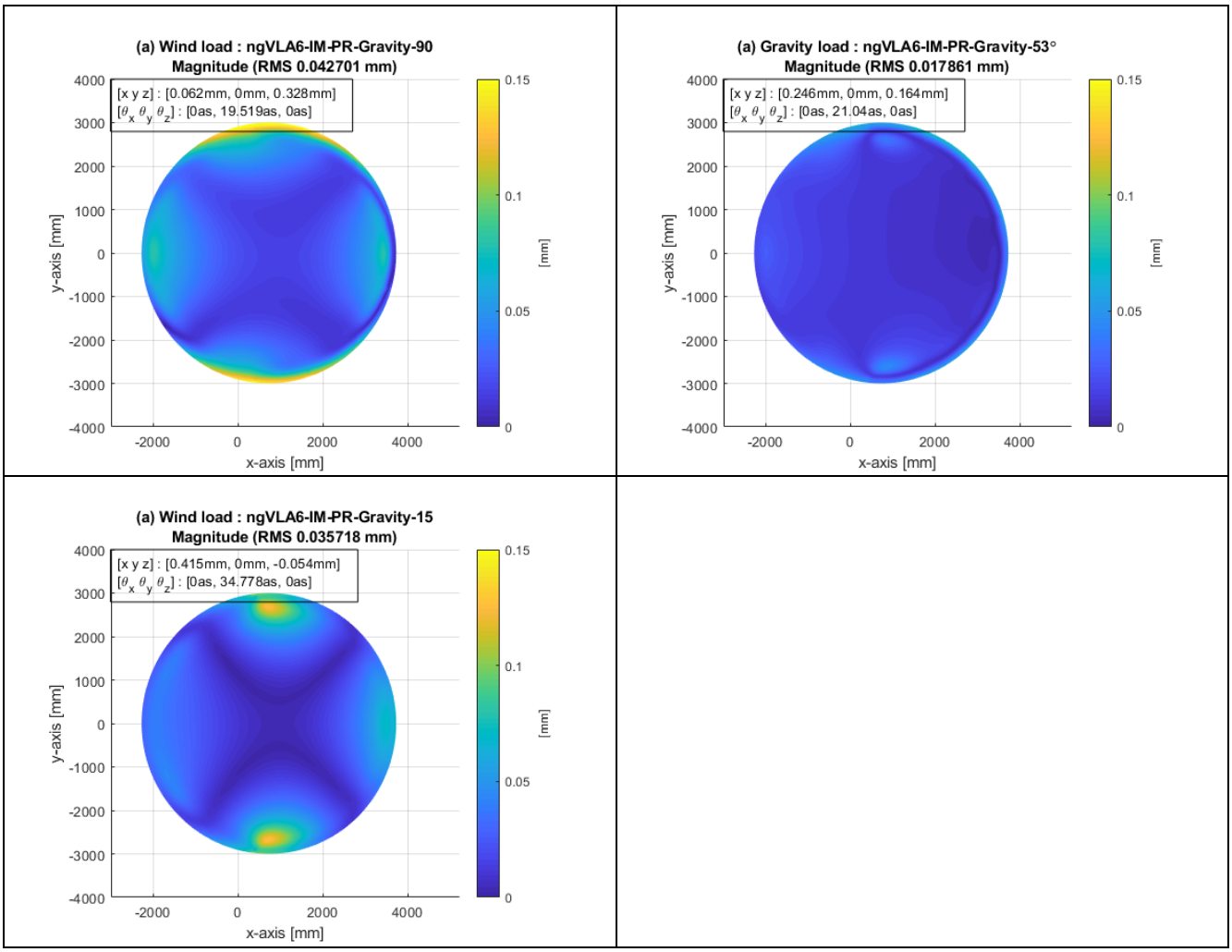

Figure 9-10 (Updated) Primary surface deviation results from the integrated model (upper left) at 90° elevation angle error is 43 μm, (upper right) 53° elevation angle error is 17 μm, (lower left) 15° elevation angle error is 37 μm

9.1.1.4 Thermal distortion (Discrete model), earlier version

Thermal bath analysis was also performed on the discrete model. The ΔT was set at 20°C. **Figure 9-11** presents the distortion due to temperature change. The OBUS steel tubes expand differently due to differences in length (tubes close to secondary are shorter than the ones far from the secondary), Figure 9-12.

NB: the undistorted surface is scaled with an effective CTE scaling factor of 3.78e-6 m/m/°C.

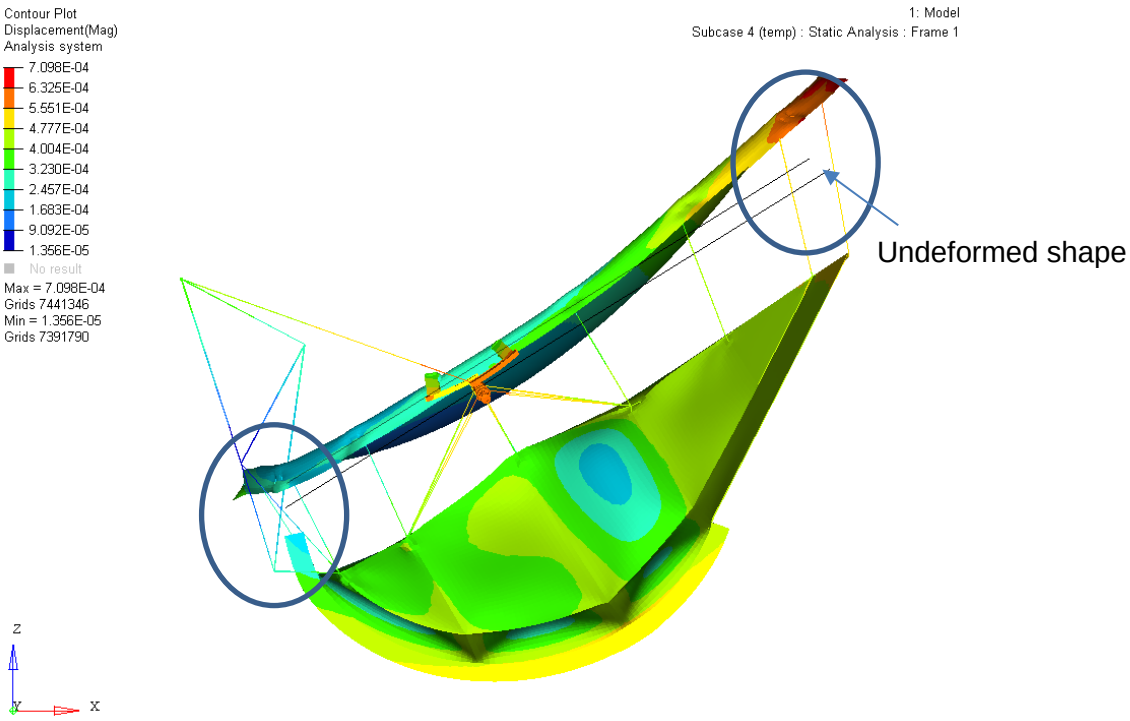

Figure 9-11 Distortion in the dish due to temperature change ($\Delta T = 20°$) all steel OBUS tubes (1500X magnification**)**

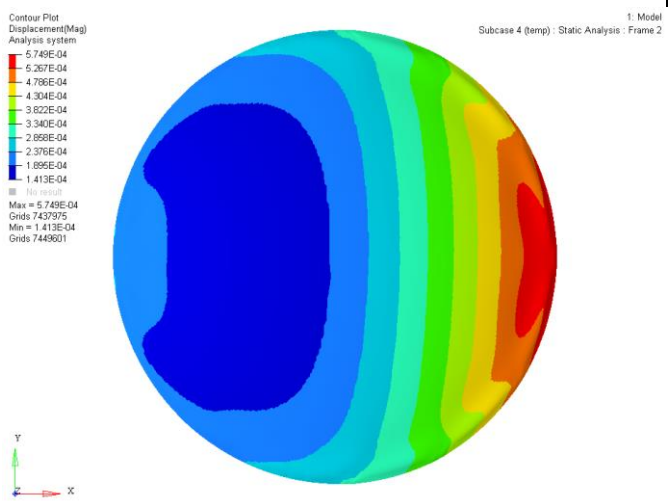

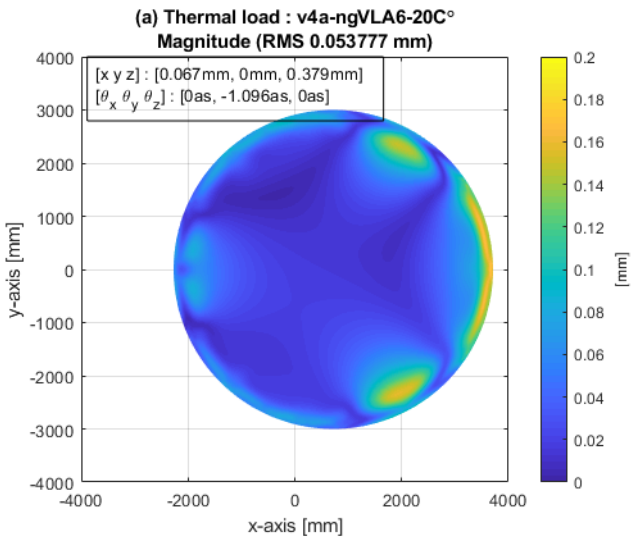

Figure 9-12 (Left) FEA results (Right) Surface distortion analysis all steel OBUS tubes.

Since there is a differential change in length at the OBUS tubes, it is necessary to match the CTE for some of the OBUS tubes. **Figure 9-13** shows the OBUS steels tubes which are replaced with Carbon tubes for CTE matching.

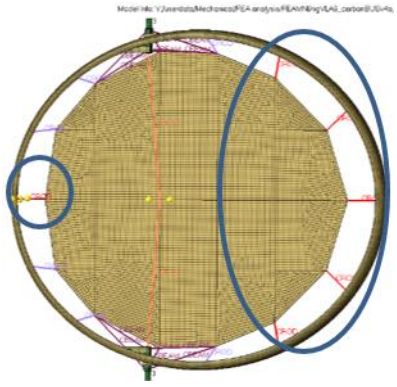

Figure 9-13 CTE matched OBUS tube orientation

The FEA results of CTE matched OBUS tubes are presented in **Figure 9-14**, it can been seen that the shape of the dish does not distort at the ends.

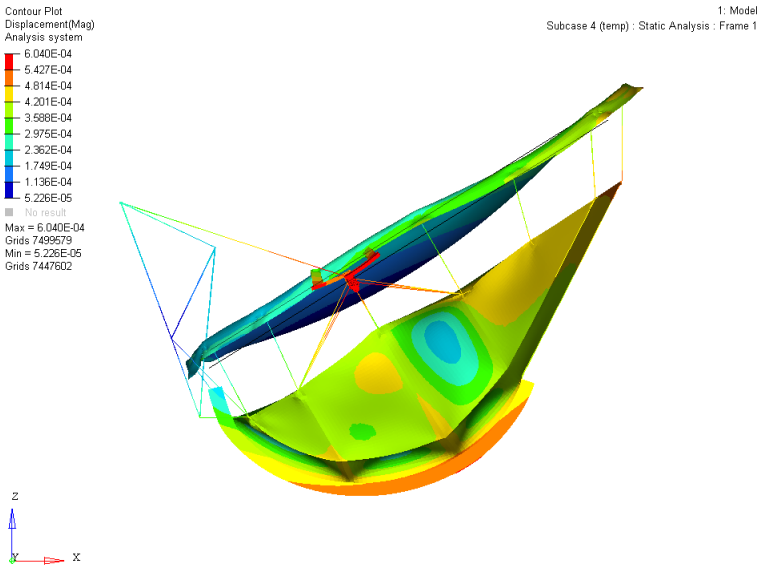

Figure 9-14 Distortion in the dish due to temperature change ($\Delta T = 20°$) mix of carbon and steel OBUS tubes (1500X magnification**)**

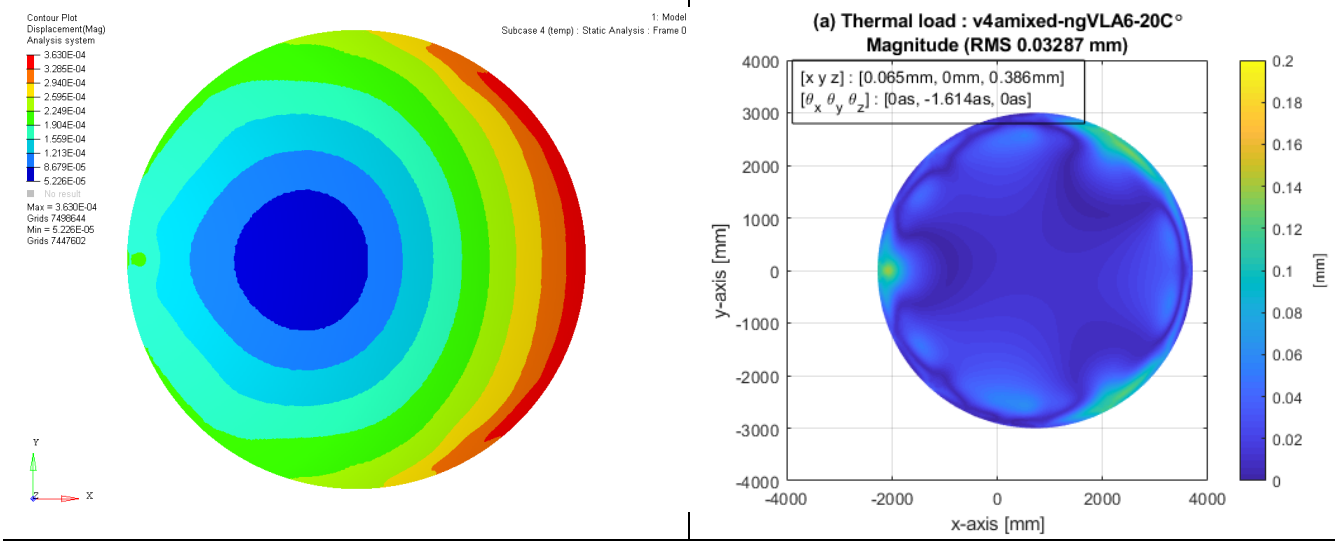

Figure 9-15 (Left) FEA results (Right) Surface distortion analysis, mix of carbon and steel OBUS tubes.

Thermal analysis results are listed in the Table 9-4.

Table 9-4 Surface RMS error reduction in Thermal loading

Iterations	Errors [μm]	Natural Frequency [Hz]	Notes
Steel OBUS tubes	53.8	3.54	
CTE matched OBUS tubes	32.9	3.7	Figure 9-13

9.1.1.5 Update on the Temperature induced Surface distortion (Integrated model)

The primary reflector consists of different composite parts which has different CTEs which creates temperature induced surface distortion presented in Figure 9-16. Since the overall surface expands due to the temperature loading, the undistorted point clouds are scaled by a factor equivalent to the effective CTE of the whole structure. The value was used 6.75 e-6 m/m/°C which is close to the reflector CTE value.

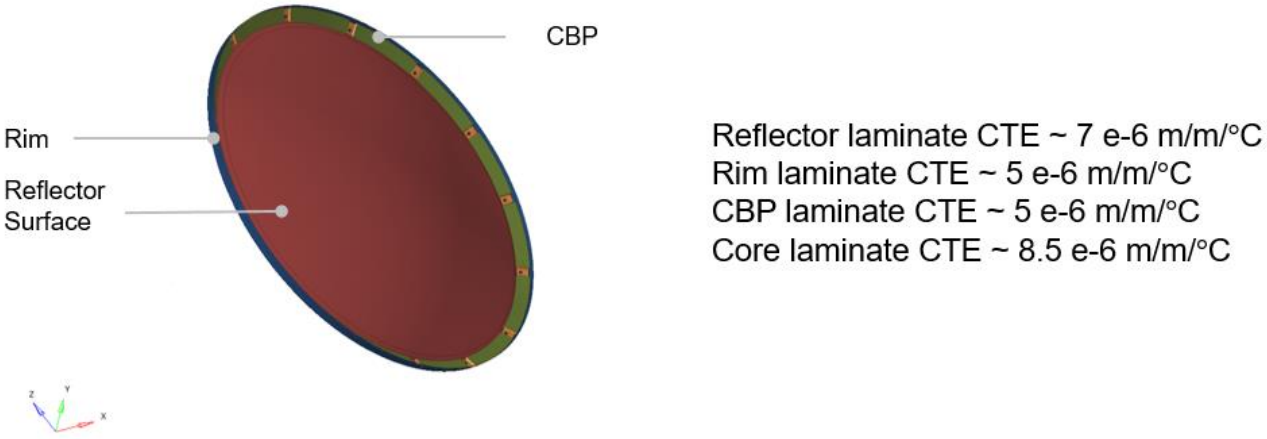

Figure 9-16 CTE variation among the parts in the primary reflector

The Finite element analysis under the thermal bath of 20°C is shown in Figure 9-17. The constraint point in the drive section varies depending on the elevation angle and affects the surface distortion presented in Figure 9-18.

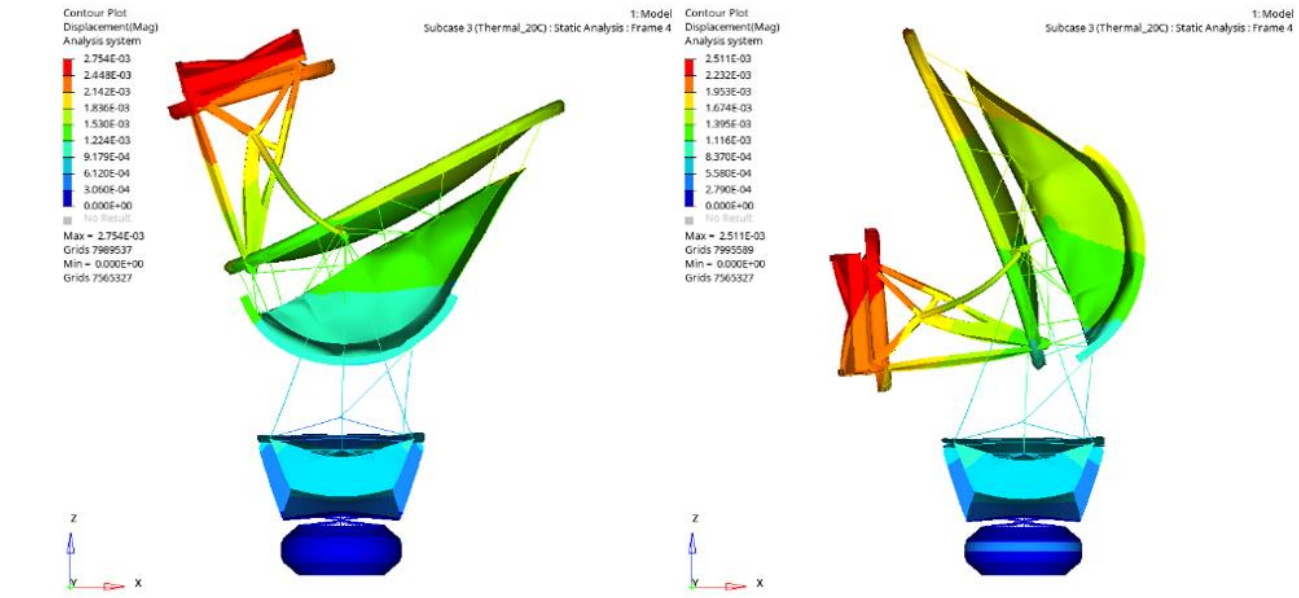

Figure 9-17 Displacement in the dish structure due to the thermal bath (left) at 90°elevation, (right) 15° elevation

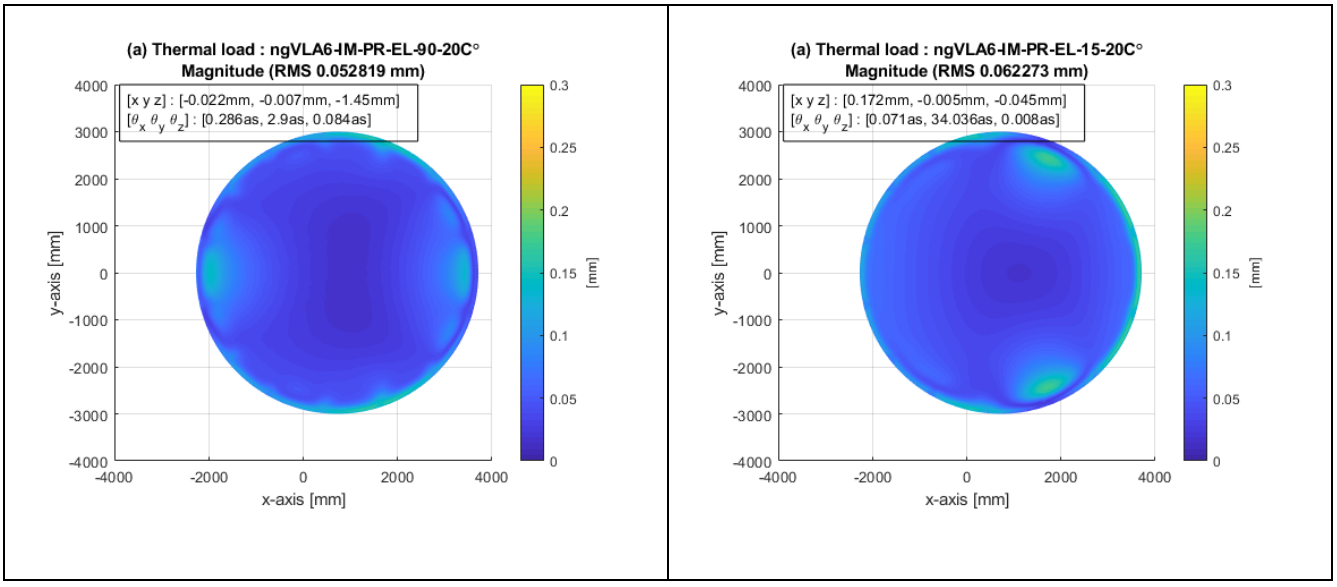

Figure 9-18 Primary Surface distortion due to the thermal bath (left) at 90°elevation error is 53 μm, (right) 15° elevation error is 52 μm

Figure 9-18 presents the temperature induced surface distortion. Although these errors are not true errors (due to scaling), they provide good representation of the errors. Based on the previous iterations and Table 9-4, some further optimization has been done on the tube tubes to match the CTE. Figure 9-19 presents the CTE matching of the OBUS tubes to minimize the surface distortion. In Figure 9-20, temperature induced surface distortion is presented for the CTE matched OBUS tubes where the surface error is reduced by 22% for the worst case elevation angle.

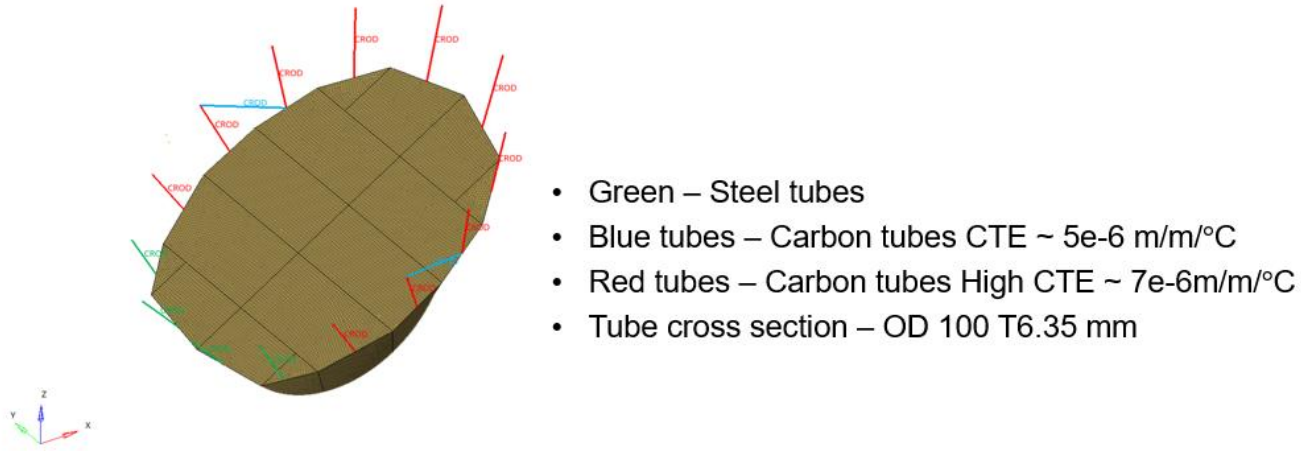

Figure 9-19 CTE matching of the OBUS tubes

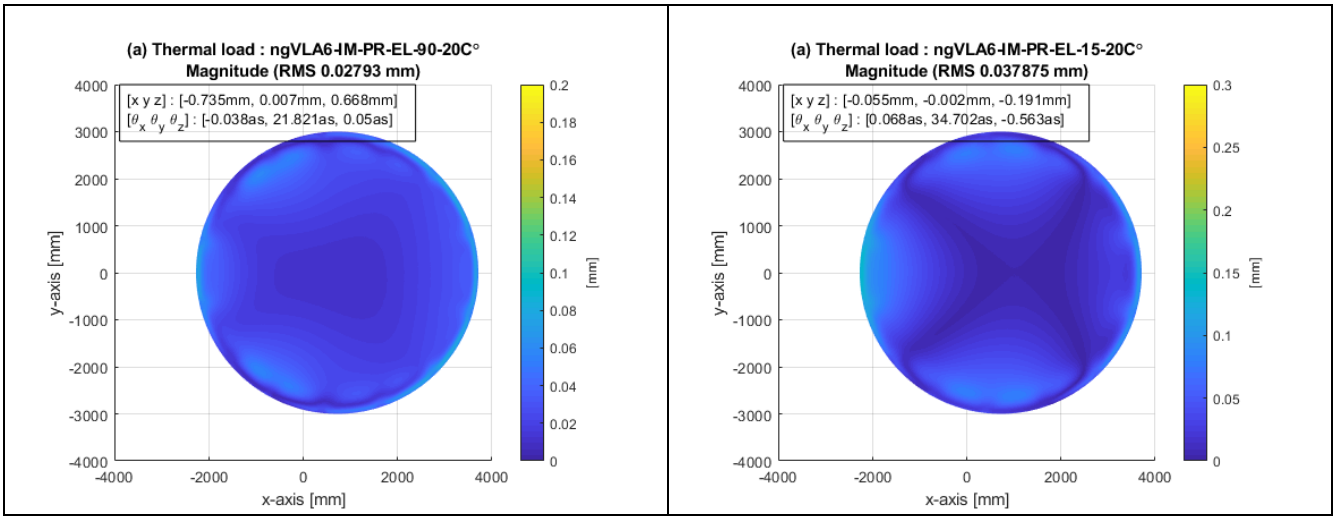

Figure 9-20 Primary Surface distortion due to the thermal bath (left) at 90°elevation, (right) 15° elevation – CTE matched tubes

9.1.1.6 Normal modes analysis

Normal modes are analysed for the integrated model. The first mode has 1.7 Hz which is low. Figure 9-21 presents the first 4 modes. From normal modes analysis, it is evident that there is no lateral support between the reflector and the OBUS. So, two diagonal tubes are added shown in Figure 9-22.

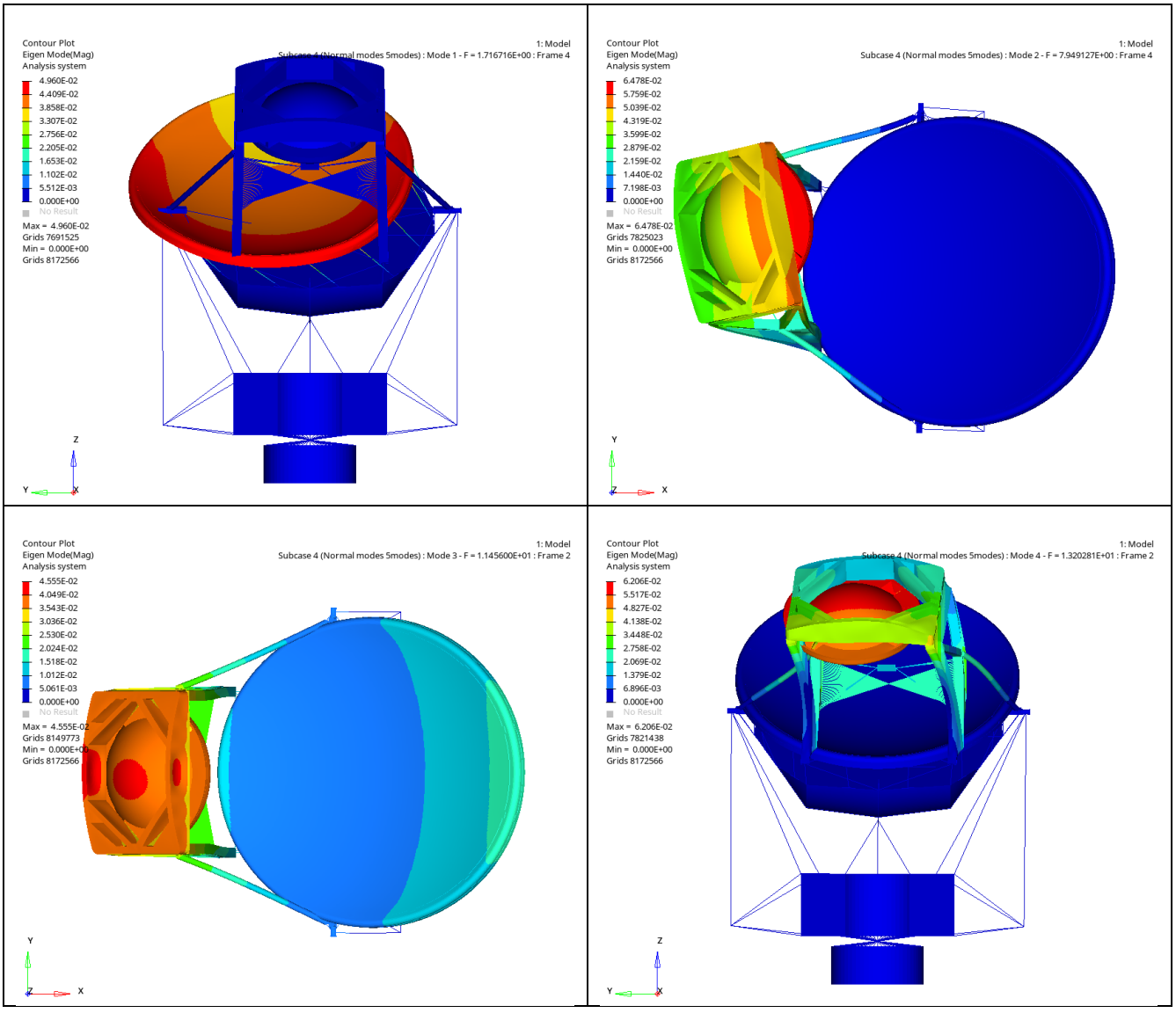

Figure 9-21 Normal modes analysis, top left – 1.7 Hz, top right – 7.9 Hz, bottom left – 11.4 Hz and bottom right – 13.2 Hz

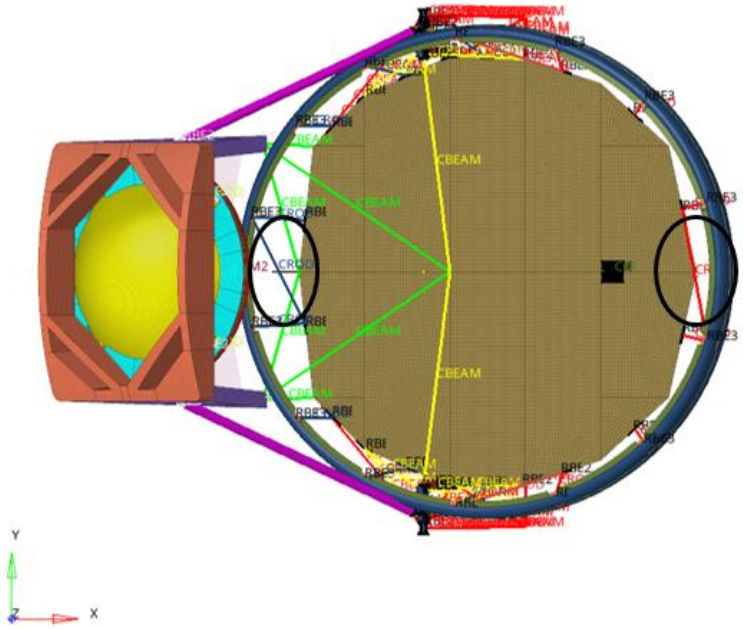

Figure 9-22 Diagonal tubes are added at the circled positions to provide lateral stiffness to the structure

With the lateral support tubes, the natural frequency is increased to 7.9 Hz (Figure 9-23).

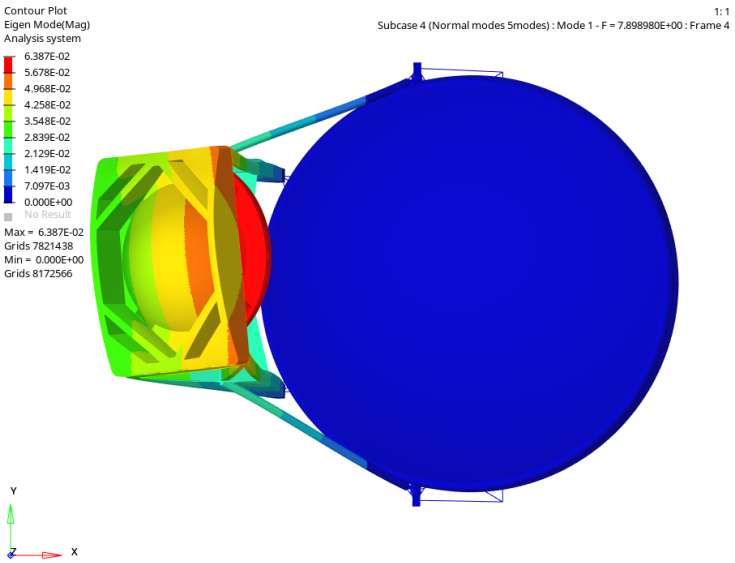

Figure 9-23 Normal modes analyses – 1st mode (7.9 Hz)

With the added lateral support, there is a concern about the thermal stresses. After thermal bath analysis, there is not noticeable difference observed with and without the lateral support ().

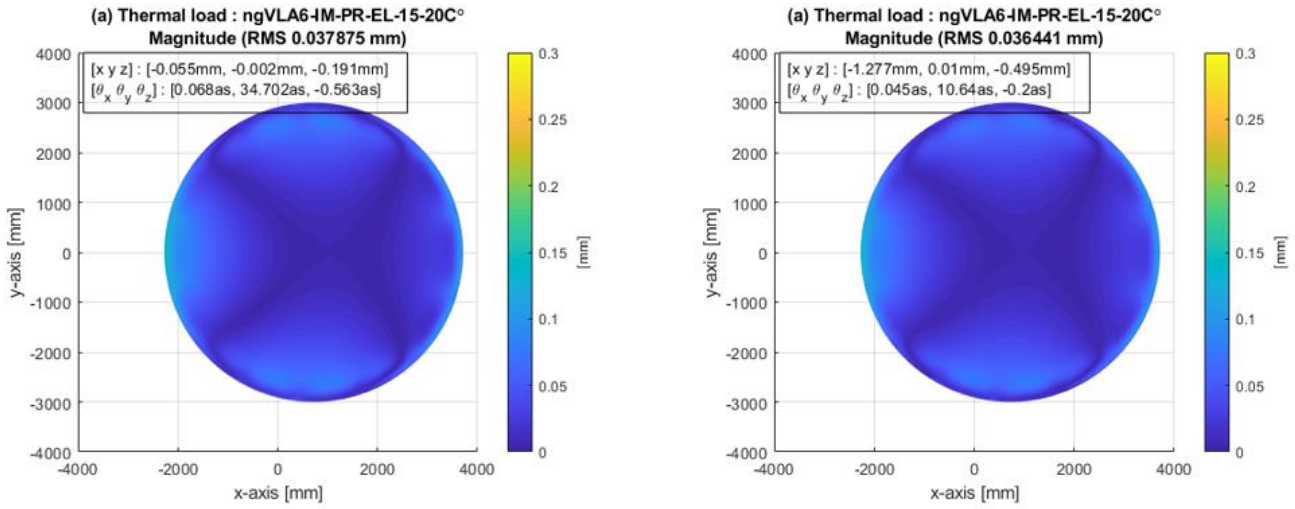

Figure 9-24 Thermal bath analysis: surface distortion (left) without the lateral support strut error is 38 μm, (right) with the lateral support strut error is 36 μm

9.1.1.7 Wind induced surface distortion

Wind tunnel test results are presented in Figure 9-25. Based on the maximum and the minimum values and the maximum standard deviation of the pressure coefficients, three cases were selected: runs 1179, 1188 and 1294. The pressure contour maps are presented in Figure 9-26. This pressure contour is mapped on the primary surface as a pressure load at 7 m/s wind velocity based on precision condition. It is expected that for the normal condition, the errors are linearly scaled and well below than the budgeted error.

	El	Az		5	6	7	8			9		10	
Max	16	0	1.033283	1.033283	0.967604	0.347073	-0.21734	0.942809	-0.26306	0.348703	-0.2268	0.366786	-0.13207
Min	66	90	-0.98448	0.027158	-0.17346	-0.9658	-0.45773	-0.22522	-0.4568	-0.98448	-0.41958	-0.96161	-0.53922
StDev	16	90	0.309534	0.190323	0.202755	0.309534	0.049911	0.214804	0.033332	0.299777	0.032348	0.30369	0.091662
Range	66	90	1.33318	1.006125	1.141067	1.312875	0.240392	1.168032	0.193745	1.33318	0.19278	1.328392	0.407158
Contour Plots			Run	1179	1185	1188	1191	1350	1359	1294	1303	1334	1343
			Azimuth	0	60	90	120	50	140	90	180	90	180
			Elevation	16	16	16	20	46	46	66	66	86	86
		X	Y	Cp	Cp	Cp	Cp	Cp	Cp	Cp	Cp	Cp	Cp
		-6.36396	-7.32282	0.17475	-0.05989	-0.22336	-0.45297	-0.1414	-0.38453	-0.11085	-0.32225	-0.10551	-0.35834
		-6.60872	-7.02459	0.175249	-0.06505	-0.22683	-0.45621	-0.18302	-0.38573	-0.12922	-0.33703	-0.1226	-0.38143
		-6.83526	-6.72636	0.179347	-0.06737	-0.22909	-0.45773	-0.2111	-0.38559	-0.14468	-0.34709	-0.136	-0.39737
		-7.04534	-6.42813	0.190743	-0.06763	-0.23	-0.45703	-0.22499	-0.38348	-0.15576	-0.35093	-0.14719	-0.40765

Figure 9-25 Wind tunnel test pressure coefficients

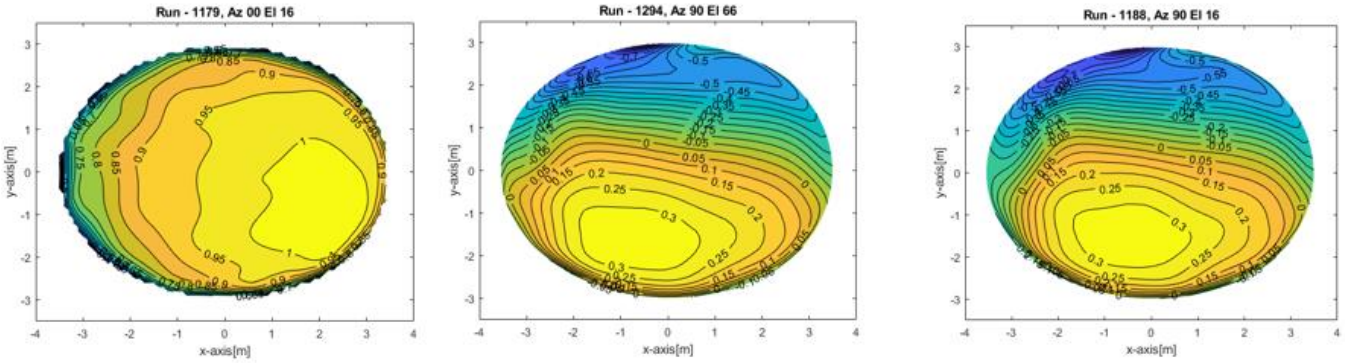

Figure 9-26 Pressure contour plot

Worst case wind induced surface distortion plot is shown in Figure 9-27. The error is observed as 9 μm. The error is other cases are less than 5 μm.

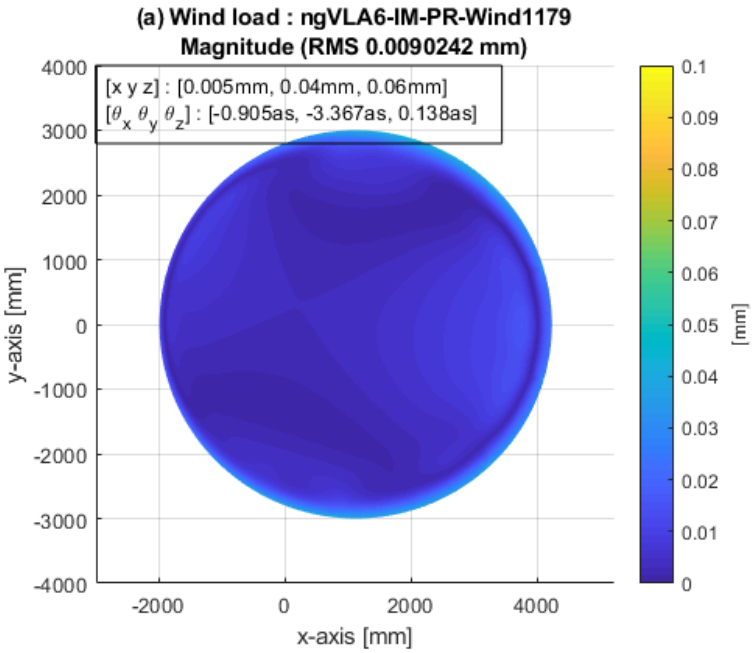

Figure 9-27 Run 1179 wind induced surface distortion error is 9 μm

9.1.2 Secondary Reflector Surface Deformation

Secondary rim design plays a significant role in secondary reflector surface distortion. This section illustrates design changes in the secondary rim geometry and finite element results under gravity and wind load cases.

9.1.2.1 Secondary reflector rim design

The secondary reflector is supported using quasi-kinematic links at four locations. The baseline design has 4 layers of QISO materials. The baseline design also has a square rim. The errors are more than 60 μm over the full range of elevation. The next iteration has slightly different layup (2 layers of QISO, 2 layers of Triaxial and 2 layers of QISO) to minimize the local distortion on the surface. Although this helps significantly, the errors are close to 40 μm where the secondary surface error is budgeted to less than 20 μm including the support structures. In the next few iterations, the rim geometry was optimized until it starts obstructing the beam. With the larger rim, internal bulkheads are required to minimize the bending of the rim. With all these implementations, the secondary reflector distortion is kept below 12 μm for all the elevations angles. **Figure 9-28** presents all the incremental changes to minimize the surface distortion error. The surface distortion plots under gravity loads (90° and 15°), constrained at quasi-kinematic supports, are shown in **Figure 9-29**.

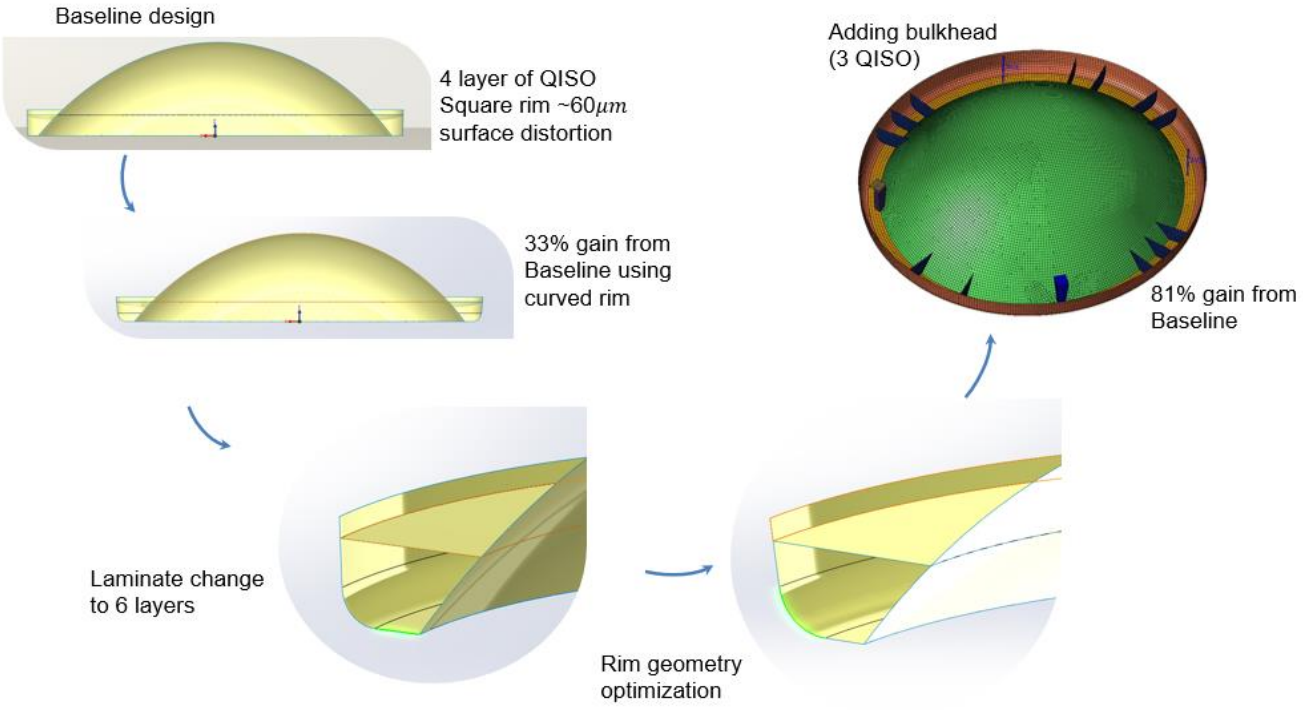

Figure 9-28 Secondary reflector development stages

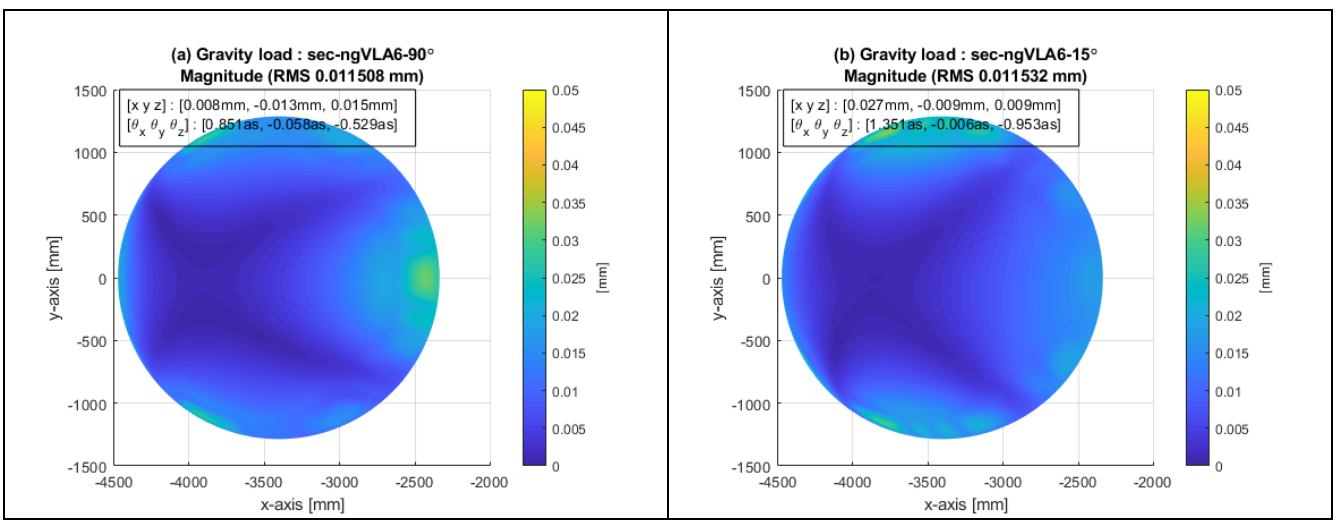

Figure 9-29 Secondary surface distortion plots (left) 90° elevation error is 12 μm (right) 15° elevation error is 12 μm

The secondary reflector support frame (square frame at the back) is changed to accommodate the larger rim and adjacent structure. The secondary support structure (side frames) is obtained through a topology optimization program. Next, the secondary reflector and the support structures are integrated with the rest of the antenna structure to analyse the gravity and temperature related distortion on the secondary reflector.

9.1.2.2 Gravity related secondary surface distortion (integrated model)

The gravity related secondary surface distortions are presented in **Figure 9-30** for the integrated model. The maximum surface distortion is observed at 15° elevation angle which is about 17μm.

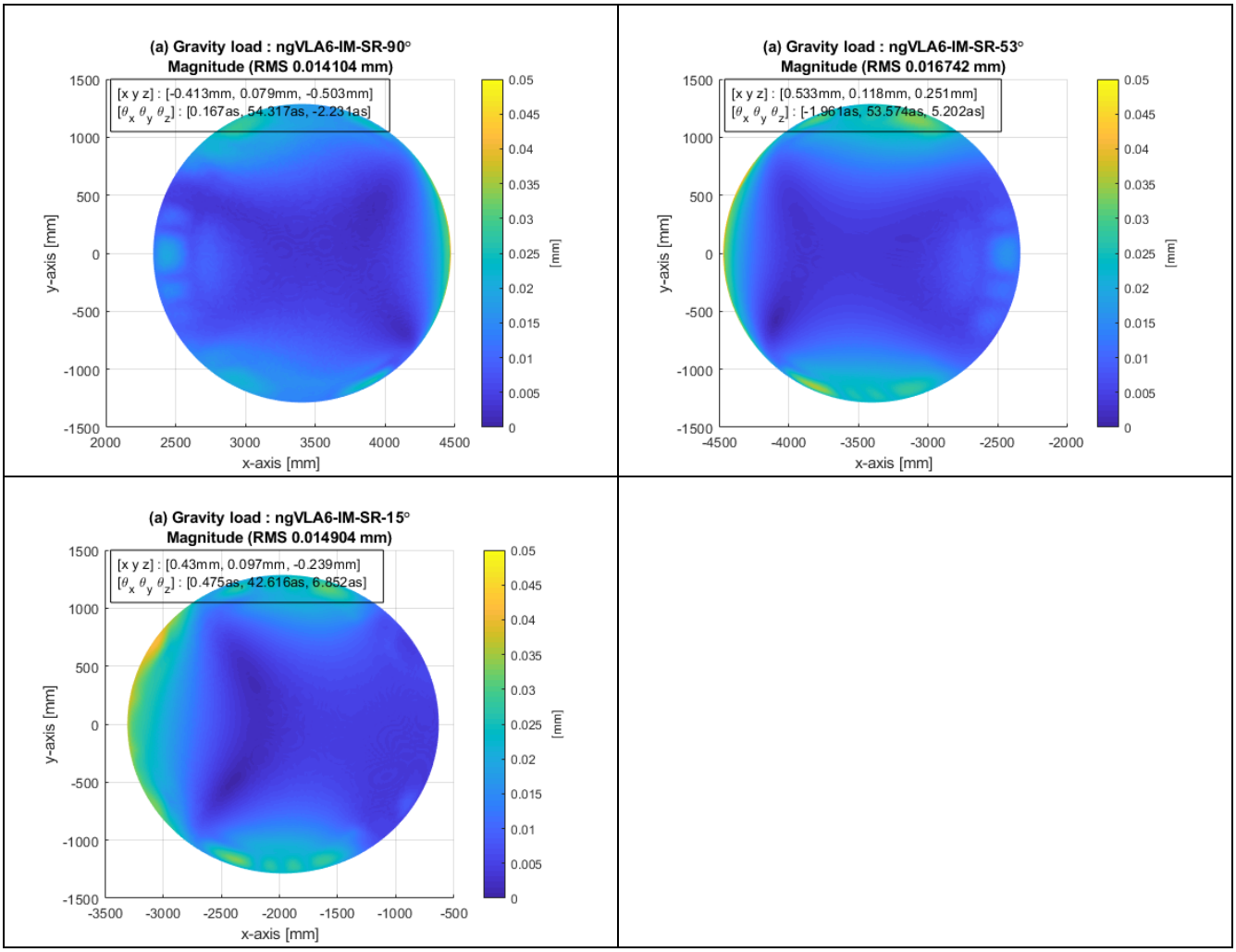

Figure 9-30 Secondary reflector surface distortion due to various elevation angles (upper left) at 90° elevation angle error is 14 μm, (upper right) 53° elevation angle error is 17 μm, (lower left) 15° elevation angle error is 15 μm

9.1.2.3 Temperature related secondary surface distortion (integrated model)

Secondary surface distortion results are presented in **Figure 9-35** under thermal bath condition. Similar scaling value is used to compute the temperature related distortion as used in the primary reflector distortion calculation. The surface distortion is less than 17 μm.

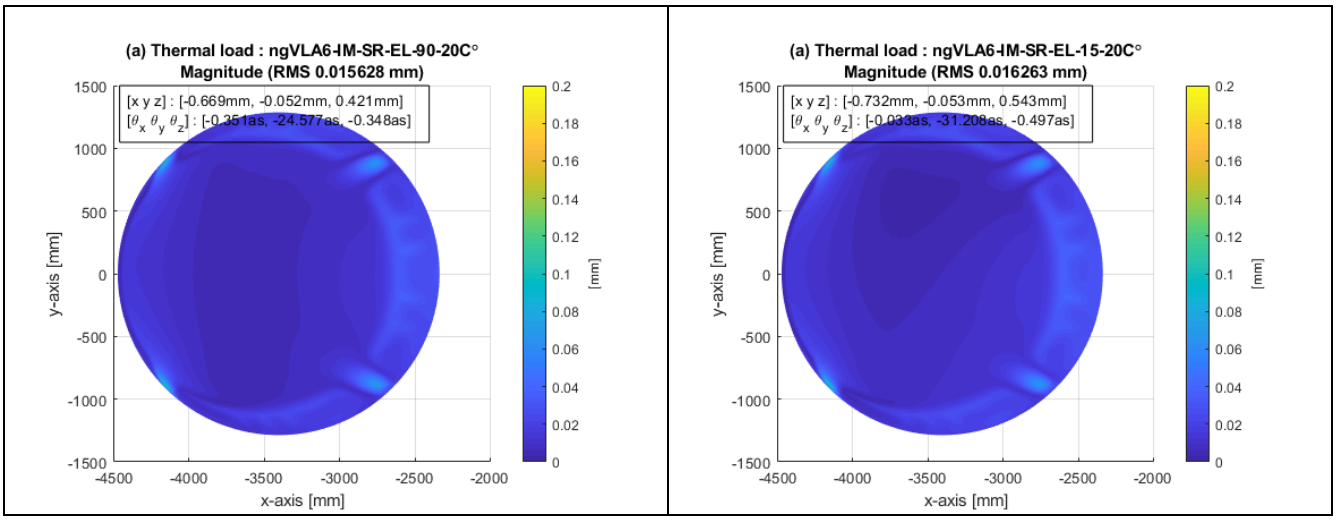

Figure 9-31 Secondary reflector surface distortion due to thermal bath of $\Delta T = 20°C$ (left) at 90° elevation angle, (right) at 15° elevation angle

9.1.3 Error summary

The surface distortion errors are summarized in Table 9-5 for all the loading conditions. The secondary surface distortion under wind load was not analysed. It is expected that the wind related distortion on the secondary surface is negligible.

Table 9-5 Error summary

Load cases	Description	Conditions	Primary Surface Error [μm]	Secondary Surface Error [μm]
LC1	Gravity load	EL 15°	37	15
LC2	Gravity load	EL 53°	21	17
LC3	Gravity load	EL 90°	34	15
LC4	Wind load – 7 m/s	AZ 0 EL 16°	9	
LC5	Wind load – 7 m/s	AZ 60° EL 16°	8	
LC6	Wind load – 7 m/s	AZ 90° EL 16°	2	
LC7	Wind load – 7 m/s	AZ 120° EL 20°	4	
LC8	Wind load – 7 m/s	AZ 90° EL 66°	1	
LC 9	Wind load – 7 m/s	AZ 90° EL 86°	2	
LC 10	Thermal Bath (Elevation 90°)	$\Delta T = 20°C$	28	16
LC 11	Thermal Bath (Elevation 15°)	$\Delta T = 20°C$	38	16

9.1.4 Manufacturing Errors

The SRC reflectors are manufactured as the name implies in one piece on a mould. The as-manufactured surface accuracy depends on; mould accuracy, process design and process control. As illustrated in the Surface Error Budget, Table 8-1, the required as-manufactured accuracy will depend on the values achieved through design for the deformation due to gravity, wind and thermal loads. The values shown in Table 8-1 represent the current status of the surface accuracy and indicate that the required as-manufactured accuracy will be ~128µm Root Mean Square (RMS) (80 microns RMS mould error and 100 microns RMS process induced error added in RSS).

9.1.5 Process Induced Distortion (PID) Study

A comprehensive study was carried out by Convergent Manufacturing Technologies to try and characterize and to quantize the PID. Generally the working method has been to estimate the PID using data collected through past experience on similar parts, however there are analytical methods that can also be used to make estimates of PID. The hope is that with a good understanding of PID, one could 'subtract out' this distortion from the mould (basically, machine in the negative of the expected distortion into the mould), and in that way this additional error term could be removed from the error table. In reality of course there will also be some scatter in the processing parameters (such as resin ratio and fibre direction) which will have some additional effect, so in reality the PID would not be completely removed.

The PID study was broken up into three main sections: Material properties characterization, L-Flange analysis, and Finite Element Modelling. The following sections outline these activities.

9.1.5.1 Material Properties Characterization

In order to model Process Induced Distortion (PID) one must know in detail all of the relevant thermal-mechanical and thermal-chemical properties that define the interaction between the resin and the fibre in the composite layup.

9.1.5.1.1 Thermal-Chemical Characteristics

Beginning with the thermo-chemical characteristics, the exact cure kinetics of the resin must be determined. This part of the process requires test samples to be laid-up, cured, and post-cured using the same procedure as the full scale part. This was done in our lab, and a great deal was learned about the chosen resin, temperature ramp rates, etc. Following the development of the cure/post cure profile, the resin was characterized in a DSC (Differential Scanning Calorimeter) to determine the

terms required in the Cure Kinetics Model (chemical cross linking and behaviour-after-vitrification terms).

Heat Capacity was the next term in the model that was determined, although this time it was calculated using published values. It was however, verified experimentally.

Thermal conductivity of the composite is the next characteristic required for modelling PID. This parameter was not measured by Convergent, but instead typical values for epoxy resin and carbon fibre were extracted from literature and used to construct the model.

9.1.5.1.2 Thermal-Mechanical Characterization

DMA testing was performed to characterize the modulus of the epoxy resin used. A model of the resin modulus as a function of temperature and degree of cure was developed.

Resin shrinkage during cure and the CTE (coefficient of thermal expansion) properties had also to be measured.

9.1.5.2 L-Flange Analysis

Once the resin and resin-fibre laminates had been characterized in both thermal-chemical and thermal-mechanical analysis, it is time to fabricate test sampled in order to validate the characterized material properties and to validate the FEA simulation (as well as determine the exact FEA model to use).

The L-Flange parts were made in our lab at DRAO. The L-Flange parts were made using a variety of layups in order to gauge the effect of each of the structural layers. For instance a part was made with just the 4 layers of QISO carbon material. Another was made with the QISO material plus the central ‘core’ carbon layer, and so on up to and including the full layup. The materials used, the layup, and the process for infusion, cure, and post-cure were all as closely similar or identical to the full scale part as was possible.

L-Flange parts were made on high-precision metal tooling. Once the parts were fabricated, the tooling and the parts were shipped to Convergent in Vancouver so that they could measure the full mould and parts surfaces using their CMM (Coordinate Measurement Machine). In this way the ‘spring-in-angle’ could be accurate determined. This spring-in-angle is a characteristic over rotation of an angled part (typically a 90 degree angled part) tends to adopt because of resin shrinkage (usually through thickness shrinkage dominates). The results show that the spring-in angle is not very dependent on the metallic surface layer or veil layers, but is instead dominated by the carbon structural layers. This is good news, because it means that the asymmetric addition of the reflective material stack-up on one side of the composite structure has little effect on the PID.

The L-Flange parts were also used to determine the sensitivity of the model to the mesh. In particular the different layers in the composite structure are best modelled using separate mesh elements.

However, since these layers are so thin (for instance the QISO carbon layer is about 0.7mm thick), and the maximum aspect ratio of an FEA element is about 10:1, this would add up to millions of elements to model the 6m reflector. Both a 'ply-wise' model and a monolithic mesh were run and compared and the difference was found to be slight at least for the L-Flange test articles. Additionally because of the large aspect ratio of the part and the fact that it was cured at room temperature and did not devitrify during postcure (this was carefully checked on the L-Flange parts), the CTE and shear effects are not expected to be significant contributors to the deformations. With the addition of the metallic and veil layers on one side of the laminate the monolithic model did not do quite as well (but Convergent concludes that this different is not significant).

9.1.5.3 Sensitivity Study

A sensitivity study was also carried out to determine the sensitivity of the results to variations in the resin ration and the fibre direction (both parameters expected to have some variability in actual manufacturing conditions).

The conclusions of this study were that fibre angle changes in the expected +- 5 degree range had little effect on the spring-in angle.

Spring-in angle is effected by temperature change away from the cure temperature; but this is expected, the part has a non-zero CTE (although it is low)

Spring-in angle is effected by fibre volume fraction (Vf). Changes in Vf will affect the PID, but the Vf are fairly well controlled using the vacuum infusion process (within one or two percent).

9.1.5.4 Finite Element Model of PID

Once all of the above preparatory work had been completed, then finally the FEA-PID model can be constructed and used to predict the shape change in the part due to resin-cure and resin-shrinkage along with those other interesting effects the occur because of the resin cure-kinetics and other factors.

For this study we also wanted to include the mould. It was thought that the movement of the mould due to CTE effects during the cure cycle would likely influence the part shape. Because of the high accuracy requirement for the ngVLA-6m reflector it was determined that the mould must be made from INVAR or from carbon fibre. Convergent shows in their report that this choice of material, and the room temperature cure cycle chosen for these parts, that the mould's influence on the part shape is negligible.

As mentioned above the FEA model adopted was the monolithic-mesh model. Based on model comparisons done with the L-Flange model comparison, the solutions were deemed similar enough to the ply-wise mesh solution, and the computational requirements are vastly reduced.

An FEA model was then created for the dish surface with it's curved rim, but not including any other structure. This is an accurate representation of the part as it would be during the moulding and curing process; a bare part fully supported by the mould.

9.1.5.4.1 FEA-PID Results

A point cloud of the PID distorted shape was the final product created by Convergent. This cloud can then be compared to the original design surface to see the differences. Figure 9-32 shows this result. The data has been reduced by NRC to show just the residual error. The general characteristic of the PID error is to reduce the radius of curvature of the reflector (reduce focal length). This sort of response, a general 'cupping' of the structure is as expected from prior experience. What is less expected is the '0-90' nature of the error (larger errors in the horizontal and vertical extremes of the reflector in Figure 9-32). The other thing not expected was the predicted magnitude of the error (around 10x that seen in similar reflectors).

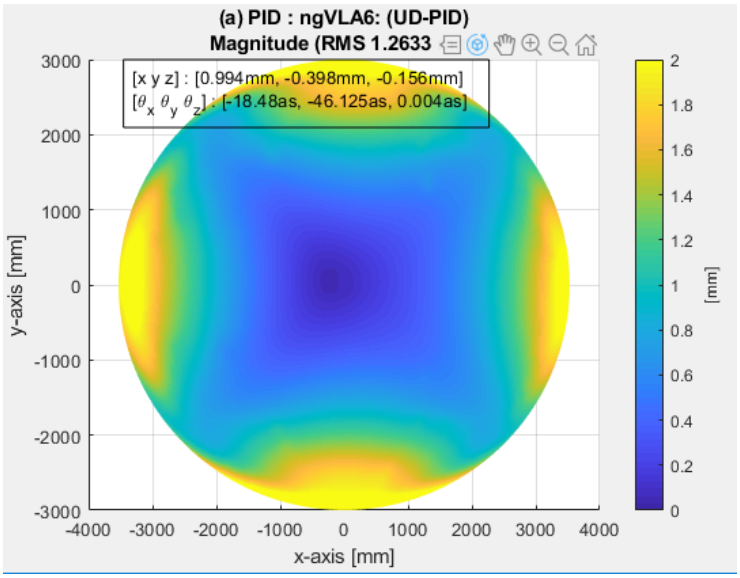

Figure 9-32: Residual plot of calculated PID distortion.

In response to concerns about the nature and magnitude of the predicted errors Convergent has prepared some additional work. Essentially Figure 9-32 shows an ideal case of dish surface errors for a dish suspended perfectly with zero gravity. In order to compare these new theoretical results with past experience Convergence has added gravity and a more realistic support condition. Figure 9-33 shows the same reflector with gravity and with a more realistic (although still idealistic) continuously supported rim. Now we can see can see dish surface distortions that have the same general character as other single piece reflectors built at DRAO such as the DVA1 and DVA2, although the magnitude of these errors is still higher than expected.

It is our opinion that the PID distortion prediction is working in principle, but does still need an intermediate scale test article to further calibrate the model (jumping straight from a 150mm L angle sample to the full 6m scale is too large of a scale increase). Some sort of meso-scale test article such as a more shallowly curved part around 1m in size would be appropriate.

When the PID stresses manifest themselves in a reflector with the rim constrained these stresses cannot warp the dish as in Figure 9-32, but do instead cause low and high spots in the surface as in Figure 9-33. With the mould corrected to compensate for this PID error, these same lows and highs, which normally add to the mould RMS, would then be eliminated (or at least drastically reduced), which is the goal of this work. See RDO5 for further information.

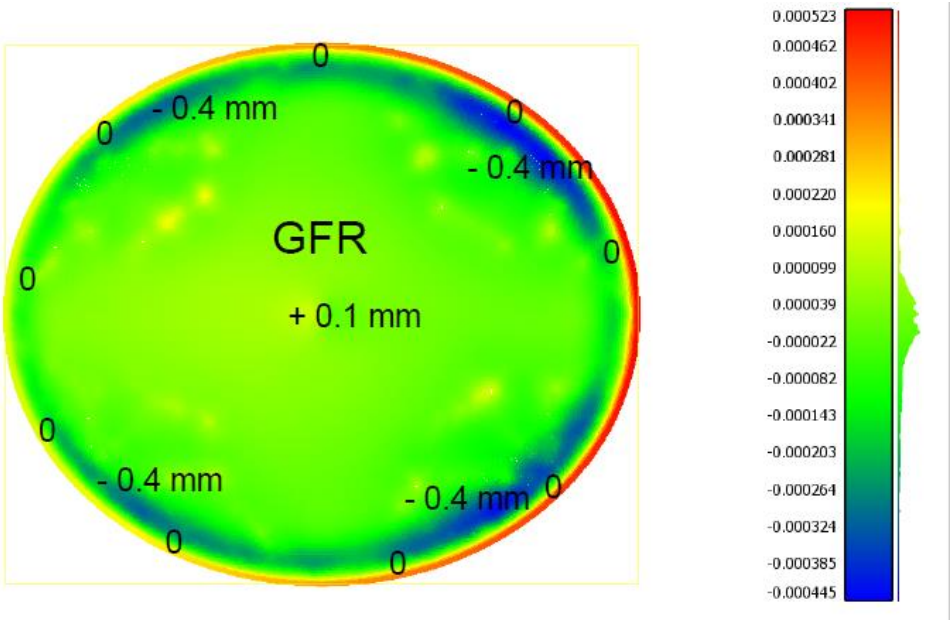

Figure 9-33: The ngVLA 6m reflector showing PID plus gravity with continuous rim support.

9.1.6 Surface Adjustment

Surface adjustment will be achieved by adjusting the bolts at the ends of the OBUS tubes. Since the composite reflector is a large single piece continuous membrane, adjusting the tube-ends near the rim support can attribute to large surface change near the rim. From the FEA results, it is visible that most of the surface distortions are occurring around the rim areas. Previously on the DVA-1/DVA-2 dishes the tube end bolts were adjusted guided by laser tracker measurements in and significant improvement in surface accuracy was achieved. The ngVLA6 design, uses single tubes (means 1 bolt to adjust at a single point of connection) which make the adjustment easier than with the A-frame (two tubes at a single point) support structure in DVA-1/DVA-2.

As an example, in the FE model, two OBUS tubes near the secondary are adjusted, Figure 9-34, using force-displacement DEFORM elements about 0.1 mm at each tube ends. This results in the surface RMS error reduction by 24%. Figure 9-35 presents the results due to adjustment on the discrete dish model.

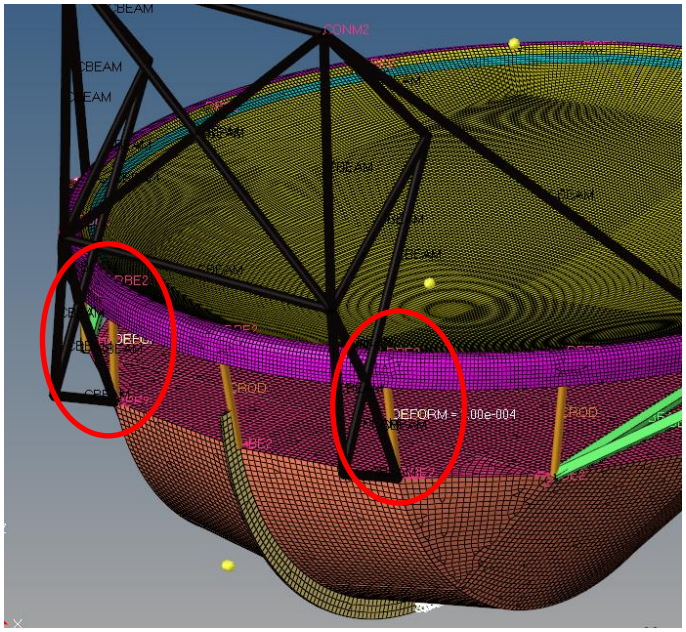

Figure 9-34 DEFORM elements are added to the tubes (in red circle) to show the adjustment performed in the tube end bolts. Current adjustment is set to 0.1 mm.

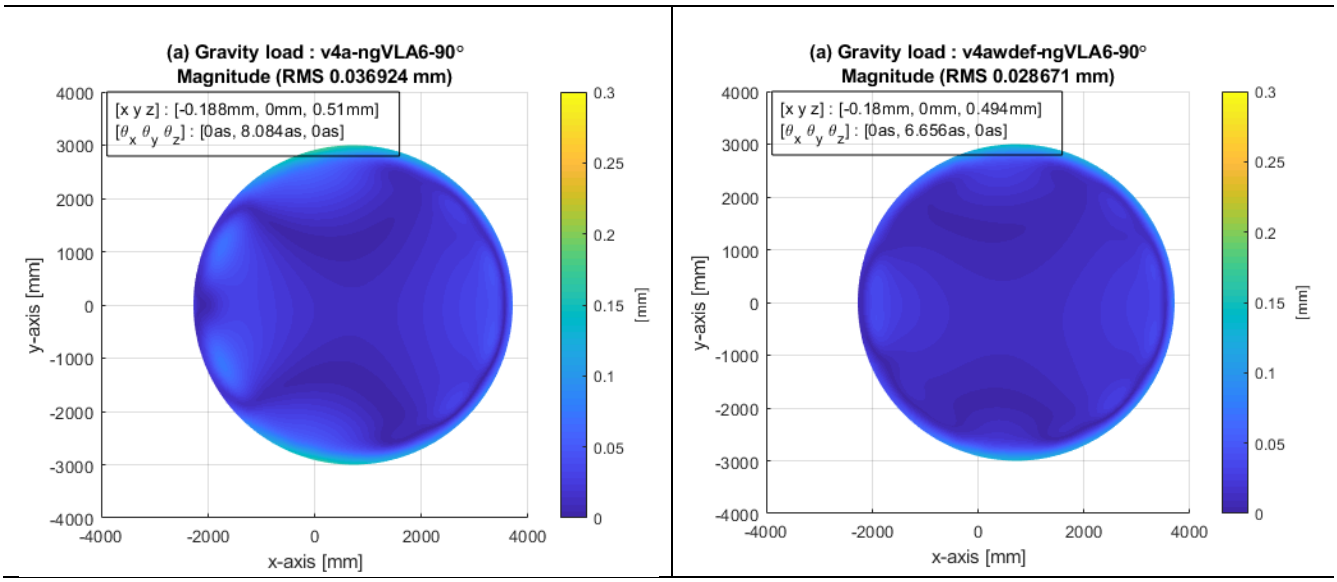

Figure 9-35 (Left) Surface distortion at 90 degrees without adjustment (Right) Surface distortion at 90 degrees after adjustment

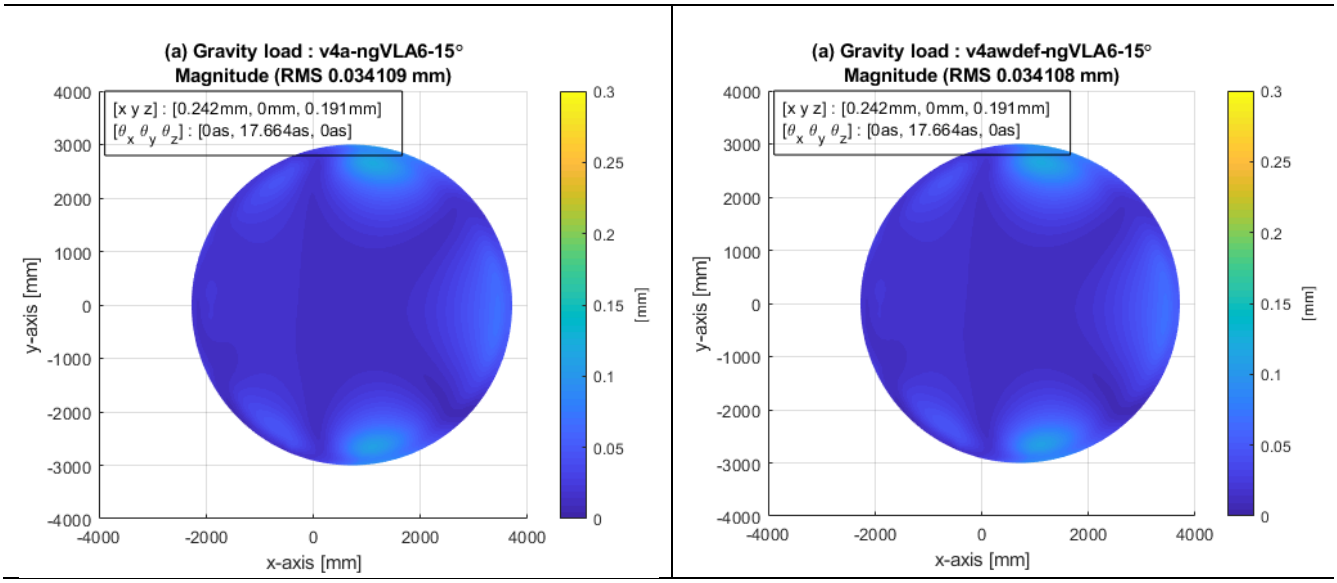

Figure 9-36 (Left) Surface distortion at 15 degrees without adjustment (Right) Surface distortion at 15 degrees after adjustment

Table 9-6 Surface RMS error reduction by adjustment (The adjustment was only performed at 90 degree elevation angle as an example)

Conditions	Errors [μm] at 90°	Errors [μm] at 15°	Notes
No adjustment	36.9	34.1	Figure 9-4, Figure 9-5
With adjustment (100 micron)	28.6	34.1	Figure 9-35

9.2 Pointing

The pointing requirements for the ngVLA 6m antenna are shown in Table 9-7 and Table 9-8.

Table 9-7 Precision Pointing Requirements

Parameter	Req. #	Value	Traceability
Absolute Pointing Error	ANT0611	18 arc sec RMS.	CAL0201
Referenced Pointing Error	ANT0612	3 arc sec RMS, within 3º of the target position and 15 minutes of time.	CAL0201

Table 9-8 Normal Pointing Requirements

Parameter	Req. #	Value	Traceability
Absolute Pointing Error	ANT0621	30 arc sec RMS.	CAL0201
Referenced Pointing Error	ANT0622	5 arc sec RMS, within 3°. Must maintain spec for a minimum of 15 minutes.	CAL0201

At this time a comprehensive pointing analysis has not been performed, this will be a priority in the next phase.

9.3 Survivability

Survivability analysis has not been performed at this time, based on the DVA1/2 experience it is not seen to be a risk but will be analysed in the next phase.

The DVA1/2 design did have a failure mode in survival conditions which was buckling of the surface due to high wind from the back of the reflector. At the end of the reflector opposite the feed and secondary the surface has less shape and therefore less stiffness. With the open BackUp Structure (BUS) of the DVA1/2 the surface is exposed to wind directly from the rear. Plans to mitigate that risk with those designs included adding stiffeners to the back of the surface (not desirable as they might print through under operational loading) or shielding attached to the BUS. With the proposed ngVLA design the back side of the reflector is well shielded by the oBUS and so the back of the surface will not be exposed to direct wind and the buckling failure should not occur. Analysis to confirm this will be performed in the next phase.

10 PRODUCTION LOGISTICS

Production of the proposed design could take place both on and off-site similar to that of the 18m, [RD01] with the primary surface being fabricated on site and all other components fabricated and sub assembled off site and final assembly taking place at the antenna station. The smaller primary reflector size would require much smaller space than the 18m and may be possible to use an existing VLA facility. However the smaller size and quantity may offer the opportunities for other production scenarios such as fabrication the primary and secondary reflector surfaces and assemble the elevation assembly off site and/or final assembly in the existing VLA Antenna Barn and transport full antennas to the nearby stations. A future trade study will examine the options for optimizing the production.